

# **Spectroscopic Electron Density Determination of Plasma Targets for Plasma Wakefield Acceleration**

## **Dissertation**

zur Erlangung des Doktorgrades

an der Fakultät für Mathematik, Informatik und Naturwissenschaften

Fachbereich Physik

der Universität Hamburg

vorgelegt von

*Lars Goldberg*

GUTACHTER DER DISSERTATION:

Prof. Dr. Brian Foster  
Dr. Bernhard Schmidt

ZUSAMMENSETZUNG DER PRÜFUNGSKOMMISSION:

Prof. Dr. Roman Schnabel  
Prof. Dr. Brian Foster  
Dr. Bernhard Schmidt  
Dr. Jens Osterhoff  
Prof. Dr. Gudrid Moortgat-Pick

DATUM DER DISPUTATION:

08.08.2018

VORSITZENDER DER PRÜFUNGSKOMMISSION:

Prof. Dr. Roman Schnabel

VORSITZENDER DES FACH-PROMOTIONS-AUSSCHUSSES PHYSIK:

Prof. Dr. Wolfgang Hansen

LEITER DES FACHBEREICHS PHYSIK:

Prof. Dr. Michael Potthoff

DEKAN DER MIN-FAKULTÄT:

Prof. Dr. Heinrich Graener

# Abstract

---

One of the key issues for the generation of stable and reproducible beams in plasma particle accelerators is control of the initial plasma density distribution. Not only the longitudinal but also the transverse density profile, the species distribution as well as fragmentation and ionization dynamics can have significant impact on the generated beams. In particular at FLASHForward, where the creation of the plasma and the driving of the wakefield are decoupled and which aims to investigate advanced electron injection and beam-transport mechanisms, the precise knowledge of these parameters is vital. Currently established methods, like interferometry or gas density diagnostics using scattering processes, only allow for gas targets operated at densities well above  $10^{17} \text{ cm}^{-3}$  and lack versatility.

This thesis reports on electron density measurements based on the Stark broadening of the spectral lines of hydrogen. The different approaches to convert the linewidth and shift to an electron density have been compared. The electron density of a capillary discharge plasma has been shown to reach its peak value at the beginning of the discharge and decreases over its duration. Furthermore, the spectroscopic measurements allowed for the identification of the capillary's sapphire material as a secondary plasma source besides the hydrogen gas. The successful creation of longitudinal density ramps has also been demonstrated with pure hydrogen gas as well as a mixture of hydrogen and helium. Laser-induced plasmas have been shown to expand during their lifetime of up to  $1 \mu\text{s}$ , with both expansion time and lifetime depending on the backing pressure. Moreover, the transverse density profile changes significantly during the first  $\sim 10 \text{ ns}$ , with the timescale of the change depending on the backing pressure. This rapid change in the density profile in combination with the rapid expansion led to a measured on-axis density below  $10^{17} \text{ cm}^{-3}$ , independent of the backing pressure. It was thereby identified as partially responsible for the unsuccessful attempts to calibrate the spectroscopic density measurements against interferometric density measurements. Furthermore, nonlinear effects induced by the laser pulse when passing through the focusing optics were identified as a second possible reason. These effects led to a change to reflective focusing optics for the plasma creation at FLASHForward.



# Zusammenfassung

---

Einer der Schlüsselaspekte für die Erzeugung von stabilen und reproduzierbaren Elektronenstrahlen in plasmabasierten Teilchenbeschleunigern ist die Kontrolle der anfänglichen Plasmadichteverteilung. Nicht nur das longitudinale, auch das transversale Dichteprofil, die Verteilung der Gasarten sowie Fragmentations- und Ionisationsdynamiken können einen erheblichen Einfluss auf die erzeugten Strahlen haben. Insbesondere bei FLASHForward, wo die Plasmaerzeugung und das Treiben des Wakefields entkoppelt sind und das darauf abzielt fortgeschrittene Elektroneninjektions- und Strahltransportmechanismen zu untersuchen, ist die genaue Kenntnis dieser Parameter entscheidend. Derzeit etablierte Methoden, wie Interferometrie oder Gasdichtediagnostiken basierend auf Streuprozessen, erlauben nur Gaszellen die bei Dichten oberhalb von  $10^{17} \text{ cm}^{-3}$  arbeiten und sind unflexibel.

Diese Arbeit berichtet über Elektronendichtemessungen basierend auf der Starkverbreiterung der Spektrallinien des Wasserstoffs. Die verschiedenen Ansätze die Linienbreite und -verschiebung in eine Elektronendichte umzuwandeln wurden verglichen. Es wurde gezeigt, dass die Elektronendichte eines Kapillarentladungsplasmas ihr Maximum zu Beginn der Entladung erreicht und über die Dauer der Entladung absinkt. Außerdem erlaubten die spektroskopischen Messungen die Identifikation des Saphirs aus dem die Kapillare besteht als sekundäre Plasmaquelle neben dem Wasserstoffgas. Ebenso wurde die erfolgreiche Erzeugung von longitudinalen Dichteramphen mit purem Wasserstoffgas sowie mit Helium-Wasserstoff Gemischen demonstriert. Es wurde gezeigt, dass Laser induzierte Plasmen während ihrer Lebensdauer von bis zu  $1 \mu\text{s}$  expandieren, wobei sowohl die Dauer der Expansion als auch die Lebensdauer vom Gasdruck abhängen. Darüber hinaus verändert sich das transversale Dichteprofil signifikant während der ersten  $\sim 10 \text{ ns}$ , wobei die Zeitskala der Veränderung vom Gasdruck abhängt. Diese schnelle Änderung des Dichteprofils in Kombination mit der schnellen Expansion führte zu einer gemessenen Dichte von unter  $10^{17} \text{ cm}^{-3}$  auf der Laserachse. Dieses Verhalten wurde damit als teilweise verantwortlich für die fehlgeschlagenen Versuche die spektroskopischen Dichtemessungen mit interferometrischen Dichtemessungen zu kalibrieren identifiziert. Außerdem wurden nichtlineare Effekte die beim Durchgang des Laserpulses durch die Fokussieroptiken auftreten als weiterer Grund dafür identifiziert. Diese Effekte führten zu einem Wechsel auf reflektive Fokussieroptiken für die Plasmaerzeugung bei FLASHForward.



# Contents

---

<b>Abstract</b>	<b>iii</b>
<b>Zusammenfassung</b>	<b>v</b>
<b>1. Introduction</b>	<b>1</b>
<b>2. Theoretical Principles</b>	<b>3</b>
2.1. Laser and Optics . . . . .	3
2.1.1. Theory of Light . . . . .	3
2.1.2. Laser Radiation . . . . .	5
2.1.3. Gaussian Beam Optics . . . . .	7
2.1.4. Nonlinear Effects / Optical Kerr Effect . . . . .	8
2.2. Plasmas . . . . .	9
2.2.1. Definition of a Plasma . . . . .	9
2.2.2. Debye Length . . . . .	10
2.2.3. Plasma Frequency . . . . .	11
2.2.4. Wave Guiding in Plasma . . . . .	12
2.3. Plasma Wake-Field Acceleration . . . . .	14
2.4. Ionisation Mechanisms . . . . .	15
2.4.1. Ionization and Dissociation of Molecular Hydrogen . . . . .	17
2.5. Electric Breakdowns and Paschen's Law . . . . .	18
2.5.1. Basic Breakdown Mechanism (Townsend Breakdown) . . . . .	18
2.5.2. Streamer Breakdown Mechanism . . . . .	18
2.5.3. Discharge Regimes . . . . .	19
<b>3. Electron Density Determination by Spectral Line Broadening</b>	<b>21</b>
3.1. Plasma Spectroscopy . . . . .	21
3.2. Spectral-Line Broadening in Plasmas . . . . .	22
3.2.1. The Standard Model of Line Broadening in Plasmas (GKS Model)	23
3.2.2. The GC Model . . . . .	25
3.2.3. The Shift Method . . . . .	27
3.2.4. Conclusion . . . . .	28
<b>4. Experimental Setup</b>	<b>29</b>
4.1. Lab Setup . . . . .	29
4.1.1. The Laser Lab . . . . .	29
4.1.2. The Experimental Lab . . . . .	31
4.2. Plasma Diagnostics and Spectrometer Setup . . . . .	33
4.2.1. Light-Detection Considerations . . . . .	34
4.3. Gas Targets . . . . .	36
4.3.1. Capillaries . . . . .	36
4.3.2. The Gas Cube . . . . .	37

## Contents

---

4.4. Discharge Setup . . . . .	39
4.5. Laser Focusing and Beam Transport . . . . .	40
4.5.1. Focus . . . . .	40
4.5.2. Pointing Stability . . . . .	44
<b>5. Experimental Results</b>	<b>47</b>
5.1. Method of Analysis and Error Considerations . . . . .	47
5.2. Capillary Discharge Plasmas . . . . .	49
5.2.1. Influence of Ablation . . . . .	53
5.2.2. Temporal Plasma Evolution . . . . .	59
5.2.3. Spatial Plasma Distribution and Gas Mixtures . . . . .	61
5.3. Laser-Induced Plasmas . . . . .	64
5.3.1. Possible Length of the Plasma Channel . . . . .	65
5.3.2. Plasma Lifetime and Temporal Evolution . . . . .	65
5.3.3. Spatial Evolution . . . . .	69
5.3.4. Investigating Lower Than Expected Peak On-Axis Densities . . . . .	72
5.3.5. Conclusions . . . . .	77
<b>6. Conclusions and Outlook</b>	<b>79</b>
<b>A. Software</b>	<b>83</b>
A.1. Image Preparation Script . . . . .	83
A.2. Image Analysis Script . . . . .	88
A.3. ToolBox . . . . .	91
<b>Bibliography</b>	<b>100</b>
<b>Acknowledgments</b>	<b>101</b>
<b>Eidesstattliche Versicherung</b>	<b>103</b>

# Introduction

---

Nowadays, a variety of applications in material sciences and life sciences, medicine, and particle physics require highly energetic electron beams. These applications include, but are not limited to, free-electron-lasers (FELs, Kondratenko and Saldin, 1979) and colliders. Most facilities capable of delivering these beams to-date use conventional radio-frequency cavities for acceleration (see e.g. Humphries, 1999). These cavities are limited to acceleration gradients of  $\sim 100$  MV/m by electric or thermal breakdown (Solyak *et al.*, 2009; Wang *et al.*, 2010). Hence, the facilities had to grow in size to fulfill the ever higher energy requirements. A recent example is the European XFEL in Hamburg with its  $\sim 1.6$  km-long acceleration section (Altarelli, 2011; Ebeling, 2017). Advanced accelerator concepts such as laser wake-field accelerators (LWFAs) in plasma, as originally proposed by Tajima and Dawson (1979), and plasma wake-field accelerators in general (Chen *et al.*, 1985; Rosenzweig *et al.*, 1988) can provide acceleration gradients well above 10 GV/m (Gordon *et al.*, 1998). This allows for significantly more compact devices on scales of centimeters.

The FLASHForward facility (Aschikhin *et al.*, 2016) is a plasma wake-field accelerator beamline at the free-electron laser FLASH at the Deutsches Elektronen-Synchrotron DESY in Hamburg, Germany. Its goal is, among others, the plasma-based acceleration of electron beams with energy of order GeV and sufficient quality for use in photon science experiments, in particular for FELs. At FLASHForward, in an approach to decouple the plasma creation from the driving of the wake-field, a multi-TW laser system ionizes a hydrogen gas target while the plasma wave is driven by an electron beam from the FLASH linear accelerator. This separation of ionizing the gas and driving the wake-field allows for improved control over the initial plasma-density distribution which is one of the keys for the generation of stable and reproducible beams. Not only the longitudinal but also the transverse density profile, the species distribution as well as fragmentation and ionization dynamics can have significant impact on the generated beams with respect to their shot-to-shot reproducibility, energy, energy spread, charge, and divergence (e.g. Mangles *et al.*, 2007; Nakamura *et al.*, 2007; Hafz *et al.*, 2008). Especially for increasingly complex scenarios, e.g. specific electron injection and laser-beam transport mechanisms, precise knowledge of these parameters is vital (e.g. Pak *et al.*, 2010; Bourgeois, Cowley, and Hooker, 2013; Martinez de la Ossa *et al.*, 2013). Currently established methods, like interferometry (Kaganovich *et al.*, 1999; Spence, Burnett, and Hooker, 1999; Jones *et al.*, 2003; Gonsalves *et al.*, 2007) or gas-density diagnostics using scattering processes (Raman and Krishnan, 1928; Weineisen *et al.*,

2011; Schaper *et al.*, 2014), only allow for gas targets operated at densities well above  $10^{17} \text{ cm}^{-3}$  and lack versatility<sup>1</sup>. In the spectroscopy setup, for example, switching from a longitudinally to a transversely resolved density measurement is simply a matter of rotating the image on the spectrometer, while an interferometry setup would require the probe beam to be directed along another direction of the target. The spectroscopy method uses the intrinsic glow of the plasma, requiring no additional probe beam and theoretically allowing for density measurements in parallel to the acceleration. Furthermore, the use of a spectrometer opens the possibility of measuring the plasma temperature through the spectral-line intensities and identifying different species within the plasma.

This thesis presents electron density measurements based on the Stark broadening of the spectral lines of hydrogen. For a wide parameter range, laser- and discharge-generated plasmas have been investigated with respect to the temporal evolution of longitudinal and transverse electron-density distributions, as well as plasma lifetime. These measurements identified challenges in using this method for the characterization of the laser-based plasma generation planned at FLASHForward and of the current focusing setup that have been further investigated. Additionally, the measured spectra of capillary-discharge plasmas allowed for the identification of secondary plasma sources besides the hydrogen gas.

Chapter 2 gives an overview of the theoretical foundations necessary for the understanding of this thesis. This includes the description of lasers and optics, ionization through light and electrical breakdown, as well as the general properties of plasma and particle acceleration in plasma. Chapter 3 discusses the different approaches to calculate the plasma-electron density from the spectral-line profiles of hydrogen. The experimental setup, including the lab layout, the laser and discharge, as well as the diagnostics setup, is described and characterized in chapter 4. Chapter 5 details the measurement method and compares the available formulas for converting the spectral line properties to an electron density before presenting the measurements performed on capillary-discharge plasmas and laser-induced plasmas. Finally, chapter 6 concludes the thesis by summarizing the results and giving an outlook for future investigations.

---

<sup>1</sup>If the plasma target has a length such that a sufficient phase shift can be accumulated, interferometry can be used at lower densities. However, for typical plasma targets, this means that interferometry can only be used to characterize the transverse density profile (e.g. Lemos *et al.*, 2013).

# Theoretical Principles

---

This chapter will provide the theoretical foundation needed for the general understanding of this thesis. First, the basics of laser light and optics are covered in section 2.1. Then, the properties of plasmas (section 2.2) and plasma wake-field acceleration (section 2.3) are explained. Finally, section 2.4 describes the ionization of matter by laser pulses before section 2.5 details the creation of plasma via electrical breakdown. In parts, the author covered these topics in his earlier work (Goldberg, 2013).

## 2.1. Laser and Optics

This section covers the theoretical principles governing the behavior of light, including the basic theoretical description (section 2.1.1), the properties of laser radiation (section 2.1.2), the propagation of beams (section 2.1.3) and how to determine if non-linear effects play a role (section 2.1.4).

### 2.1.1. Theory of Light

Light can be regarded as both a particle, called a photon, and an electromagnetic wave. It can be fully characterized by the properties of its electric field  $\vec{E}$  and its magnetic field  $\vec{B}$ . These fields are time  $t$  and space  $\vec{r}$  dependent and can be defined by a vector potential  $\vec{A}$  and a scalar potential  $\Phi$  (e.g. Jackson, 1999; Demtröder, 2009):

$$\begin{aligned}\vec{E} &= -\frac{\partial}{\partial t}\vec{A} - \nabla\Phi, \\ \vec{B} &= \nabla \times \vec{A}.\end{aligned}\tag{2.1}$$

From the Maxwell equations

$$\nabla \cdot \vec{E} = \frac{\rho}{\epsilon_0},\tag{2.2}$$

$$\nabla \cdot \vec{B} = 0,\tag{2.3}$$

$$\nabla \times \vec{E} = -\frac{\partial \vec{B}}{\partial t},\tag{2.4}$$

$$\nabla \times \vec{B} = \mu_0 \vec{J} + \frac{\partial \vec{E}}{c^2 \partial t},\tag{2.5}$$

## 2. Theoretical Principles

---

decoupled by using the Lorenz gauge

$$\nabla \cdot \vec{A} + \frac{1}{c^2} \frac{\partial \Phi}{\partial t} = 0, \quad (2.6)$$

the wave equations that these potentials have to fulfill can be derived by calculating  $\nabla \times \nabla \times \vec{E}$ :

$$\begin{aligned} \frac{1}{c^2} \frac{\partial^2 \vec{A}}{\partial t^2} - \nabla^2 \vec{A} &= \mu_0 \vec{J} \\ \frac{1}{c^2} \frac{\partial^2 \Phi}{\partial t^2} - \nabla^2 \Phi &= \frac{\rho}{\epsilon_0}, \end{aligned} \quad (2.7)$$

where  $c$  is the speed of light,  $\epsilon_0$  is the electric permittivity and  $\mu_0$  is the magnetic permeability, all with respect to vacuum. They depend on each other through  $c = (\epsilon_0 \mu_0)^{-\frac{1}{2}}$ . Furthermore,  $\rho$  denotes the charge density and  $\vec{J}$  represents the electric current density. With no charge distribution  $\rho$  or current  $\vec{J}$  present, a solution of (2.7) is a plane wave travelling with velocity  $c$ :

$$\vec{A}(\vec{x}, t) = \vec{A}_0 \cos(\omega t - \vec{k}\vec{x} + \phi). \quad (2.8)$$

The amplitude and polarization of this wave are determined by  $\vec{A}_0$  and  $\vec{k}$ , respectively, where  $\vec{k}$  is the wave vector, which points in the wave's propagation direction. The angular frequency  $\omega = 2\pi c \lambda^{-1}$  is defined by the wavelength  $\lambda$  and  $\phi$  is a phase offset. Substituting the solution for the vector potential (eqn. 2.8) into the wave equation (2.7) yields the vacuum dispersion relation:

$$|\vec{k}|^2 = \frac{\omega^2}{c^2}. \quad (2.9)$$

The vector potential  $\vec{A}(\vec{x}, t)$  (eqn. 2.8) is also a solution to the wave equation of  $\Phi$  (eqn. 2.7) since both parameters are coupled by equation (2.6). Therefore, using (2.1), the electric and magnetic fields can be described by

$$\begin{aligned} \vec{E}(\vec{x}, t) &= \vec{E}_0 \sin(\omega t - \vec{k}\vec{x} + \phi) \\ \vec{B}(\vec{x}, t) &= \vec{B}_0 \sin(\omega t - \vec{k}\vec{x} + \phi). \end{aligned} \quad (2.10)$$

Assuming the plane wave is travelling along the  $z$  direction with  $\partial \vec{E} / \partial x = \partial \vec{E} / \partial y = 0$ , the Maxwell equation in vacuum  $\nabla \cdot \vec{E} = 0$  yields  $\partial E_z / \partial z = 0$ . Therefore, the electric field along the travelling direction is constant and can be set to 0, which means  $\vec{E} \perp \vec{k}$  and thereby also  $\vec{A} \perp \vec{k}$ . The Maxwell equation (2.4) then yields

$$\frac{\partial B_x}{\partial t} = \frac{\partial B_z}{\partial t} = 0, \quad (2.11)$$

and thereby  $B_x(t) = \text{const.}$  and  $B_z(t) = \text{const.}$ . The constant can again be chosen to be 0, which leaves only components of  $\vec{B}$  with  $\vec{B} \perp \vec{E}$  and  $\vec{B} \perp \vec{k}$ . From this follows, using again equation (2.4):

$$-\frac{\partial B_y}{\partial t} = \frac{\partial E_x}{\partial y} = -kE_x. \quad (2.12)$$

The magnetic field can then be obtained by integrating over time:

$$B_y = \frac{k}{\omega} E_0 \sin(\omega t - kz + \phi). \quad (2.13)$$

Using the relation  $\omega/k = c$  and equations (2.1) yields  $|\vec{E}_0| = c|\vec{B}_0| = \omega|\vec{A}_0|$ .

The energy flux density of an electromagnetic wave is described by the Poynting vector (Poynting, 1920):

$$\vec{S} = \epsilon_0 c^2 (\vec{E} \times \vec{B}). \quad (2.14)$$

Its absolute value corresponds to the intensity  $I$ :

$$S = |\vec{S}| = \epsilon_0 c^2 |\vec{E}| \cdot |\vec{B}| = \epsilon_0 c E^2 = I. \quad (2.15)$$

An exchange of energy between electromagnetic waves and their environment is only possible in discrete quantities of (Planck, 1901)

$$E_{ph} = \hbar \omega \quad (2.16)$$

called photons (Einstein, 1905), where  $\hbar$  is the reduced Planck constant. The momentum of a photon is also quantized and given by (Einstein, 1909)

$$\vec{p}_{ph} = \hbar \vec{k}_{ph}, \quad (2.17)$$

which means that it has a relativistic mass  $m_{ph} = \vec{p}_{ph} c^{-1} = E_{ph} c^{-2}$  and therefore is affected by gravity (Einstein, 1905; Einstein, 1907; Einstein, 1911; Einstein, 1915), although it has no rest mass. Photons having a momentum furthermore implies that they can exert a force on objects, the so-called radiation pressure  $P_L = I c^{-1}$ .

### 2.1.2. Laser Radiation

Laser is an acronym for *light amplification by stimulated emission of radiation*. The principle of lasers is fundamentally based on three types of light-matter interaction (cf. figure 2.1) (Svelto, 1998):

## 2. Theoretical Principles

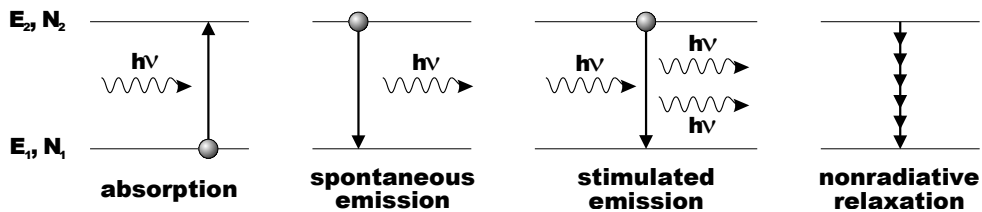


Figure 2.1.: Schematic illustration of the basic interaction of light and matter.

**Spontaneous emission.** Consider an atom with two energy levels  $E_1$  and  $E_2$  with their respective population densities  $N_1$  and  $N_2$ . If the atom is in its excited state  $N_2$ , it will decay into its ground state after the mean lifetime  $\tau_{sp}$  by emitting a photon of energy  $h\nu = E_2 - E_1$ , where  $\nu$  is the frequency and  $h$  the Planck constant.

**Stimulated emission.** This decay can be stimulated by a photon of  $\Delta E = E_2 - E_1$  interacting with the excited atom, which induces the emission of a second photon with identical phase, propagation direction, frequency and polarization.

**Absorption.** If a photon of energy  $\Delta E = E_2 - E_1$  interacts with an atom in its ground state  $N_1$ , it can be absorbed and the atom will enter its excited state  $N_2$ .

Therefore, if light of frequency  $\nu = \Delta E/h$  passes through an active medium with most of its atoms in their excited state  $N_2$  (e.g. through absorption of photons from another light source), it is amplified. A laser oscillator is constructed by placing two mirrors around the active medium, which reflect the light through the medium again and again, thereby further amplifying it with each pass. If one of the mirrors is partially transmissive, a usable light beam is produced. The properties of laser beams are (Svelto, 1998):

**Monochromaticity.** This is due to the fact that only photons of frequency  $\nu = (E_2 - E_1)/h$  are amplified. A resonant cavity is formed by the two mirrors which only allows the oscillation of light at the resonance frequencies of this cavity.

**Coherence,** which can be divided into *spatial* and *temporal* coherence. *Spatial* coherence is given when the phase difference between two points on the wave front of the electromagnetic wave stays constant for all times  $t$ . *Temporal* coherence is given when the phase difference of the fields at times  $t$  and  $t + \tau$  at a given point  $P$  stays constant for all times  $t$ .

**Directionality.** This is due to the fact that it is only possible to sustain a wave within the cavity which is propagating in a direction orthogonal to the surface of the mirrors. Therefore, the beam has a very small divergence.

**High intensity.** Mainly due to the directionality of the emitted light, laser beams have

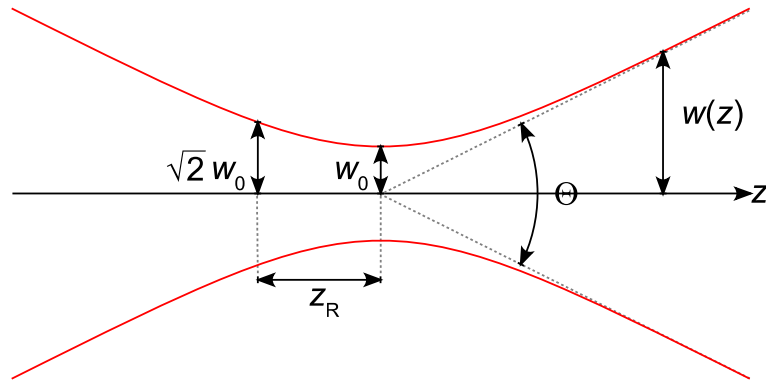


**Figure 2.2.:** Gaussian beam width  $w(z)$  with beam waist  $w_0$ , Rayleigh length  $z_R$  and total angular spread  $\Theta$ .

an intensity<sup>1</sup> several orders of magnitude higher than conventional light sources.

**Short pulse duration.** Lasers can produce light pulses with a duration on the order of the inverse of the linewidth of the laser transition  $N_2 \rightarrow N_1$  (down to  $\sim 10$  fs).

### 2.1.3. Gaussian Beam Optics

Within the scalar approximation, which assumes that electromagnetic fields are uniformly polarized, thereby decoupling the field's phase and amplitude, the electric field of an electromagnetic wave can be described by (Svelto, 1998)

$$E(x,y,z,t) = \tilde{E}(x,y,z) \exp(j\omega t). \quad (2.18)$$

Employing the paraxial wave approximation, where the wave is assumed to be only propagating at a small angle  $\theta$  to the  $z$ -direction, the complex amplitude  $\tilde{E}$  can be written as

$$\tilde{E} = u(x,y,z) \exp[-(jkz)] \quad (2.19)$$

where  $u$  is a slowly varying function compared to the wavelength scale. Within the paraxial wave approximation,  $u$  has to satisfy the paraxial wave equation

$$\nabla_{\perp}^2 u - 2jk \frac{\partial u}{\partial z} = 0 \quad (2.20)$$

with  $\nabla_{\perp}^2 = (\frac{\partial^2}{\partial x^2}) + (\frac{\partial^2}{\partial y^2})$ . Gaussian beams are a class of  $E$ -field solutions to the paraxial wave equation and represent an idealized case of real laser beams, which typically deviate from a purely Gaussian profile.

<sup>1</sup>energy per time and area

## 2. Theoretical Principles

---

Solving the paraxial wave equation (2.20) for a Gaussian beam propagating through free space with the beam waist  $w_0$  at  $z = 0$  (see figure 2.2) yields for the normalized field amplitude (Svelto, 1998)

$$u(x,y,z) = \frac{w_0}{w(z)} \exp \left[ - \left( \frac{x^2 + y^2}{w^2(z)} \right) \right] \exp \left[ -jk \left( \frac{x^2 + y^2}{2R} \right) \right] \exp(j\phi). \quad (2.21)$$

The beam radius at  $z$  is defined as the distance from the beam axis where the intensity is reduced to  $1/e^2$ . It is given by

$$w^2(z) = w_0^2 \left[ 1 + \left( \frac{z}{z_R} \right)^2 \right]. \quad (2.22)$$

The radius of curvature of the propagating wave front of equal phase  $\phi$  at  $z$  is

$$R(z) = 1 + \left( \frac{z_R}{z} \right)^2, \quad (2.23)$$

with  $R(0) = \infty$ . The Rayleigh length  $z_R$  is the distance from the beam waist  $w_0$  at which the beam radius  $w(z)$  has grown by a factor of  $\sqrt{2}$ ,  $w(z_R) = \sqrt{2}w_0$ . For a laser beam of wavelength  $\lambda$ , it is given by

$$z_R = \frac{\pi w_0^2}{\lambda}. \quad (2.24)$$

### 2.1.4. Nonlinear Effects / Optical Kerr Effect

The strong electric field of a high-intensity laser pulse can induce a change in the refractive index  $\eta$  of the medium it is propagating through, which can be written as (Siegman, 1986)

$$\eta = \eta_0 + \eta_2 I, \quad (2.25)$$

where  $\eta_0$  is the linear index of refraction,  $\eta_2$  the nonlinear index of refraction and  $I$  represents the optical intensity. The optical signal itself changing the value of the optical refractive index is commonly referred to as the *optical Kerr effect*.

One effect caused by the optical Kerr effect is *self-focusing*. Suppose a laser pulse with a Gaussian-shaped transverse intensity profile passes through a medium. The center of the pulse will encounter a higher index of refraction compared to the wings, due to the higher intensity in the center, thereby focusing the beam. The focusing increases the intensity in the center which, again, increases the refractive index in the center, leading to an increased focusing effect. This will, theoretically, continue indefinitely. Self-focusing also has an effect on a small scale, since any small amplitude variation in

the transverse beam profile experiences self-focusing and will therefore exponentially grow in amplitude as the laser pulse travels through the medium. This effect can significantly alter the transverse intensity profile.

Furthermore, the optical Kerr effect produces an effect called *self-phase modulation*. The time-dependent intensity  $I(t)$  of laser pulses leads to a time-dependent change of the index of refraction  $\Delta\eta(t) = \eta(t) - \eta_0 = \eta_2 I(t)$ . The resulting change in optical path length leads to a time-varying phase modulation of the pulse. Effectively, the frequency of the pulse during the leading edge will be lowered and the frequency in the trailing edge will be increased, since the light in the high-intensity region between them is delayed.

Since the effects of nonlinear modulation grow exponentially, the so-called *B integral* is defined as a cumulative measure of the nonlinear interaction (Siegman, 1986),

$$B = \frac{2\pi}{\lambda} \int_{z_1}^{z_2} \eta_2 I(z) dz. \quad (2.26)$$

$I(z)$  refers to the transverse peak intensity along the beam axis and  $z$  is the position on the beam axis. A common criterion for high-intensity laser systems is to keep the value of  $B$  below 3 – 4, which corresponds to an accumulated wave-front distortion of approximately  $\lambda/2$  (Mourou and Umstadter, 1992). However, since high on-target intensities are required in short-pulse applications, a more stringent criterion is used here. It states that the peak intensity at focus  $I_p$  is proportional to  $1 - B^2$ . This means that the intensity at focus is decreased by a factor of 2 for  $B = 0.7$  (Mourou and Umstadter, 1992).

## 2.2. Plasmas

This section covers the definition of a plasma as well as its basic properties.

### 2.2.1. Definition of a Plasma

A plasma (Greek, meaning "formed" or "molded") consists of collectively behaving ionized matter. It is often referred to as the fourth state of matter, in addition to the commonly known states solid, liquid, and gas. Strictly, ionized matter has to show the following properties to be considered a plasma (Stix, 1962; Cairns, 1985; Keudell, 2014; Osterhoff, 2009):

**Spatial quasi-neutrality:** The physical dimensions of the plasma volume have to exceed

the Debye screening length  $\lambda_D$  (see section 2.2.2).

**Temporal quasi-neutrality:** The plasma frequency  $\omega_p$  (see section 2.2.3) must be higher than the characteristic frequency describing the processes under investigation, so charges can be shielded rapidly.

**Ideal plasma conditions:** Collective electrostatic interactions have to dominate two-body collisions ( $\Lambda > 1$ , see equation 2.29).

### 2.2.2. Debye Length

The Debye length  $\lambda_D$  defines the length scale above which a plasma appears electrically neutral due to shielding effects between oppositely charged particles. It is defined by (Goldston and Rutherford, 1995)

$$\lambda_D = \sqrt{\frac{\epsilon_0 k_B}{e^2} \left( \frac{n_e}{T_e} + \sum_{\text{ion sorts}} \frac{Z_i n_i}{T_i} \right)^{-1}}, \quad (2.27)$$

where  $k_B$  is Boltzmann's constant and  $n_e$  and  $T_e$  are the electron density and temperature, respectively. Accordingly,  $n_i$  and  $T_i$  correspond to the ion species with charge state  $Z_i$ . Since the mass of the plasma ions is high compared to that of the electrons, their motion can be neglected, especially in plasmas for wakefield acceleration, in which the thermal energy of the electrons significantly exceeds that of the ions  $T_e \gg T_i$ . This allows for the redefinition of the Debye length:

$$\lambda_D = \sqrt{\frac{\epsilon_0 k_B T_e}{e^2 n_e}}. \quad (2.28)$$

Within the range of experimental parameters for plasma acceleration, the Debye length is well below the dimensions of the plasma volume, fulfilling the requirements of spatial quasi-neutrality<sup>2</sup>. The plasma parameter

$$\Lambda = \frac{4\pi}{3} n_x \lambda_D^3 \propto n_x^{-1/2} \quad (2.29)$$

is an important value directly connected to the Debye length. It specifies the number of particles of species  $x$  and of density  $n_x$  inside a sphere of radius  $\lambda_D$  (Fitzpatrick, 2006). In cold and dense systems, electrostatic interaction between the particles is shielded and particle motion is dominated by individual scattering events. Therefore, the Debye sphere only contains a minimum of particles ( $\Lambda < 1$ ) and the plasma is referred to as

<sup>2</sup>E.g. a plasma density of  $n_e = 10^{18} \text{ cm}^{-3}$  and an electron temperature of  $T_e = 5 \cdot 10^4 \text{ K}$  yields a Debye length of  $\lambda_D \simeq 15 \text{ nm}$ .

strongly coupled. This case does not match the strict definition of a plasma due to its lack of collective behavior. Hot and dilute systems, on the other hand, are dominated by collective interactions. The Debye sphere is densely populated ( $\Lambda \gg 1$ ) and the plasma is referred to as weakly coupled. Laser- or discharge-generated plasmas used for particle acceleration are usually weakly coupled, hence the complicated strongly coupled case will henceforth be neglected.

### 2.2.3. Plasma Frequency

Displacing the electrons of a small plasma volume against the ion background by a distance  $\delta x < \lambda_D$  such that no screening effects occur results in an electric field of (Keudell, 2014)

$$E = \frac{en_e}{\epsilon_0} \delta x. \quad (2.30)$$

The corresponding equation of motion for the electrons inside the field is then

$$m_e \frac{d^2}{dt^2} \delta x = -eE, \quad (2.31)$$

which leads to an oscillation equation of the form

$$\frac{d^2}{dt^2} \delta x + \frac{n_e e^2}{\epsilon_0 m_e} \delta x = 0. \quad (2.32)$$

This harmonic oscillation's eigenfrequency is termed the electron-plasma frequency

$$\omega_p = \sqrt{\frac{n_e e^2}{\epsilon_0 m_e}}, \quad (2.33)$$

describing the lowest angular oscillation frequency at which plasma or Langmuir waves (Tonks and Langmuir, 1929) can travel in a plasma of density  $n_e$ . It defines the time scale  $\tau_e$  for collective electron effects to take place in a plasma. Analogously, the time scale  $\tau_i$  of ion dynamics is set by the ion-plasma frequency  $\omega_{p,i} = \sqrt{Z_i^2 e^2 n_i / \epsilon_0 m_i}$ , where  $m_i$  is the ion mass. On typical time scales for plasma acceleration, the ion motion is negligible, since  $m_i \gg m_e$ . Hence the plasma frequency  $\omega_p$  in the following will refer to the *electron*-plasma frequency. On typical time scales for plasma discharges, however, ion motion cannot be neglected. The dispersion relation for the aforementioned plasma waves is given by (Bohm and Gross, 1949)

$$\omega_L^2 = \omega_p^2 + \frac{3k_B T_e}{m_e} k_L^2, \quad (2.34)$$

where  $k_L$  is the Langmuir-wave vector.

#### 2.2.4. Wave Guiding in Plasma

Optical wave guiding in plasmas is based on refractive guiding. If the maximum of the radially symmetric index of refraction  $\eta_r(r)$  is on axis, i.e.  $\partial\eta_r/\partial r < 0$ , the on-axis phase velocity is slower than off axis. The laser beam is then guided by the phase fronts being curved and focused towards the axis. Here, only the qualitative aspects of the guiding mechanisms in plasma will be explained. For an in-depth review of the topic, see e.g. Sprangle *et al.* (1992), Esarey, Sprangle, Krall, and Ting (1997), and Esarey, Schroeder, and Leemans (2009).

An electromagnetic wave with a frequency  $\omega < \omega_p$  cannot propagate within the plasma and is reflected at the plasma surface due to the charges rearranging faster than the light field oscillates. The critical density  $n_{cr}$  above which the wave is reflected is given by  $\omega = \omega_p$  (Dinklage *et al.*, 2005):

$$n_{cr} = \frac{m_e \epsilon_0}{e^2} \left( \frac{2\pi c}{\lambda} \right)^2. \quad (2.35)$$

The plasma is called underdense for  $n_e < n_{cr}$  with  $n_{cr} \simeq 1.7 \cdot 10^{21} \text{ cm}^{-3}$  for an 800 nm laser.

In the 1D limit, a small amplitude electromagnetic wave propagating in a plasma of uniform electron density  $n = n_0$  experiences an index of refraction of  $\eta_r = (1 - \omega_p^2/\omega^2)^{1/2}$ . Large amplitude waves, however, can cause variations in the electron density and mass, due to the electron's relativistic quiver velocity. Therefore,  $m_e \rightarrow \gamma m_e$  and  $\omega_p^2 \rightarrow (\omega_{p0}^2/\gamma)n/n_0$ , where  $\omega_{p0}$  is the unperturbed plasma frequency and  $\gamma$  is the relativistic Lorentz factor. Assuming  $\omega_p^2/\omega^2 \ll 1$ , this yields the general expression for the refractive index for a large-amplitude electromagnetic wave in a plasma (Sprangle *et al.*, 1992):

$$\eta_r(r) \simeq 1 - \frac{\omega_{p0}^2}{2\omega^2} \frac{n(r)}{n_0 \gamma(r)}. \quad (2.36)$$

The radial profile of the index of refraction  $\eta_r(r)$  is influenced by the relativistic factor  $\gamma(r)$  and the radial density profile  $n(r)$ . Since the electron quiver motion orthogonal to the laser's propagation direction  $\vec{p}_\perp = m_e c \vec{a}$  dominates the electron motion in the laser field, the electron motion along the axis can be neglected and  $\gamma \simeq \gamma_\perp = (1 + a^2)^{1/2}$ . The refractive index in the limits  $a^2 \ll 1$ ,  $|\Delta n_p/n_0| \ll 1$ , and  $|\delta n/n_0| \ll 1$  then is

(Esarey, Sprangle, and Krall, 1996)

$$\eta_r \simeq 1 - \frac{\omega_{p0}^2}{2\omega^2} \left( 1 - \frac{a^2}{2} + \frac{\Delta n_p}{n_0} + \frac{\delta n}{n_0} \right), \quad (2.37)$$

where  $n_0 = n(r = 0)$  is the on-axis plasma-electron density,  $\Delta n_p$  is the transverse electron density distribution and  $\delta n$  the density oscillation behind the laser pulse. This expression contains the main contributions to laser guiding in plasmas (Goldberg, 2013):

**The  $a^2/2$  term** accounts for *relativistic self-guiding*. For laser powers above a critical power  $P_c [\text{GW}] = 17(\lambda_p/\lambda)^2$ , the laser-induced relativistic electron quiver motion causes a variation in the electron density and mass. Hence, a laser intensity profile peaked on axis ( $\partial a^2/\partial r < 0$ ) results in a refractive index profile ( $\partial n/\partial r > 0$ ) that enables guiding (Esarey, Sprangle, Krall, and Ting, 1997). However, relativistic self-guiding is ineffective in preventing the diffraction of short ( $L \leq \lambda_p$ ) laser pulses, due to the laser modifying the refractive index on the plasma-frequency timescale rather than the laser-frequency timescale (Sprangle *et al.*, 1992; Esarey, Sprangle, Krall, and Ting, 1997).

**The  $\Delta n_p/n_0$  term** describes *preformed density channel guiding*. For instance, a capillary discharge or an intense laser pulse, through a combination of ponderomotive and thermal effects, can form density channels in plasmas. A radially increasing density profile ( $\partial n/\partial r > 0$ ) corresponds to a radially decreasing refractive index ( $\partial \eta_r/\partial r < 0$ ), which leads to the possibility of guiding. Ideally the plasma channel has a parabolic electron density distribution  $\Delta n_p(r) = n_0 + \Delta n(r/r_0)^2$ , where  $r_0$  is the channel radius. For a capillary-discharge waveguide,  $r_0$  is approximately the capillary radius. A spot size  $w_0 = w_M$  of a Gaussian beam focused at the entrance to the channel that remains constant throughout the propagation through the channel is called the matched spot size. It is given by (Esarey, Sprangle, Krall, and Ting, 1997)

$$w_M = \left( \frac{r_0^2}{\pi r_e \Delta n} \right)^{\frac{1}{4}} \quad (2.38)$$

if no further ionization takes place and ponderomotive and relativistic effects are neglected;  $r_e$  is the classical electron radius. For an unmatched beam with  $w_0 \neq w_M$ , the spot size of the beam oscillates between  $w_0$  and  $w_M^2/w_0$  with a length period of  $\pi^2 w_M^2/\lambda$ .

**The  $\delta n/n_0$  term** describes *self-channeling* and *plasma wave guiding*. The radial ponderomotive force of a long laser pulse ( $L > \lambda_p$ ) travelling in an initially uniform plasma can expel electrons from the axis. The resulting density channel can

enhance the effects of relativistic self-guiding and is called ponderomotive self-channeling (Sprangle *et al.*, 1992). An ultrashort pulse ( $L < \lambda_p$ ) can also be guided by a plasma wave, provided it has the appropriate phase with respect to the wakefield and the wakefield amplitude is sufficiently large (Ting, Esarey, and Sprangle, 1990). Inside a plasma wave of which the density oscillation at a point  $\zeta = z - ct$  behind the laser pulse can be described as  $\delta n = \delta \hat{n}(r) \sin(k_p \zeta)$ , with  $\delta n > 0$  and  $d\delta \hat{n}/dr < 0$ , the regions of the plasma wave in which  $\sin(k_p \zeta) < 0$  enhance focusing, whereas those where  $\sin(k_p \zeta) > 0$  enhance diffraction.

### 2.3. Plasma Wake-Field Acceleration

In plasma wake-field acceleration, two main concepts have to be distinguished, although they share the same basic mechanism. Laser wake-field accelerators (LWFA) use a high-intensity short laser pulse to drive the wake-field while beam-driven plasma wake-field accelerators (PWFA) use a bunched relativistic particle beam as the wake-field driver.

The plasma needed for the acceleration is usually generated by ionizing a gas either via an ionizing laser precursor, a high-voltage discharge or by the wake-field driver itself. Typically used gasses are hydrogen or helium, since they are likely to be fully ionized during plasma generation due to their low atomic number, hence preventing unwanted ionization effects such as ionization defocusing (Auguste *et al.*, 1992). When propagating through the plasma, the wake-field driver expels the plasma electrons in both longitudinal and transverse directions. In the case of a laser driver, this is due to its ponderomotive force, whereas space-charge forces are responsible when using a particle-bunch driver. The ions can be considered to form a static background due to their high mass compared to the electrons. Therefore, the driver leaves behind a region of positive charge which attracts the expelled electrons through the resulting Coulomb force. The electrons then oscillate around their original position, which leads to an electron density modulation with a peak behind the positively charged region following the driver. This plasma wave left by the driver is called the wake-field which, for a flat density profile, has a phase velocity equal to the (group) velocity of the driver.

The electron density spikes and the positively charged regions within the wake-field create a longitudinal Coulomb field that can be used to accelerate particles, with a typically reachable field of (Esarey, Schroeder, and Leemans, 2009)

$$E_0 = cm_e \omega_p / e \quad \text{or} \quad E_0 [V/m] \simeq 96 \sqrt{n_e [\text{cm}^{-3}]}, \quad (2.39)$$

only limited by the electron number density,  $n_e$ . The maximum field of  $E_0 \simeq 96 \text{ GV/m}$

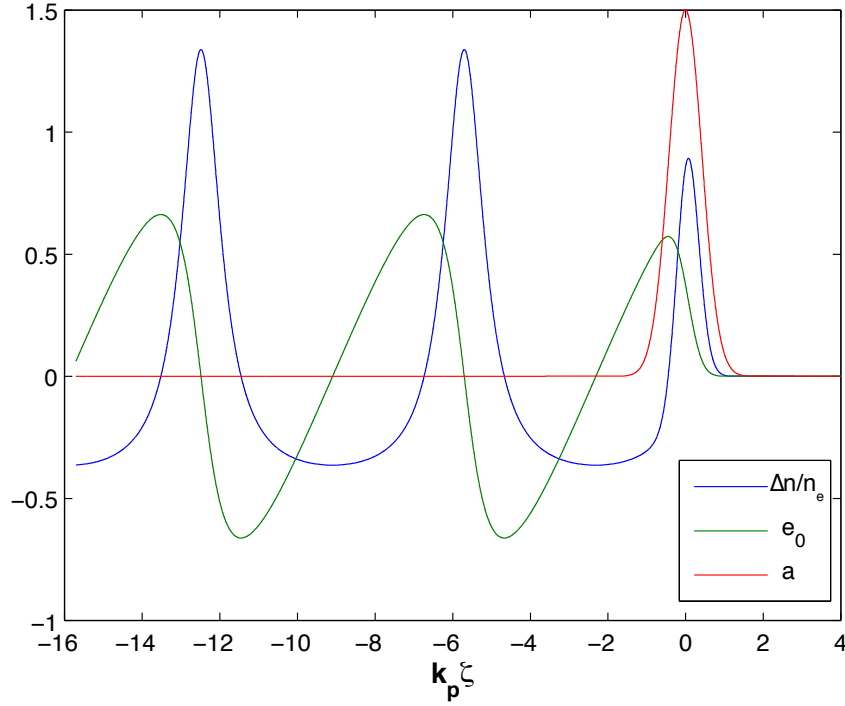


**Figure 2.3.:** Simulated normalized plasma-electron-density modulation  $\Delta n/n_e$  (blue) created by a pulse of  $a = |\vec{a}| = 1.5$  (red). Additionally, the resulting normalized electric field  $e_0 = |\vec{E}_z|/|\vec{E}_0|$  is shown (green).  $k_p \zeta$  is the distance behind the pulse  $\zeta = z - ct$  in units of the wave number  $k_p = \omega_p/c$ . Electrons injected into the buckets between the density peaks can be accelerated. Plot derived from Schwinkendorf (2012).

for a typical plasma density on the order of  $n_e = 10^{18} \text{ cm}^{-3}$  is approximately three orders of magnitude above the current limit for conventional radio-frequency accelerators.

Figure 2.3 shows the normalized plasma electron-density modulation and the resulting normalized electric field. Electrons are accelerated in the propagation direction of the laser by surfing the plasma wave if they are injected into the low-density region behind the laser under the right circumstances (Esarey, Schroeder, and Leemans, 2009). Commonly used methods for injecting electrons into the wake-field are wave-breaking (e.g. Modena, Najmudin, and Dangor, 1995; Bulanov *et al.*, 1998; Malka *et al.*, 2002), density down-ramp injection (Suk *et al.*, 2001) and ionization injection (e.g. Oz *et al.*, 2007; Pak *et al.*, 2010; McGuffey *et al.*, 2010).

## 2.4. Ionisation Mechanisms

The intense light pulses required for the generation of plasmas and electron acceleration therein create extraordinary conditions when interacting with matter. The laser system

## 2. Theoretical Principles

---

designed for the FLASHForward project (see section 4.1.1), for example, carries a peak power of  $P \simeq 25$  TW. In the following, the ionization of matter by such intense laser pulses will be described.

Photoionization of an atom can occur by absorption of a single photon of energy greater than or equal to the ionization energy of the atom (Einstein, 1905). In extension, multi-photon ionization is the simultaneous absorption of  $N$  photons with a cumulative energy sufficient to ionize the atom. The ionization rate of such an  $N$ -photon-process depends on the intensity  $I$  and the generalized  $N$ -photon-ionization cross-section  $\sigma_N$  as  $R_N = \sigma_N I^N$  (Mainfray and Manus, 1991). If the intensity is high enough, a multi-photon process can still be observed for very high values of  $N$  (as long as the electric field can still be treated as a perturbation to the atom's field), even though the cross-section  $\sigma_N$  decreases rapidly with increasing order  $N$ .

The strong electric fields of the laser can also alter the inner-atomic fields. In this case, the bound electrons can tunnel out of the deformed potential well (tunnel ionization, e.g. Ammosov, Delone, and Krainov, 1986; Delone and Krainov, 1998) or escape over the suppressed Coulomb barrier (barrier-suppression ionization, e.g. Augst *et al.*, 1991; Delone and Krainov, 1998). The Keldysh parameter (Keldysh, 1965; Perelomov and Popov, 1967)

$$\gamma_K = \sqrt{\frac{E_i}{2U_p}} \quad (2.40)$$

determines whether multi-photon mechanisms ( $\gamma_K > 1$ ) or strong-field effects ( $\gamma_K \ll 1$ ) dominate the ionization process. It is the ratio of the ionization energy  $E_i$  to the ponderomotive potential of the electromagnetic field  $U_p$ . The latter is defined as the cycle-averaged kinetic energy  $U_p = \langle E_q \rangle = \frac{1}{2} m_e \langle |\vec{v}|^2 \rangle$  due to the quiver motion of a free electron of charge  $e$  and mass  $m_e$  in an oscillating light field with magnetic field  $\vec{B}$  and electric field  $\vec{E}$ . Considering the Lorentz force (Maxwell, 1861), the electron quiver velocity  $\vec{v}$  is given by the electron's equation of motion:

$$m_e \frac{d}{dt}(\gamma \vec{v}) = -e(\vec{E} + \vec{v} \times \vec{B}). \quad (2.41)$$

In the non-relativistic case ( $\vec{v} \ll c$ ), the relativistic factor  $\gamma = (1 - |\vec{v}|^2/c^2)^{-1/2}$  is unity and the  $\vec{v} \times \vec{B}$  term is negligible since  $|\vec{B}| = |\vec{E}|/c$ , thereby reducing equation (2.41) to

$$m_e \frac{d\vec{v}}{dt} = -e\vec{E}. \quad (2.42)$$

Integrating (2.42) over time yields the electron-quiver velocity. Considering linear polarization and a slowly varying electric-field amplitude compared to one oscillation,

the ponderomotive potential then is

$$U_p = \frac{e^2}{4m_e\omega^2} |\vec{E}_0|^2 \quad (2.43)$$

for an electron initially at rest ( $\vec{v}_0 = 0$ ). Above the critical laser-field strength (Tong and Lin, 2005)

$$E_b = \frac{\kappa^4}{16Z_c}, \quad (2.44)$$

barrier-suppression ionization dominates over the competing processes. Here,  $Z_c$  is the charge seen by the electron and

$$\kappa = \sqrt{2E_i}. \quad (2.45)$$

When  $E_b$  reaches unity, the potential barrier is suppressed completely by the laser field and the electron can leave the atom without tunneling. Due to the temporal intensity profile of a high-intensity laser pulse, it is possible that the lower intensity in the leading edge of the pulse already fully ionizes the atom through multi-photon ionization before strong-field effects come into play. In this case, the peak intensity of the laser pulse does not play a role in the ionization of the atom.

The strength of an electromagnetic pulse relative to the electron rest energy is determined by the normalized vector potential (e.g. Gibbon, 2005)

$$\vec{a} = \frac{e\vec{A}}{m_e c^2}. \quad (2.46)$$

If  $a = |\vec{a}|$  reaches unity, the kinetic energy gained by an electron in a half-cycle of a light wave is comparable to its rest energy. Hence, the threshold between the non-relativistic ( $a \ll 1$ ) and the relativistic case ( $a \geq 1$ ) is marked by  $a = 1$ .

### 2.4.1. Ionization and Dissociation of Molecular Hydrogen

An intense laser pulse can ionize and dissociate molecular hydrogen ( $H_2$ ) via three different paths as shown in figure 2.4. In one path, the  $H_2$  molecule can dissociate into two neutral hydrogen atoms which are then independently ionized. In the other path, the molecular hydrogen can initially be ionized to an  $H_2^+$  molecule. Afterwards, it is either further ionized to an  $H_2^{++}$  and then dissociates, or it is split into a neutral H atom and an  $H^+$  ion before full ionization. The path taken depends on the laser pulse duration and peak intensity. Dissociation requires at least 20 fs to 40 fs, due to the finite velocity of the nuclei, while ionization requires higher energies. A more detailed analysis of this topic can be found in the master thesis of Gabriele Tauscher (2016).

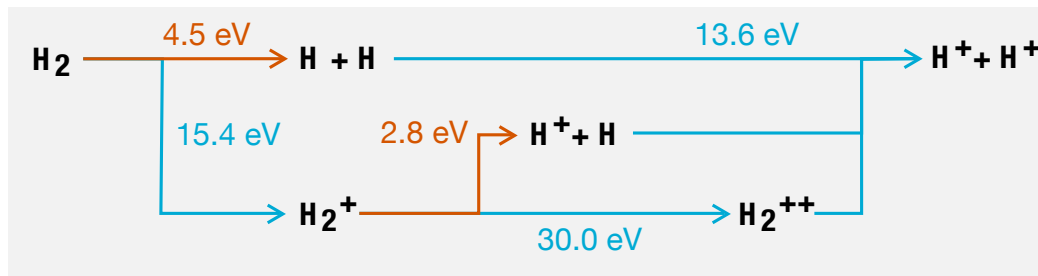


**Figure 2.4.:** Flowchart of the possible ionization (blue) and dissociation (orange) paths of molecular hydrogen and their respective required energies. Plot derived from Gabriele Tauscher (2016).

## 2.5. Electric Breakdowns and Paschen's Law

This section details the basic mechanisms of electrical breakdowns in gases.

### 2.5.1. Basic Breakdown Mechanism (Townsend Breakdown)

If a high voltage (HV) is applied between two electrodes forming a discharge gap inside a gas-filled volume, an electrical breakdown can be initiated through the generation of a free electron inside the gap. The electric field between the electrodes accelerates the electron towards the anode. Through ionization of the gas caused by the accelerated electron, more electrons are generated which, in turn, are accelerated in the electric field and ionize the gas. This causes an exponential growth of charged particles between the electrodes, with additional electrons being produced by positive ions colliding with the cathode (secondary electron emission). Once a critical current density is reached, a breakdown occurs (see e.g. Dinklage *et al.*, 2005).

The minimum voltage  $U_B$  at which a breakdown can be initiated depends on the product of the discharge-gap spacing  $d$  and the gas pressure  $p$ ,  $U_B \propto p \cdot d$  (Paschen, 1889). This dependence is also known as **Paschen's law**. Figure 2.5 shows Paschen curves for air and hydrogen as originally measured by Paschen (1889).

### 2.5.2. Streamer Breakdown Mechanism

The Townsend breakdown mechanism described above only applies below a certain voltage limit. At higher voltages, the transition to the streamer breakdown mechanism, based on the growth of thin ionized channels between the electrodes, is made. Analogous to the Townsend mechanism, a free electron initiates the breakdown by generating a local plasma due to the high electric field. Highly energetic photons emit-

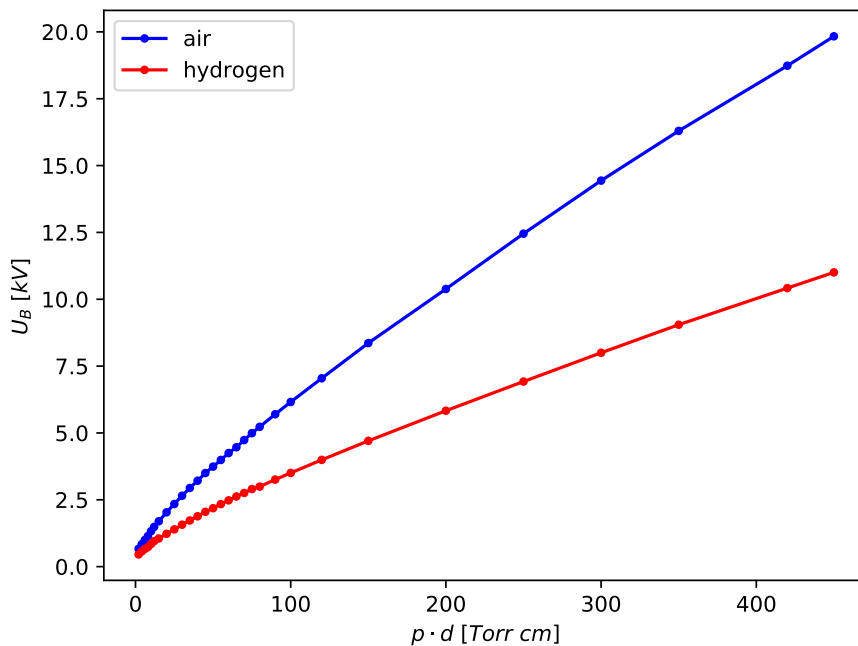


**Figure 2.5.:** Paschen curves for air and hydrogen as measured by Paschen (1889).

ted by the plasma produce new electrons via photoionization. They form a growing ionized channel called a streamer. This ultimately leads to a breakdown followed by an arc discharge, limited by the power source. However, the streamer mechanism is a complex topic beyond the scope of this thesis. For further information, see Morrow and Lowke (1997) and Dinklage *et al.* (2005).

### 2.5.3. Discharge Regimes

An overview of the different discharge regimes and their respective current-voltage behavior is given in figure 2.6. Characteristic of the stationary dark discharge or Townsend discharge regime is a very low discharge current, with the electric field being approximately uniform. With increasing discharge current, the electric field increases at the cathode and decreases at the anode. The transition to the glow discharge is made when the field at the anode is almost zero. Typically a glow discharge is sustained at voltages on the order of 1 kV with low current. At high discharge currents, thermal electron emission at the cathode replaces the secondary electron emission by impact ionization and becomes a major contributor to the discharge besides the field electron emission. Typical parameters for the arc discharge are comparably low voltage ( $\sim 50$  V) and a high current density. This allows for arc discharges to be maintained in vacuum as well as at high pressures (Dinklage *et al.*, 2005).

## 2. Theoretical Principles

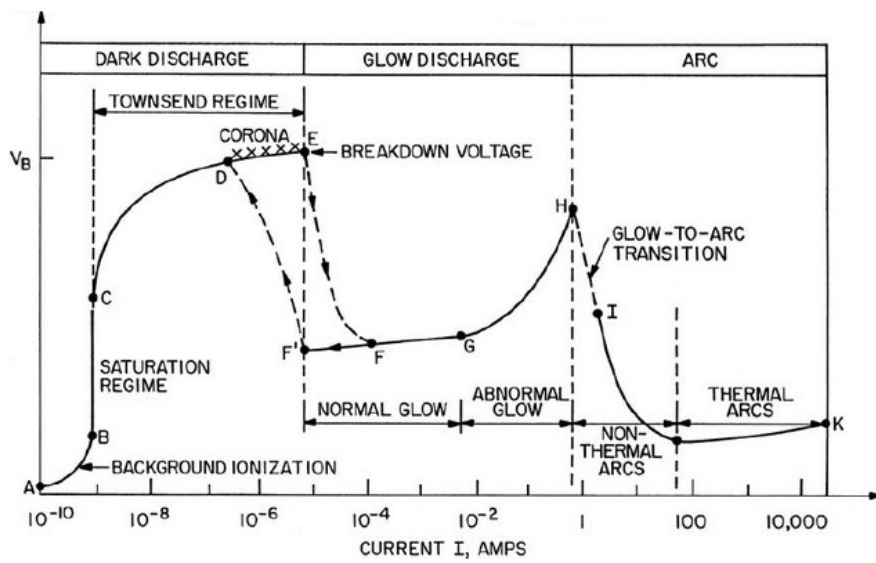


**Figure 2.6.:** Voltage versus current plot of all low-density plasma discharge regimes (dark discharge, glow discharge and arc discharge modes). Plot from Roth (1995).

The parameters of the discharges used within this thesis correspond to the arc-discharge regime. Their measured impedance characteristics indicate that the transition is made via the streamer mechanism.

# Electron Density Determination by Spectral Line Broadening

---

As described in chapter 1, the precise determination of electron densities in a plasma can be quite challenging, especially at low densities which become increasingly important with petawatt laser systems and electron beams driving plasma-wakefield accelerators. An alternative method of measuring the spatially resolved electron density while overcoming the limitations of interferometric or Raman scattering methods will be described in the following. Section 3.1 introduces the term plasma spectroscopy and section 3.2 describes the different approaches on calculating the electron density from the line profiles.

## 3.1. Plasma Spectroscopy

In general, spectroscopy is the study of features in the wavelength or frequency spectrum of electromagnetic radiation emitted from (ionized) matter. While conventional spectroscopy mainly focuses on the atomic structure of an isolated atom, plasma spectroscopy has to also consider the properties of the plasma in the vicinity of the emitting atom. This is due to the fact that ions and electrons are influenced by the electric fields within the plasma as well as collisional processes (Cooper, 1966).

Spectroscopic measurements of plasma emissions can therefore be used to diagnose many plasma parameters. The (electron) density and (electron) temperature are of particular interest, since many plasma properties are described in terms of these parameters. The *density* can be measured by means of (Griem, 1997):

- spectral line widths and profiles,
- shift of spectral lines,
- absolute continuum intensities,
- absolute line intensities, and
- relative line intensities.

Here, 'continuum' refers to the continuous background of the spectrum due to recombination. Analogously, the plasma *temperature* can, for example, be measured through (Griem, 1997):

### 3. Electron Density Determination by Spectral Line Broadening

---

- relative line intensities,
- relative continuum intensities,
- ratios of line and continuum intensities, and
- Doppler profiles.

This work focuses on electron-density measurements through spectral-line widths, which promises to be a simple and accurate method (e.g. Jang, Kim, and Nam, 2012), even for electron densities below  $10^{16} \text{ cm}^{-3}$  (Konjević, Ivković, and Sakan, 2012). Furthermore, the installation of a spectrometer as a diagnostics tool can be extremely valuable due to the wide range of parameters that can possibly be measured with it.

## 3.2. Spectral-Line Broadening in Plasmas

Hydrogen is subject to a large linear Stark effect. Therefore, broadening of hydrogen lines in plasmas is primarily caused by the interaction of the emitting atoms with the local electric fields of the ions and electrons. The electron densities of the plasmas investigated in this work are in the range of  $10^{16} \text{ cm}^{-3}$  to  $10^{18} \text{ cm}^{-3}$ . For plasmas in this density range, the Stark-effect broadening of the Balmer<sup>1</sup>  $H_\alpha$  and  $H_\beta$  lines of 0.5 nm to 30 nm (full width at half maximum, FWHM) usually dominates over other types of spectral-line broadening, such as

**natural line broadening** due to the finite lifetime of the excited states, which is on the order of  $10^{-4} \text{ nm}$  (McIntyre *et al.*, 1989),

**resonance broadening** caused by non-radiative energy transfer through interaction of the emitter with ground-state atoms of the same element, which is on the order of  $2 \cdot 10^{-3} \text{ nm}$  for a ground-state density of  $10^{18} \text{ cm}^{-3}$  (Ali and Griem, 1965; Konjević, 1999),

**Doppler broadening** due to the thermal motion of the emitter, which leads to a broadening of 0.07 nm of the Balmer  $H_\alpha$  and  $H_\beta$  lines for an electron temperature of  $2.3 \cdot 10^4 \text{ K}$  ( $\sim 2 \text{ eV}$ ), which is expected to be the maximum temperature for the plasmas investigated in this thesis (Ashkenazy, Kipper, and Caner, 1991), and

**Van der Waals broadening**, which is caused by the dipole interaction of an excited atom with the induced dipole of a neutral ground-state atom and on the order of  $4 \cdot 10^{-3} \text{ nm}$  for a ground-state density of  $10^{18} \text{ cm}^{-3}$  (Griem, 1997; Konjević, 1999).

---

<sup>1</sup>The Balmer series describes the spectral lines of hydrogen associated with electron transitions from excited states to the principal quantum level  $n = 2$ . The wavelengths of the lines within the visible spectrum are 656.27 nm ( $H_\alpha$ ), 486.13 nm ( $H_\beta$ ), 434.05 nm ( $H_\gamma$ ), and 410.17 nm ( $H_\delta$ ) (Kramida *et al.*, 2017).

These effects can be neglected compared to the Stark-broadening effect, with the exception of Doppler broadening, which can become up to  $\sim 10\%$  of the Stark-broadening width for plasma temperatures of a few  $10^4$  K (a few eV). No indication of Doppler broadening could be found in the line profiles measured for this work, which will be presented in chapter 5. A purely Stark-broadened spectral line has a Lorentz shape, while Doppler-broadened lines have a Gaussian profile (Griem, 1997). If both broadening mechanisms have an influence on the line shape, its profile is a convolution of both functions, called a Voigt function. However, all measured line profiles were best fitted with a pure Lorentz function (see figure 5.1 in chapter 5). The simulations presented in the following do not account for higher-order Stark effects, which become relevant at high plasma densities. At a plasma density of  $\sim 10^{18} \text{ cm}^{-3}$ , the quadratic Stark effect only represents approximately 0.5% of the linear Stark effect (Bethe and Salpeter, 1957). Analogously, fine-structure effects, which become relevant at plasma densities below  $3 \cdot 10^{14} \text{ cm}^{-3}$  have been neglected. Since the densities of the plasmas characterized in this work are between  $10^{16} \text{ cm}^{-3}$  and  $10^{18} \text{ cm}^{-3}$ , these approximations are of no concern.

#### 3.2.1. The Standard Model of Line Broadening in Plasmas (GKS Model)

First considerations for using the broadening of hydrogen lines in plasmas to determine the electron density have been made by Griem, Kolb, and Shen (1959) and were refined in later papers (e.g. Kepple and Griem, 1968; Griem, 1974). They simulated the spectral-line profiles of pure hydrogen plasmas with electron densities of  $10^{15} \text{ cm}^{-3}$  to  $10^{19} \text{ cm}^{-3}$  and temperatures of  $5 \cdot 10^3$  K to  $4 \cdot 10^4$  K in the framework of perturbation theory, considering the influence of the fields of both electrons and ions, as well as the broadening due to collisions of the electrons with the emitting ions and atoms. All calculations by Griem *et al.* were made for plasmas in local thermodynamic equilibrium (LTE). This means that the plasma-electrons and -ions have approximately the same temperature, a Maxwellian velocity distribution and the excited states obey a Boltzmann distribution (Griem, 1997). The laser-induced plasmas characterized in chapter 5.3 do not reach a thermodynamic equilibrium within the femtosecond time frame of the laser interaction with the plasma. This is due to the high mass of the ions compared to the electrons and the fact that the plasma ions are heated via collisions, which takes a long time compared to the observed time frame during which the investigated plasmas can be considered collision-less (see chapter 2.2). Therefore, the laser predominantly heats the electrons. The capillary-discharge plasmas characterized in chapter 5.2 also do not reach equilibrium for the same reasons; the discharge primarily heats the electrons and the ions are heated through collisions. However, they can get closer to LTE due to the longer timescale of the discharge. Griem, Kolb, and Shen (1959) showed that

### 3. Electron Density Determination by Spectral Line Broadening

$T \mid n_e$	$10^{15} \text{ cm}^{-3}$	$10^{16} \text{ cm}^{-3}$	$10^{17} \text{ cm}^{-3}$	$10^{18} \text{ cm}^{-3}$	$10^{19} \text{ cm}^{-3}$
$5 \cdot 10^3 \text{ K}$	0.00969	0.0149	0.0189		
$1 \cdot 10^4 \text{ K}$	0.00777	0.0134	0.0186	0.0215	
$2 \cdot 10^4 \text{ K}$	0.00601	0.0114	0.0175	0.0226	
$3 \cdot 10^4 \text{ K}$	0.00498	0.0100	0.0166	0.0225	0.0258
$4 \cdot 10^4 \text{ K}$	0.00150	0.00922	0.0158	0.0223	0.0270

**Table 3.1.:** Reduced HWHM line width  $\alpha_{1/2}$  [ $\text{\AA}/\text{cgs field strength}$ ] of the  $\text{H}_\alpha$  line for different electron densities  $n_e$  (columns) and temperatures  $T$  (rows) as given by Kepple and Griem (1968).

their simulated spectral-line profiles agreed with experimental measurements to within 10 %.

Kepple and Griem (1968) presented their results for the half width at half maximum (HWHM) of the spectral line  $\Delta\lambda_{1/2}$  in terms of the reduced wavelength

$$\alpha_{1/2} = \frac{\Delta\lambda_{1/2}}{F_0} \propto \frac{\Delta\lambda_{1/2}}{n_e^{2/3}}, \quad (3.1)$$

where  $F_0 = 2.61 e n_e^{2/3}$  (in cgs units) is the Holtsmark field strength (Holtsmark, 1919), which represents the average field of the electrons in the vicinity of the emitter by taking their statistical spatial distribution into account. The electron density and temperature dependent values of  $\alpha_{1/2}$  for the Balmer  $\text{H}_\alpha$  line obtained by Kepple and Griem (1968) are given in table 3.1. Figure 3.1 visualizes the dependency of  $\alpha_{1/2}$  for the  $\text{H}_\alpha$  line on the temperature and electron density. It can be seen that  $\alpha_{1/2}$  is only lightly influenced by the temperature but depends heavily on the electron density. This dependence of  $\alpha_{1/2}$  on the electron density and temperature poses a challenge for the accurate determination of the absolute electron density of a plasma by comparing its measured line width to the simulated values. As long as the temperature of the plasma electrons is unknown, this method can only provide a function  $n_e(T)$  for the measured linewidth. This can be seen in figure 3.1, where multiple combinations of  $n_e$  and  $T$  yield the same value for  $\alpha_{1/2}$  and thereby width of the spectral line. In terms of calculating the electron density from the linewidth, this means that an unknown electron temperature can introduce an uncertainty in excess of a factor of 2. This uncertainty depends on the density range that is under investigation, since the linewidth of low-density plasmas ( $\leq 10^{16} \text{ cm}^{-3}$ ) is more influenced by the temperature than that of high-density plasmas ( $\geq 10^{17} \text{ cm}^{-3}$ ), which can also be seen from the plot in figure 3.1.

Solving equation (3.1) for  $n_e$  and converting from cgs to SI units yields the following equation for converting the full width at half maximum (FWHM) of the spectral lines

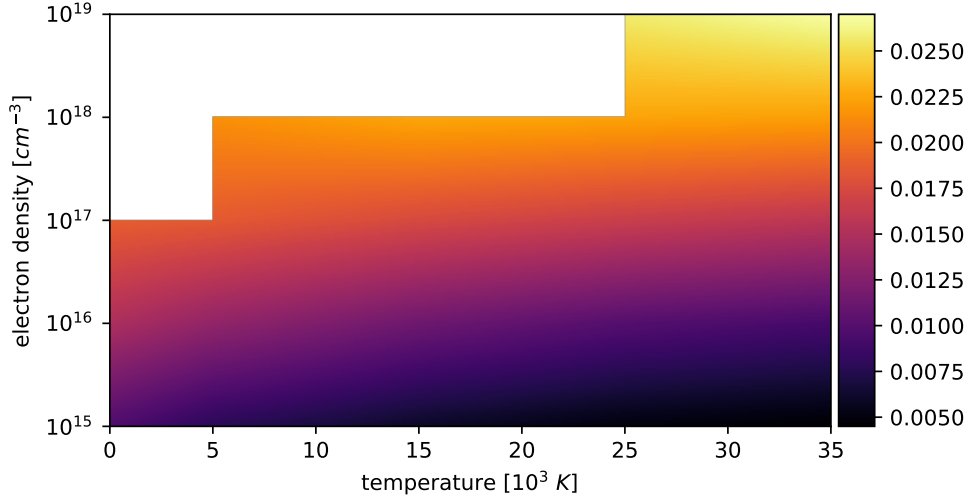


**Figure 3.1.:** Plot of the reduced linewidth  $\alpha_{1/2}$  [Å/ cgs field strength] of the  $H_\alpha$  line against temperature and electron density. The values of  $\alpha_{1/2}$  between those given by Kepple and Griem (1968) (see table 3.1) were linearly interpolated. The white space indicates missing values.

of hydrogen  $\Delta\lambda_{FWHM}$  to an electron density (Ashkenazy, Kipper, and Caner, 1991):

$$n_e [\text{cm}^{-3}] = 8.02 \cdot 10^{12} \left( \frac{\Delta\lambda_{FWHM}}{\alpha_{1/2}(T)} \right)^{3/2}. \quad (3.2)$$

This equation was used by Ashkenazy, Kipper, and Caner (1991) to characterize capillary hydrogen plasmas with densities on the order of  $10^{17} \text{ cm}^{-3}$  for which they estimated the electron temperature to be approximately  $1.2 \cdot 10^4 \text{ K}$  to  $2.3 \cdot 10^4 \text{ K}$ , which is similar to the capillary plasmas characterized in this thesis. Jang *et al.* compared the electron density of a hydrogen-filled capillary plasma obtained by Stark-broadening measurements of the  $H_\alpha$  (Jang, Kim, Nam, *et al.*, 2011) and the  $H_\beta$  (Jang, Kim, and Nam, 2012) line using equation (3.2) to interferometric measurements. For electron densities in the range of  $10^{17} \text{ cm}^{-3}$  to  $10^{19} \text{ cm}^{-3}$ , their results showed an overestimation of the electron density obtained from the  $H_\alpha$ -line width by a factor of  $\sim 2$ , while the electron density obtained from the  $H_\beta$ -line width was in good agreement with the interferometric result. Therefore, this method can at least give an estimate of the absolute electron density and the relative changes in the density can be measured to within a few percent (see chapter 5).

### 3.2.2. The GC Model

A more recent approach to determining plasma electron densities from line profiles has been made by Gigoso and Cardenoso (1996) (see also Gigoso, González, and

### 3. Electron Density Determination by Spectral Line Broadening

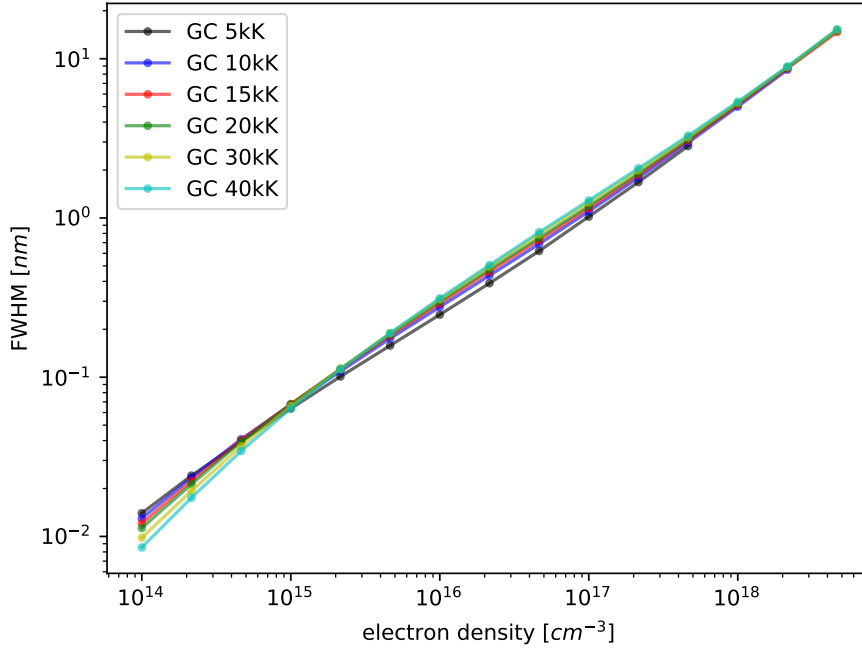


**Figure 3.2.:** Double logarithmic plot of the FWHM line width against the electron density at different temperatures as given by Gigoso and Cardenoso (1996) for  $\mu = 0.5$ . The lines are to guide the eye.

Cardenoso, 2003). Compared to other theoretical studies using perturbation theory, their simulations include ion dynamics and thereby also allow for 'two-temperature' non-equilibrium plasmas, in which the electron kinetic temperature is different from that of the ions. This is achieved by means of the simulation parameter  $\mu$  which defines the ionic mean quadratic velocity relative to the emitter:

$$v_{0i} = \sqrt{\frac{2k_B T_i}{\mu}}. \quad (3.3)$$

In thermodynamic equilibrium, the parameter  $\mu$  equals the reduced mass of the emitter-perturber pair,

$$\mu = \frac{m_{\text{emitter}} \cdot m_{\text{perturber}}}{m_{\text{emitter}} + m_{\text{perturber}}}, \quad (3.4)$$

where  $\mu$  is 0.5 proton masses for a pure hydrogen plasma ( $H - H^+$ ) and 2.0 proton masses for a deuterium plasma surrounded by very heavy ions. Since  $v_{0i} \propto \mu^{-1/2}$ , the ionic velocity decreases for increasing values of  $\mu$ . Therefore, if values of  $\mu$  greater than the equilibrium value are chosen in the simulation ( $\mu > 0.5$  in the case of a pure hydrogen plasma), this corresponds to a plasma with a reduced ionic velocity. Given a fixed mass, a reduced ionic velocity equals a lower ion temperature. Thereby, a

'two-temperature' non-equilibrium plasma is created if the electron temperature remains unchanged. The inclusion of 'two-temperature' non-equilibrium plasmas makes the results of Gigoso and Cardeñoso (1996) theoretically more useful for the plasmas used in plasma acceleration such as those characterized in this thesis, since they only reach a thermodynamic equilibrium after the time frame of interest, as discussed in section 3.2.

Gigoso and Cardeñoso (1996) gave the FWHM of their simulated line profiles for electron densities between  $\sim 10^{14} \text{ cm}^{-3}$  to  $\sim 5 \cdot 10^{18} \text{ cm}^{-3}$  at temperatures of 5000 K to 40 000 K and different values of  $\mu$ . These values are plotted in figure 3.2 for a pure hydrogen plasma ( $\mu = 0.5$ ). Fitting a power law to the results yields the following terms for calculating the electron density from the FWHM line width at the simulated temperatures:

$$5000\text{K} : n_e = 10^{17} \text{ cm}^{-3} \cdot \left( \frac{\Delta\lambda_{FWHM}}{1.03149\text{nm}} \right)^{1.52895}, \quad (3.5)$$

$$10000\text{K} : n_e = 10^{17} \text{ cm}^{-3} \cdot \left( \frac{\Delta\lambda_{FWHM}}{1.06887\text{nm}} \right)^{1.48136}, \quad (3.6)$$

$$15000\text{K} : n_e = 10^{17} \text{ cm}^{-3} \cdot \left( \frac{\Delta\lambda_{FWHM}}{1.08963\text{nm}} \right)^{1.47615}, \quad (3.7)$$

$$20000\text{K} : n_e = 10^{17} \text{ cm}^{-3} \cdot \left( \frac{\Delta\lambda_{FWHM}}{1.10574\text{nm}} \right)^{1.47399}, \quad (3.8)$$

$$30000\text{K} : n_e = 10^{17} \text{ cm}^{-3} \cdot \left( \frac{\Delta\lambda_{FWHM}}{1.14326\text{nm}} \right)^{1.48628}, \quad (3.9)$$

$$40000\text{K} : n_e = 10^{17} \text{ cm}^{-3} \cdot \left( \frac{\Delta\lambda_{FWHM}}{1.17418\text{nm}} \right)^{1.49861}. \quad (3.10)$$

It can be seen that the fit functions at the different temperatures are very similar, suggesting that the temperature dependence is not significant. This behavior is also illustrated in figure 3.2, where the FWHM line width is plotted against the electron density for these temperatures.

### 3.2.3. The Shift Method

Another method to determine the electron density from spectral-line profiles has also been introduced by Griem (1974) in the standard model, with most recent considerations given by Callaway and Unnikrishnan (1991). Besides the broadening of the spectral lines, the shift of the center of the spectral line away from the wavelength in a vacuum towards longer wavelengths due to electron scattering off radiating atoms also depends on the electron density. The expression given for the shift of the line's central wavelength can be used as an alternative method to determine the electron density

### 3. Electron Density Determination by Spectral Line Broadening

---

from the  $H_\alpha$  line profile:

$$d \simeq N_e [\text{cm}^{-3}] d_0(T), \quad (3.11)$$

where  $d$  is the deviation from the unshifted line (in  $\text{\AA}$ ), and  $d_0(T)$  is a factor depending on the electron temperature. Techniques for the calculation of  $d_0$  are described by Callaway and Unnikrishnan (1991). These techniques, however, are computationally expensive and values of  $d_0$  are therefore only given for a small set of plasma parameters. The values of  $d_0$  for conditions of interest in this work are  $0.39 \cdot 10^{-17}$  for  $T = 1.3 \cdot 10^4$  K and  $0.29 \cdot 10^{-17}$  for  $T = 1.9 \cdot 10^4$  K, with an accuracy of  $\sim 10\%$ .

The shifts calculated by Callaway and Unnikrishnan (1991) for plasmas with densities on the order of  $10^{17} \text{ cm}^{-3}$  and with temperatures of  $6 \cdot 10^3$  K to  $4.6 \cdot 10^4$  K were in good agreement ( $\sim 10\%$ ) with experimental values. However, this method is highly dependent on the plasma temperature and the influence of ion dynamics is unknown. Furthermore, this technique is more sensitive to the spectral resolution due to the shift being on the order of  $10^{-2}$  nm for plasmas of  $\sim 10^{17} \text{ cm}^{-3}$ .

#### 3.2.4. Conclusion

Theoretically, all presented methods require knowledge of the plasma temperature in order to accurately determine the electron density. However, if the electron density is determined from the linewidth, the influence of the temperature on the resulting electron density is within the expected uncertainty of the measurements. The standard model and the shift method are strictly only applicable to plasmas in thermodynamic equilibrium, which is not true for most plasmas used in plasma acceleration, due to the short timescales of the processes and the high mass of the ions compared to the mass of the electrons. Furthermore, the shift method requires a spectrometer setup with high spectral resolution and good absolute calibration, since the shift of the spectral lines is on the order of  $10^{-3}$  nm and the result is highly dependent on the measured deviation from the vacuum wavelength. Therefore, the GC model should be the most accurate, since it relies on measurements of the line width and it takes ion-dynamic effects and thereby non-equilibrium plasmas into account.

# Experimental Setup

---

The experiments carried out for this thesis used two different types of plasma generation: a capillary discharge and a multi-TW laser system. This chapter will describe the general lab layout and experimental setup for these experiments. Section 4.1 covers the general structure of the laser lab (4.1.1) and the experimental lab (4.1.2) with the sections thereafter describing parts of the setup in more detail. Section 4.2 describes the spectrometer setup used. The gas targets used in the experiments are detailed in section 4.3 while section 4.4 and section 4.5 cover the discharge unit and the laser beam characteristics, respectively.

## 4.1. Lab Setup

The FLASHForward preparation lab consists of two separate rooms. The laser lab described in section 4.1.1 contains the main laser system along with some smaller lasers and some smaller experiments that do not require the full laser energy. The experimental lab described in section 4.1.2 is the radiation safety area where all experiments requiring full power are conducted.

The general design and setup of the two labs described in the following sections was a joint effort of the group around Jens Osterhoff. The author was partially responsible for cleaning, installing and testing the vacuum components, namely the vacuum compressor, LWFA chamber, ionization test chamber and beamline. Furthermore, the installation and alignment of the optical elements inside the beamline between the vacuum compressor and the two experimental chambers were mainly his responsibility. However, the author's main work was the setup of the ionization test chamber, including the differential pumping section and beam dump, as well as the gas targets and the diagnostics. The exception is the interferometer setup, including the probe beam alignment, which is the work of Gabriele Tauscher.

### 4.1.1. The Laser Lab

The laser lab contains the Amplitude Technologies Pulsar 25 TW Titanium Sapphire laser system shown in figure 4.1. Its main output has a beam diameter of 45 mm with a

#### 4. Experimental Setup

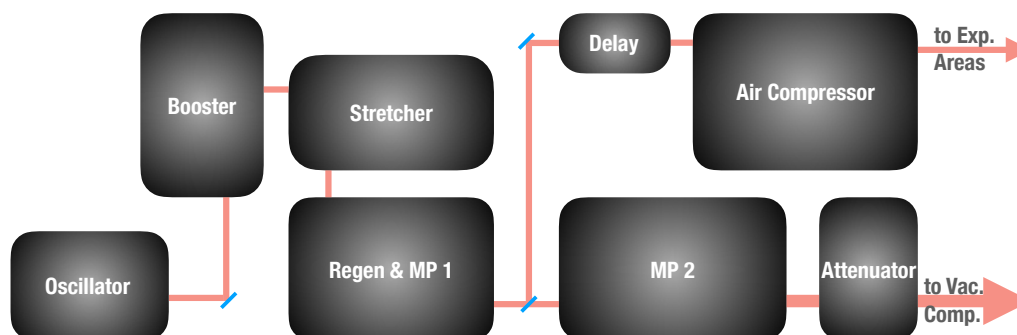


**Figure 4.1.:** Simplified layout of the Amplitude Technologies Pulsar 25 TW titanium-sapphire laser system.

Strehl ratio<sup>1</sup> of 0.85 and a maximum energy of  $\sim 900$  mJ per pulse before compression and  $\sim 600$  mJ on target, which can be lowered by an adjustable attenuator inside the multi-pass amplifier 2 (MP 2). The compressed pulse is usually around 30 fs long with a lower limit of  $< 25$  fs and a temporal contrast of  $> 10^9$ . The pulse length can be varied and optimized by changing its spectral phase, and therefore compression, with an acousto-optic programmable dispersive filter (Dazzler) located between stretcher and regenerative amplifier (Regen). A programmable spectral filter (Mazzler) can alter the Regen gain profile. This is used to flatten and widen the amplified spectrum by reducing the gain in regions where the natural gain of the titanium-sapphire is highest. A second, low-energy output with a beam diameter of 10 mm and a maximum energy of 3.5 mJ is used for experiments that do not require the full energy. Both outputs have a repetition rate of 10 Hz.

The beam path of the laser is as follows: after the seed beam leaves the titanium-sapphire femtosecond oscillator<sup>2</sup>, it enters the booster. It contains a multi-pass amplifier for direct amplification of the oscillator pulses and a saturable absorber<sup>3</sup> to enhance the contrast ratio of the pulses. Furthermore, an electro-optical pulse picker reduces the 108 MHz oscillator pulse train to 10 Hz. Afterwards, the pulses are temporally stretched to reduce the peak intensity in order to prevent self-phase-modulation (e.g. Perry, Ditmire, and Stuart, 1994) and self-focusing effects when the beam is further amplified inside the Regen and multi-pass amplifier 1 (MP 1). Thereafter, the beam is split and takes two paths.

<sup>1</sup>The Strehl ratio is defined as the ratio of the peak diffraction intensities of an aberrated to a perfect wavefront. It indicates the quality of an optical system in the presence of wavefront aberrations, with a value of 1 for a perfect optical system with no aberration. (Sacek, 2006)

<sup>2</sup>VENTEON | Pulse: ONE. Continuous-wave output power:  $\sim 530$  mW, mode-locked output power: 625 mW, repetition rate: 108.3 MHz, pulse length: 7.5 fs, spectral bandwidth:  $> 290$  nm.

<sup>3</sup>The absorption of light in a saturable absorber decreases with increasing light intensity (see e.g. Hofelich-Abate and Hofelich, 1968).

The **main beam** is further amplified in multi-pass amplifier 2 (MP 2) and passes an attenuator, which ensures that the laser can be safely used in a low-power mode for alignment while the experimental lab can still be entered. Afterwards, as shown in figure 4.2, the pulses are temporally re-compressed in the vacuum compressor. Behind the vacuum compressor is a switching chamber where the beam can either be directed into the accelerator tunnel or to the experimental lab. Next in the latter path is the lens chamber which contains a convex followed by a concave lens, each of 1000 mm focal length. Together they produce a focal length of  $\sim 18$  m for ionization experiments inside the ionization test chamber (ITC). Their separation is adjustable in order to fine tune the focal length and they can also be driven in and out of the beam. Afterwards, the beam is directed to the ITC via mirrors inside the corner cubes 1 and 2, and the ITC switch mirror, which can be driven out of the beam path so the beam can reach the LWFA chamber.

The part of the MP 1 output used as the **probe beam** can enter an optional delay section to match its travel time to that of the main beam before re-compression in the air compressor. After compression, the probe beam can directly be used on the table in the laser lab. Alternatively, it can be directed into the experimental lab via its own dedicated path to the ITC or through the main beamline to the LWFA chamber.

#### 4.1.2. The Experimental Lab

The experimental lab contains two main experimental areas. The LWFA Chamber in figure 4.2 is used for laser-driven plasma acceleration experiments. On the far end of the experimental lab is the ionization test chamber (ITC), shown in figure 4.3, which was used for most of the experiments described in this thesis. It has to be 18 m from the lenses in order to simulate the focusing distance that has to be used for the experimental setup at FLASHForward.

The **main beam** enters from the adjacent laser lab through a vacuum pipe in the wall (figure 4.2). A mirror inside the corner cube 2 then reflects it towards the LWFA chamber. By driving the moveable ionization switch mirror into its path, the beam can be deflected to the ITC. Before entering the ITC, the focused beam has to pass three apertures with diameters between 3 mm and 4 mm that limit the gas flow from the chamber into the beamline. The areas in between the apertures as well as the ITC are individually pumped to allow for higher pressure gradients between the ITC and the beamline (differential pumping section<sup>4</sup>). After the interaction, the beam is

---

<sup>4</sup>The space between the first two apertures is pumped by a small turbo pump with 200 L/s (H<sub>2</sub>), the space between the second and third aperture is pumped by a scroll pump with  $\sim 10$  L/s, and the ITC itself is pumped by a turbo pump with 1000 L/s.

#### 4. Experimental Setup

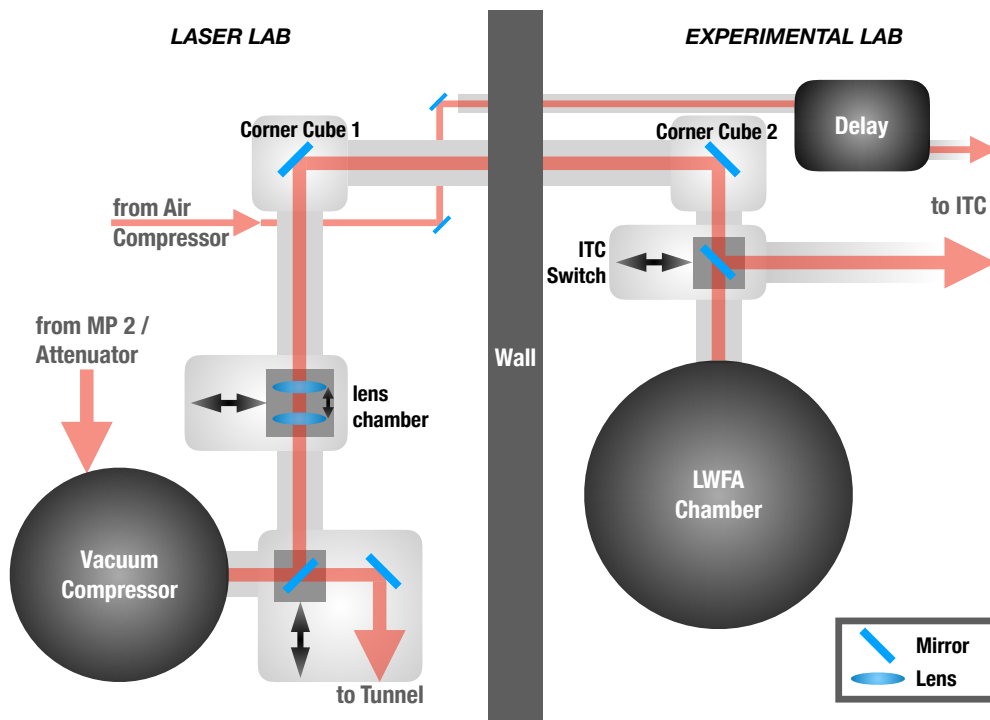


Figure 4.2.: Simplified layout of the beam path from the vacuum compressor into the experimental lab.

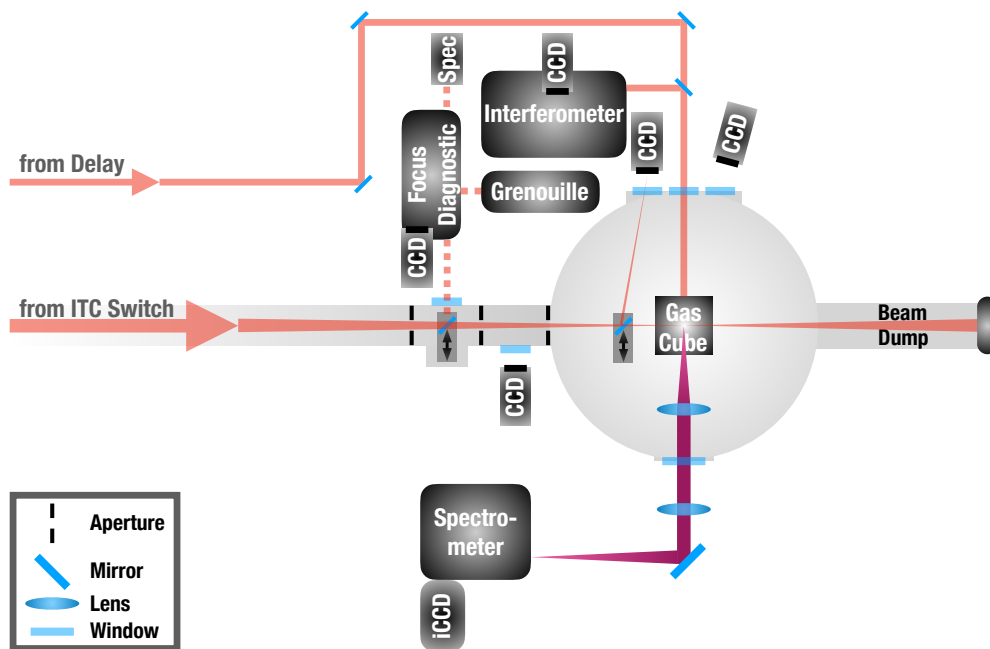


Figure 4.3.: The basic setup of the ionization test chamber. The main ionization laser, as well as the probe beam, enter from the left of the diagram. The plasma is observed by two cameras, one looking in between the second and third aperture and a second looking into the center of the ITC. The spectrometer and an interferometer are used to characterize the plasma.

dumped inside a vacuum pipe that bends downwards behind the chamber. A mirror between the first and second aperture can be driven into the beam path to direct the beam to the focus diagnostic setup, a spectrometer and the Grenouille<sup>5</sup> for pulse length measurements. A second mirror inside the ITC shortly before the gas target can also be driven into the beam path to direct the beam onto a CCD camera to measure the beam position at the gas target.

The low-power **probe beam** from the air compressor enters the experimental lab through a separate pipe next to the main beam pipe. It is first directed to a delay stage to compensate for differences in path length compared to the main beam before it is sent further downstream to the ITC. Here it is used for interferometric and shadowgraphic measurements of the plasma created inside the chamber.

## 4.2. Plasma Diagnostics and Spectrometer Setup

The plasma is observed by two CCD cameras looking at the plasma emission, one between the second and third aperture and a second one looking directly into the center of the chamber. Furthermore, plasma diagnostics are possible via interferometry and spectroscopy.

The spectrometer setup used for the measurements is shown in figure 4.3. Inside the vacuum chamber, a lens<sup>6</sup> captures the light emitted from the plasma and collimates it while a second lens<sup>7</sup> outside the chamber images the plasma onto the spectrometer slit. The light is guided by silver-coated mirrors which allow for proper alignment onto the spectrometer. Two switchable paths enable either transverse or longitudinal imaging<sup>8</sup> of the plasma (only one path is shown in figure 4.3 for simplicity).

The spectrometer in use was a Princeton Instruments SpectraPro 2150i imaging spectrometer with a grating of 1200 lines per millimeter that is blazed at 500 nm. An Andor iStar USB DH334T-18-U-03 with a chip size of 1024x1024 pixels and a pixel size of 13  $\mu\text{m}$  was used for light detection. The slit width providing an optimal ratio of intensity and spectral resolution for this setup was determined to be approximately 100  $\mu\text{m}$ . This resulted in a spectral resolution of 0.05 nm per pixel. The spatial resolution was  $\sim 10 \mu\text{m}$  as measured using a Thorlabs NBS 1963A Resolution Test Target.

---

<sup>5</sup>Grating-eliminated no-nonsense observation of ultrafast incident laser light e-fields, O'Shea *et al.* (2001)

<sup>6</sup>Achromat with 150 mm focal length, 2 inch diameter, design wavelengths: 706.5 nm, 855 nm and 1015 nm.

<sup>7</sup>Achromat with either 50 mm, 100 mm or 750 mm focal length, 2 inch diameter, design wavelengths: 706.5 nm, 855 nm and 1015 nm.

<sup>8</sup>with respect to the laser beam

### 4.2.1. Light-Detection Considerations

The measurement of plasma emissions was done on capillary-discharge plasmas and laser-generated plasmas with diameters between 200  $\mu\text{m}$  and 700  $\mu\text{m}$ . Therefore, to get a basic understanding of the amount of light captured and the depth of field of the imaging system, a simple 2D simulation of the optics based on ray tracing was conducted by propagating the light from the object area (the gas cube in figure 4.3) through the lens setup<sup>9</sup> onto the camera (the spectrometer in figure 4.3). Figure 4.4 shows how much of the light captured by the first lens actually arrives at the camera when the object is at different points around the object plane. Along the optical axis, the transmission only changes by a few percent over the simulated range of 30 mm. Deviation from the optical axis results in a larger decrease in transmission. However, the transmission is still above 80% within a 5 mm radius around the axis. Both types of plasmas under investigation will be smaller than 1 mm. Furthermore, the capillary plasmas are stationary and the laser-induced plasmas should not deviate more than their diameter from their position, according to the pointing measurements in chapter 4.5.2. This means that deviations from the optical axis should be small and all the light from the area of interest would be captured, even if the optics were not perfectly aligned.

However, the limited depth of field of the imaging system results in regions of the plasma that lie outside the imaging plane to be smeared out. This leads to a decrease in the intensity (power per area) in the image while the integrated amount of light that reaches the image remains constant. This decrease in intensity is shown in the black plot in figure 4.5, where the intensity after the lens system of light emitted from a point at different distances from the imaging plane over a solid angle of  $4\pi$  is shown. It can be seen that the intensity already decreases by an order of magnitude  $\sim 20 \mu\text{m}$  from the imaging plane and more than two orders of magnitude  $\sim 100 \mu\text{m}$  from the imaging plane. Furthermore, the lateral smear of the overall image results in an overlap of the imaged regions of the plasma that lie side-by-side within the same plane, which means that the intensities of the overlapping regions add up in the image. Therefore, when imaging the glowing plasma volume, the regions in the line of sight that are farther from the imaging plane are less intense while the increasing overlap of the laterally adjacent regions adds to the intensity. To determine the depth over which the imaged plasma volume contributes to the measurement, the imaging was simulated for a plasma volume spanning the imaging plane with increasing thickness along the optical axis and the line-of-sight integrated intensity was determined. The result is shown in the red plot in figure 4.5. The captured intensity starts to saturate at  $\sim 40 \mu\text{m}$

---

<sup>9</sup>A set of two convex lenses of 2 inch diameter; one was a 150 mm focal length capturing lens and one an imaging lens with 750 mm focal length. The lenses were separated by 400 mm.

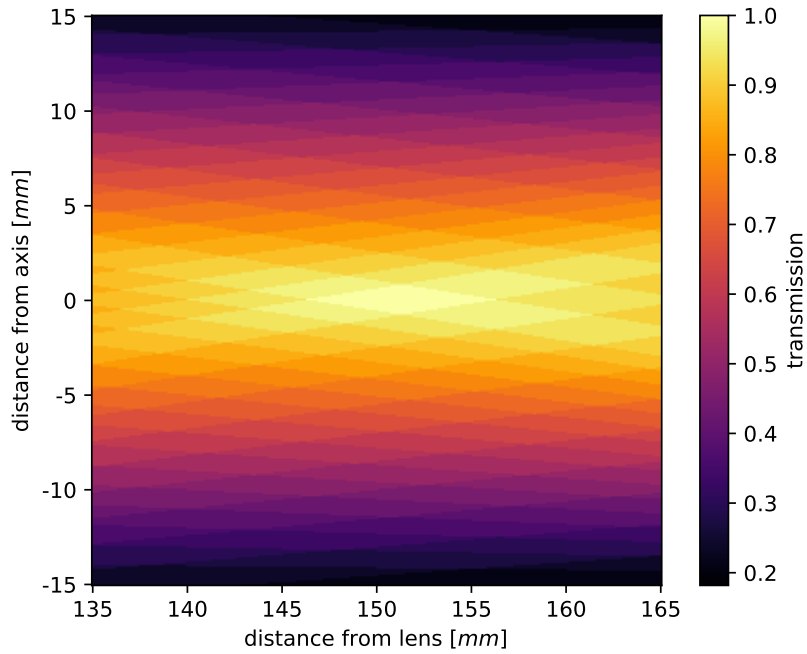


**Figure 4.4.:** Map of the transmitted light through the lens setup for on- and off-axis deviations from the optimal imaging point at 150 mm from the first lens.

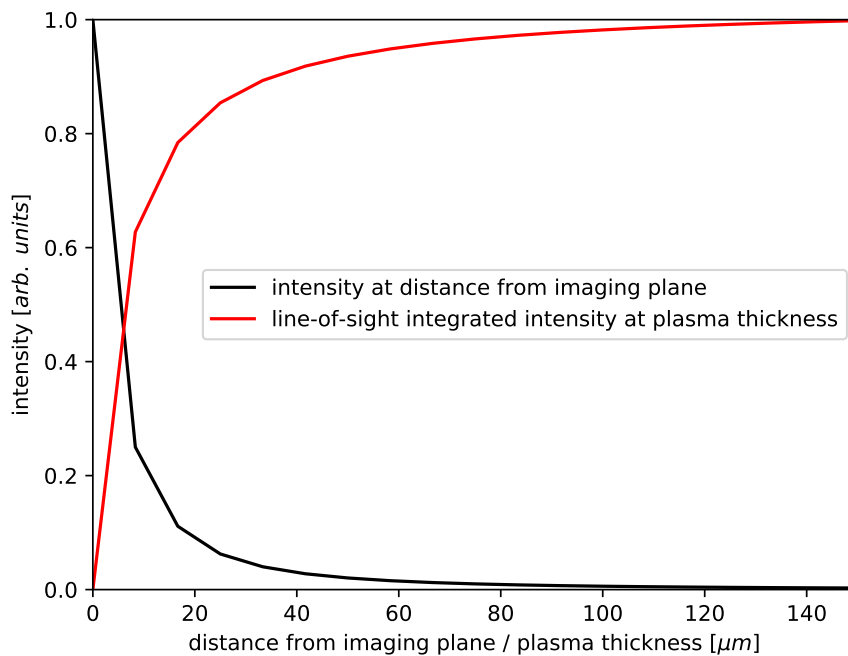


**Figure 4.5.:** Intensity after the lens system of light emitted from a point at different distances from the imaging plane over a solid angle of  $4\pi$  (black). Line-of-sight integrated intensity after the lens system of a plasma volume of different thickness (red).

plasma thickness, where it already reaches 90 % of the overall intensity. At a plasma thickness of  $\sim 75 \mu\text{m}$  it is already at 95 % and at  $\sim 130 \mu\text{m}$  it is at 99 %. Therefore, the depth of field of the imaging system used for the spectroscopic measurements can be assumed to be approximately  $100 \mu\text{m}$ . This is only a fraction of the diameter of the characterized plasmas. Therefore, deviations of the plasma from the optical imaging plane will influence which part of the plasma is measured. This is of particular concern for laser-generated plasmas due to the pointing fluctuations of the laser beam. All measurements were averaged over several tens of shots, which leads to an averaged measurement over the depth of the plasma. In the case of capillary plasmas, only the central region was captured since the capillaries are stationary.

### 4.3. Gas Targets

Commonly used targets for plasma acceleration are gas jets (e.g. Geddes *et al.*, 2004), gas cells (e.g. Osterhoff, 2009; Popp, 2011) and capillary (discharge) waveguides (Dorchies *et al.*, 1999; Spence, Butler, and Hooker, 2001). The latter two types of gas targets were used for the experiments carried out in this work. Sapphire capillaries of various lengths and diameters were utilized as capillary-discharge waveguides, while a custom-made gas cube was the instrument of choice for the measurements with laser-generated plasmas. Both types of targets will be described below.

#### 4.3.1. Capillaries

The sapphire capillaries used in the experiments consist of two sapphire blocks with channels micro-machined into their surfaces by a high-power fs-laser (Schwinkendorf, 2012). The blocks are then pressed together to form the desired capillary.

Figure 4.6a shows a very basic capillary design with a straight horizontal channel of typically  $200 \mu\text{m}$  to  $300 \mu\text{m}$  diameter, extending between the ends of the sapphire block. This channel, which serves as the actual gas target, is filled with gas through two vertical channels of larger diameter (typically  $500 \mu\text{m}$ ) leading from the upper edge of the block to the central channel. The usage of two gas inlets ensures a homogeneous gas density in the section between the inlets as long as an equal pressure is applied to both inlets (see e.g. Schwinkendorf, 2012). If required, it is also possible to create a longitudinally tapered density profile by applying a different pressure to each inlet (see e.g. Messner (2015) or measurements in section 5.2.3). The high voltage (HV) required for generation of a plasma discharge is applied via ring electrodes installed on each end of the capillary main channel. The capillary including the electrodes is mounted

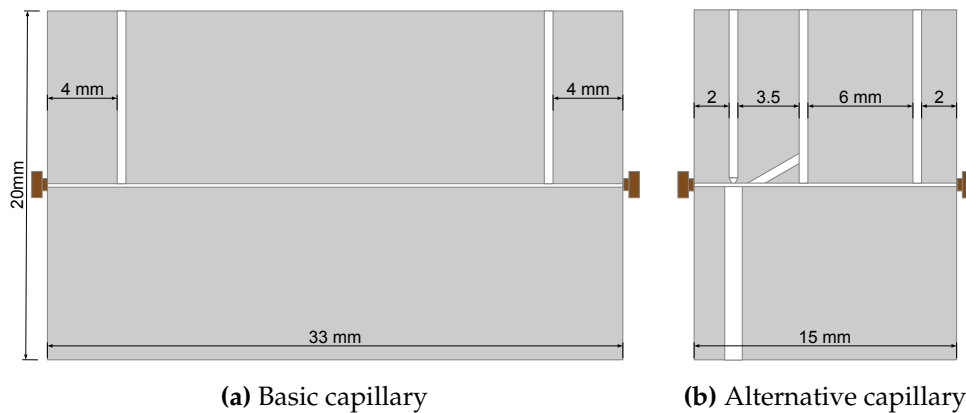


**Figure 4.6.:** (a) Basic capillary with two gas inlets (vertical channels) and electrodes on each side (brown). (b) alternative capillary design with additional gas jet (leftmost inlet) and bypass (diagonal channel). Drawings to scale.

inside the vacuum chamber using a specifically designed Plexiglas holder.

A more sophisticated capillary design is shown in figure 4.6b. Here, an additional gas inlet with a nozzle at the end and an outlet opposite to it are added to create a variable-density gas jet for ionization injection (e.g. Pak *et al.*, 2010; Oz *et al.*, 2007) or density down-ramp injection (e.g. Bulanov *et al.*, 1998; Suk *et al.*, 2001). Furthermore, a bypass is added to the inlet next to the jet to create a smoother density transition.

### 4.3.2. The Gas Cube

The gas cell used for the experiments with a laser-induced plasma is an aluminum cube with 76 mm edges. Figure 4.7 shows it mounted inside the chamber. Four sides are fitted with N-BK 7 windows with a diameter of 2 inches and a thickness of 3 mm. Smaller and much thinner windows (15 mm diameter and 100  $\mu\text{m}$  thickness) are mounted where the laser enters and exits the cube. When fired at high power, the laser machines a hole into each of these thin windows (Pronko *et al.*, 1995), which subsequently allow it to enter and exit the gas cell unobstructed with an aperture that minimizes the gas flow into the vacuum chamber. The cube is filled with gas via a 6 mm tube, which is significantly larger than the entrance and exit holes of the laser<sup>10</sup>, therefore allowing the gas cell to remain pressurized. Figure 4.8 shows a set of windows with the holes produced by the laser after a few thousand shots. The pressure inside the cube is measured by a pressure gauge connected directly to it.

<sup>10</sup>up to 1.5 mm after several thousand shots

#### 4. Experimental Setup

---

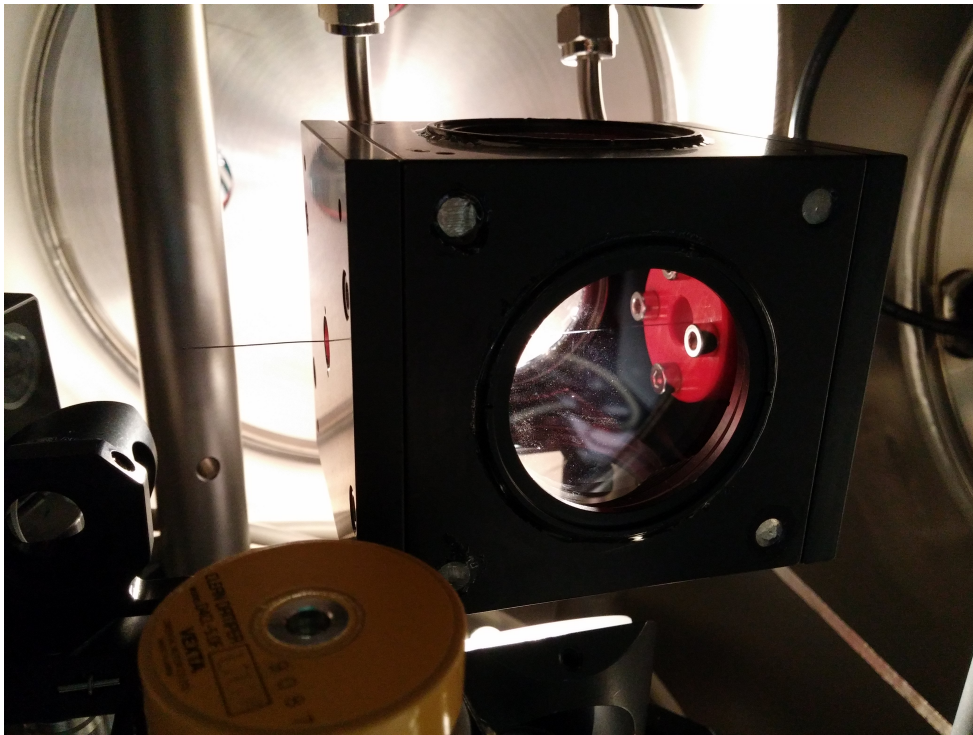


**Figure 4.7.:** The gas cube mounted inside the chamber.

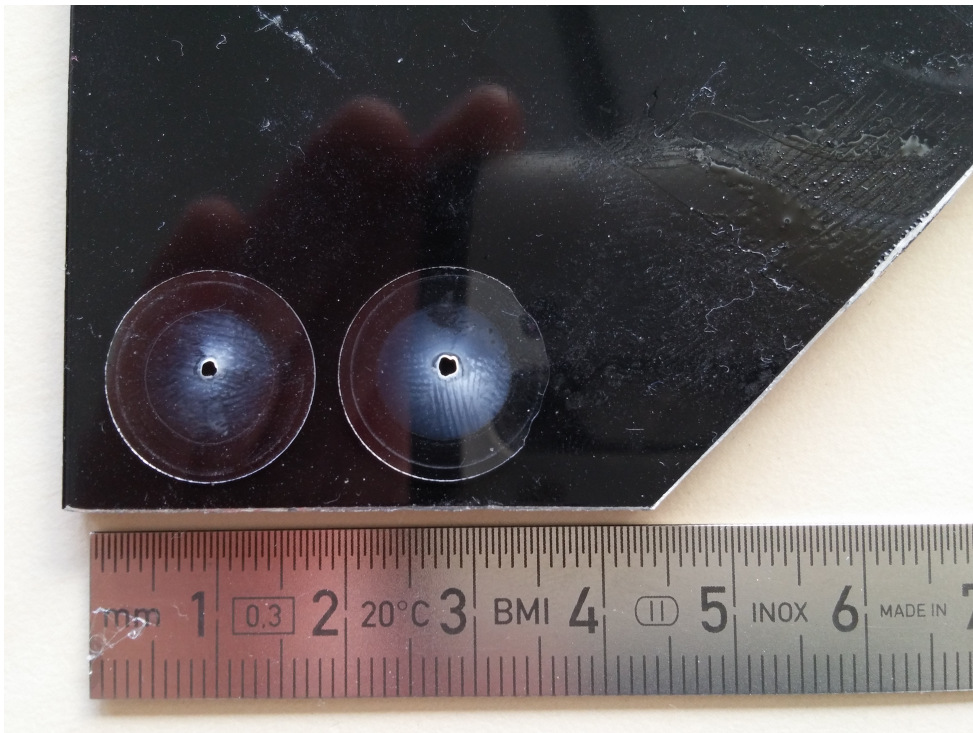


**Figure 4.8.:** The thin entrance and exit windows with the holes produced by the laser after several thousand shots.

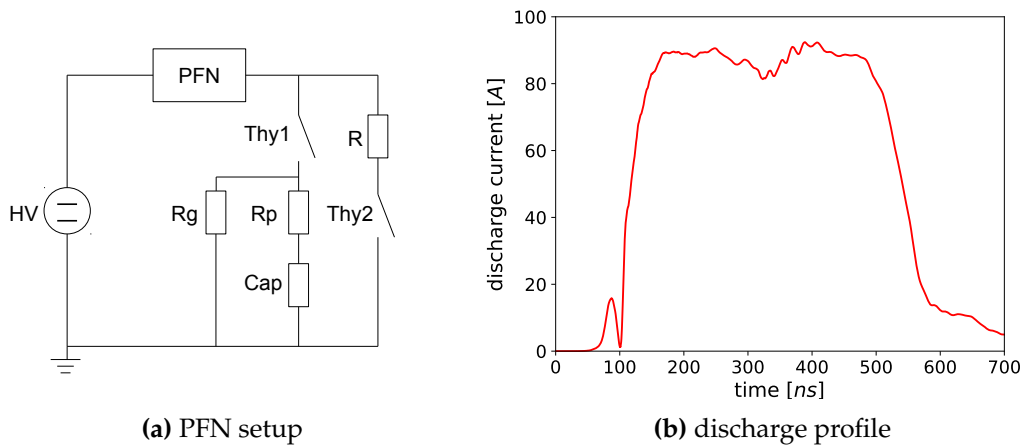


**Figure 4.9.:** (a) Discharge setup with resistances  $R_p=20\ \Omega$ ,  $Cap = \text{varying}\ \Omega$ ,  $R = 2\ \Omega$  and  $R_g = 10\ \text{M}\Omega$ . (b) Example current profile at 75 mbar applied hydrogen pressure.

## 4.4. Discharge Setup

The discharge setup (cf. figure 4.9a) used was the same as described and characterized by the author (Goldberg, 2013).

A pulse-forming network (PFN) consisting of up to 4 cables<sup>11</sup> each of 41 m length is charged at up to 40 kV by an HV generator. With all 4 cables connected, the maximum capacitance of the PFN is 16 nF, which can be lowered to 12 nF, 8 nF, and 4 nF by disconnecting single cables. The energy stored inside the PFN is then applied to the plasma cell by a hydrogen thyatron<sup>12</sup> switch. A pre-resistance  $R_p$  matches the impedance of the capillary to that of the PFN. The maximum duration of the discharge pulse is 400 ns (see figure 4.9b) which can be shortened to approximately 200 ns by a second thyatron that directly grounds the PFN. An induction coil<sup>13</sup> with an output of 0.5 V/A was used as a current monitor.

At a typical charging voltage of 20 kV, the energy stored inside the PFN is 3.2 J at full capacitance and 0.8 J with minimum capacitance. This is more than enough to fully ionize the first level of the typically used gases such as hydrogen, nitrogen or argon at a density of  $10^{18}\ \text{cm}^{-3}$  in a common capillary of 33 mm length and 200  $\mu\text{m}$  diameter, which takes around 10 mJ. It is favorable to keep the energy deposited inside the target to a minimum to prevent damage to the plasma cell. Further considerations on ionization capabilities and damage induction are contained in Goldberg (2013).

<sup>11</sup>Philips HF-Impulskabel 4,9/17,3 FRNC-Mtl.;  $C \sim 101\ \text{pF/m}$ , wave impedance  $50\ \Omega \pm 2\%$

<sup>12</sup>E2V Technologies CX1154

<sup>13</sup>Pearson Current Monitor 6595; max. 1000 A, 2.5 ns rise time

## 4.5. Laser Focusing and Beam Transport

In the ionization experiments, the laser was focused over  $\sim 18$  m to simulate the working conditions at FLASHForward. Such a long focusing distance might significantly influence the position stability on target. The beamline is also connected to and runs near several vacuum pumps and might pick up some vibrations which will be transmitted to the beamline-mounted mirrors and thereby influence the pointing stability. Furthermore, the cost-efficient focusing solution using transmissive optics consisting of two 2-inch lenses for a 45 mm diameter beam raises concern regarding the focus quality. In particular, high output energies might have a negative impact due to non-linear effects in the lenses. Therefore, the focus characteristics on target were examined.

### 4.5.1. Focus

Measurements of the focal spot were taken over a distance of  $\sim 0.5$  m around the beam waist. The minimal beam radius showed a slight asymmetry and was found to be  $\sim 380$   $\mu\text{m}$  horizontally and  $\sim 330$   $\mu\text{m}$  vertically, independent of the pulse energy. However, the scan data shows a small shift in focus position for different energies, as shown in figures 4.11 (horizontal beam radius) and 4.12 (vertical beam radius). It

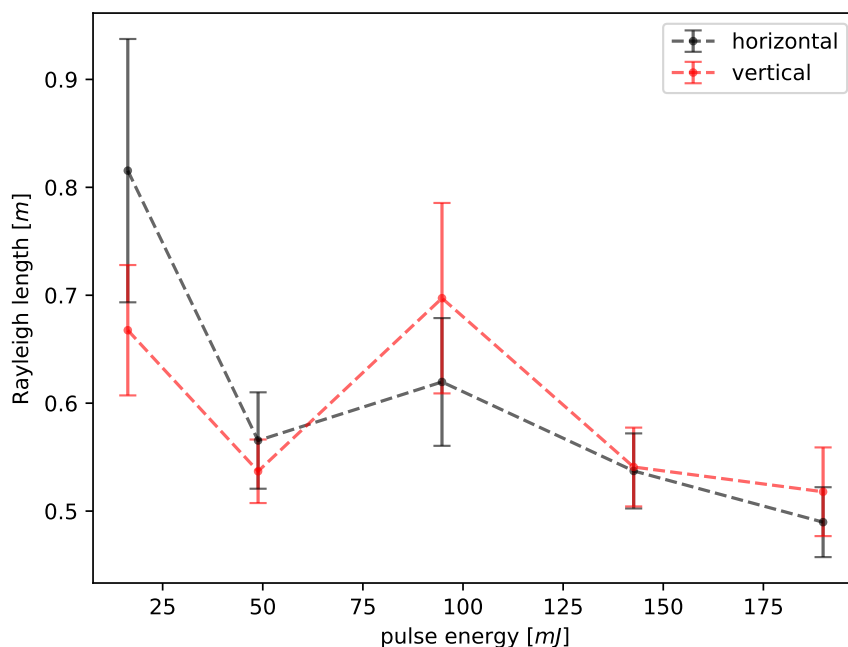


**Figure 4.10.:** Plot of the Rayleigh length against the laser pulse energy. Each measurement was averaged over 20 shots. The error bars represent the RMS from fluctuations.

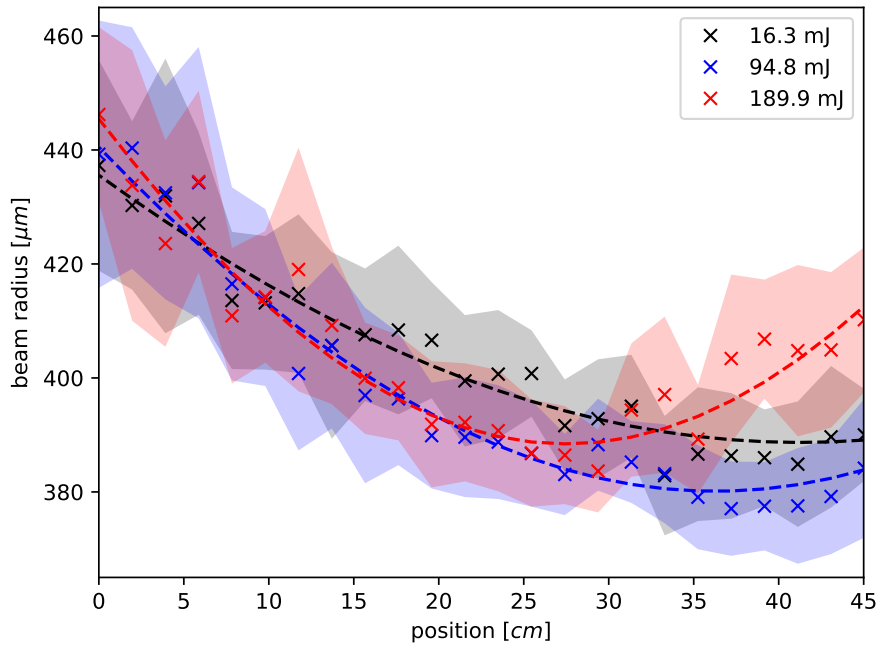


**Figure 4.11.:** Measurement of the horizontal beam size in the vicinity of the waist. Each measurement was averaged over 20 shots. The dashed line indicates the fit. The colored regions show the RMS from fluctuations.

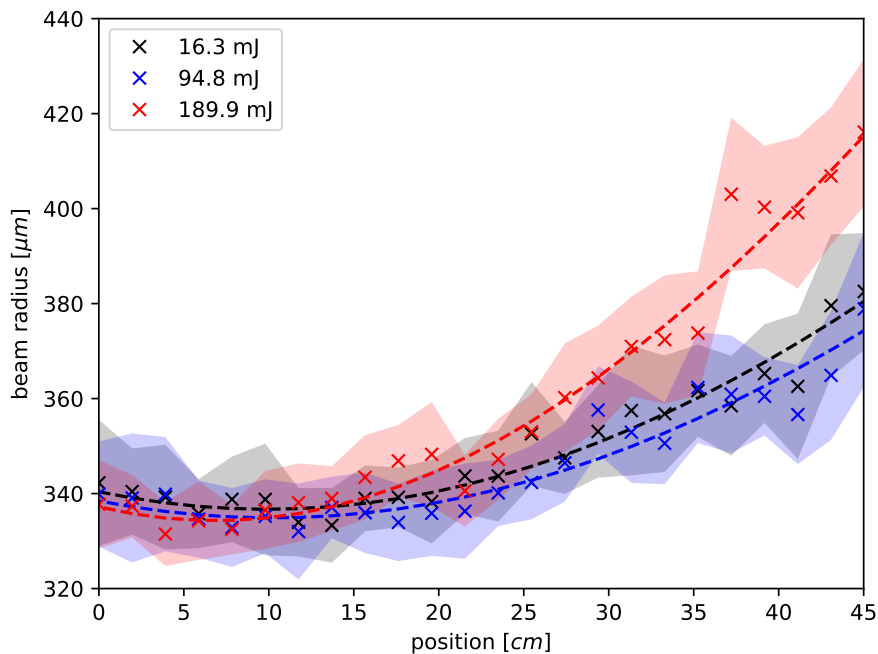


**Figure 4.12.:** Measurement of the vertical beam size in the vicinity of the waist. Each measurement was averaged over 20 shots. The dashed line indicates the fit. The colored regions show the RMS from fluctuations.

#### 4. Experimental Setup

---

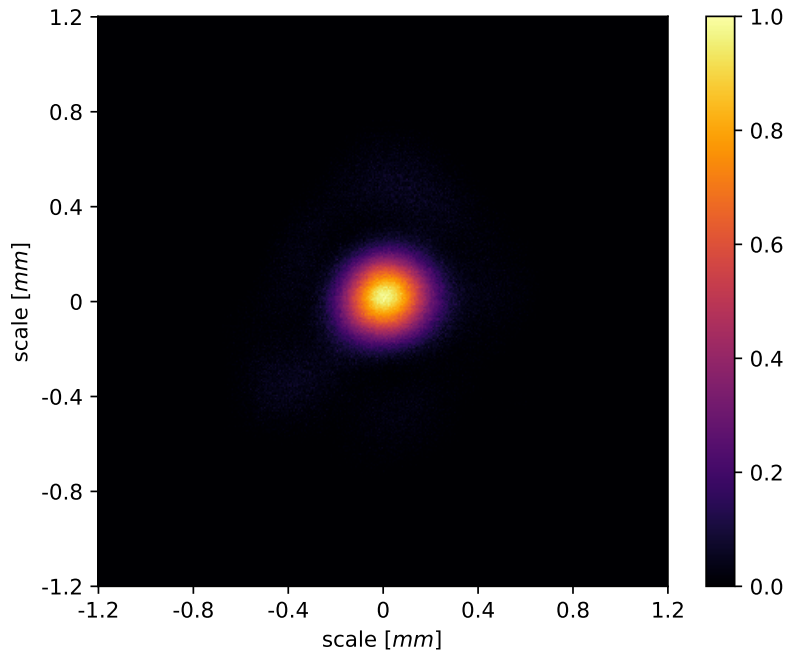


**Figure 4.13.:** Focal spot image at 94.8 mJ pulse energy averaged over 20 shots.

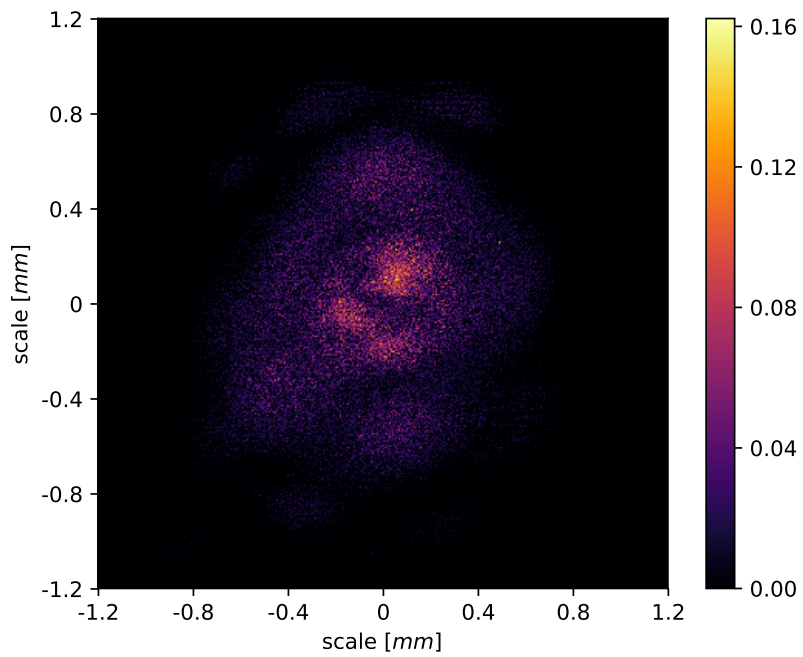


**Figure 4.14.:** Difference image of the normalized focal spots at 189.9 mJ and 16.3 mJ.

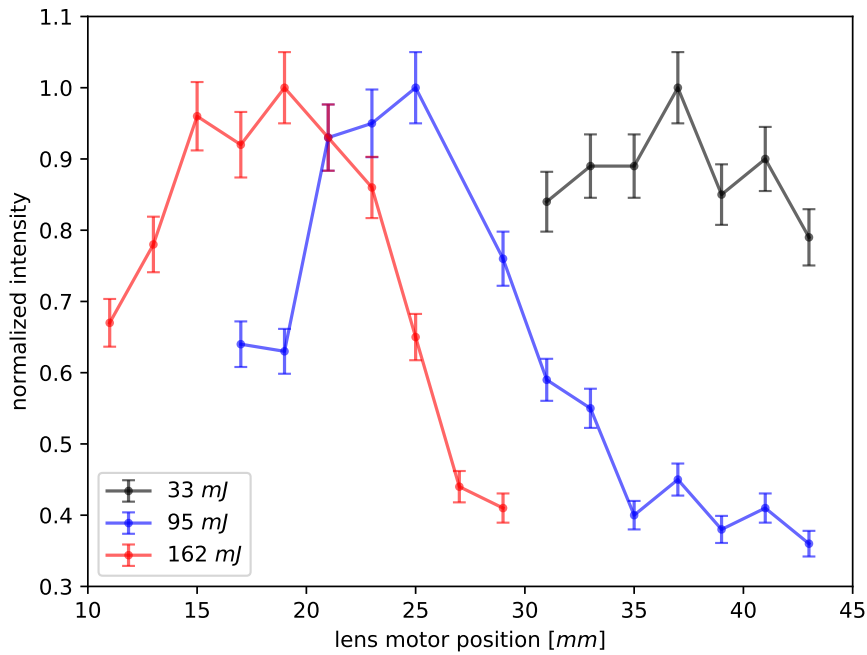


**Figure 4.15.:** Normalized plasma intensity against the lens separation for different laser pulse energies at 1 mbar hydrogen pressure. Each measurement was averaged over 20 shots. The error bars indicate the RMS from fluctuations.

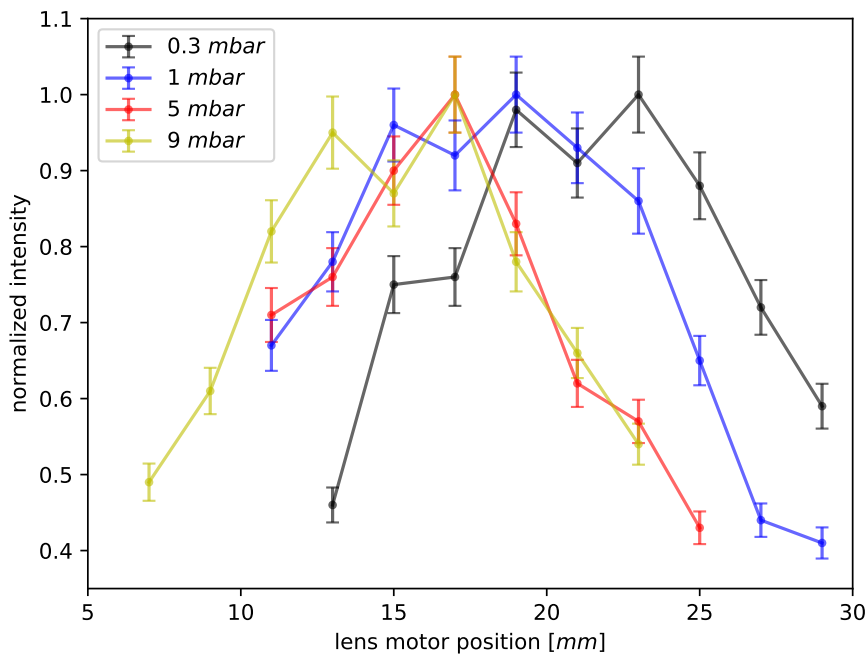


**Figure 4.16.:** Normalized plasma intensity against the lens separation for different gas pressures inside the ITC at 162.4 mJ pulse energy. Each measurement was averaged over 20 shots. The error bars indicate the RMS from fluctuations.

## 4. Experimental Setup

---

also reveals an astigmatism, where the horizontal focus position is more influenced by the laser power than the vertical focus position. Furthermore, the Rayleigh length seems to decrease for higher energies (see figure 4.10). The focal spot itself at an energy of 94.8 mJ is shown in figure 4.13. It only shows a variation in the intensity distribution of up to  $\sim 16\%$  between the highest and lowest used laser pulse energy, as can be seen from figure 4.14, which shows the difference of the normalized focal spot images at 189.9 mJ and 16.3 mJ, with both images adjusted to have the same center. The measured spot size gives an intensity of up to  $6.17 \cdot 10^{14} \text{ W/cm}^2$  at the highest energy used, with an average pulse length of 40 fs.

A shift in the focus position was also observed under experimental conditions with a gas-filled chamber. Here, the lens separation had to be adjusted at different energies to achieve maximum interaction of the laser with the gas. This is shown in figure 4.15, where the normalized integrated signal intensity of the plasma emission is plotted against the lens motor position. The lenses had to be moved closer together at higher intensities to maintain the intensity of the plasma emission, which corresponds to moving the focus further downstream of the laser. A similar, but smaller, effect can be observed when the gas pressure inside the chamber is increased (see figure 4.16). This suggests that non-linear focusing effects due to the optical Kerr effect are occurring inside the gas (see chapter 2.1.4 or e.g. Esarey, Sprangle, Krall, and Ting (1997)). The fact that the laser's peak power in the above measurements is well above the critical power of  $P_N \simeq 2.8 \text{ GW}$  for self-focusing<sup>14</sup> in air at atmospheric pressure supports this hypothesis. Furthermore, an estimation of the B integral over 1 m in air yields a value  $\gg 1$ , which means that nonlinear effects will occur, even at much lower pressures.

### 4.5.2. Pointing Stability

Since the laser is being focused over almost 18 m and is supposed to hit a target not much larger than its focal diameter, the pointing stability of the system is of particular importance.

The focus position on target in one dimension can be extracted from the spectrometer images of the plasma emissions, as long as the imaging direction is transverse to the laser propagation axis, as was the case for the spectrometer setup (see figure 4.3) used in the measurements presented in the following. The vertical focus position is extracted by fitting a Gaussian to the transverse intensity profile and deriving the center position of the resulting function. Due to the imaging from one side, horizontal pointing fluctuations cannot be resolved.

---

<sup>14</sup> $P_N = \lambda^2 / 2\pi n_0 n_2$ , where  $\lambda$  is the laser wavelength.  $n_0$  and  $n_2$  are the linear and non-linear index of refraction, respectively.

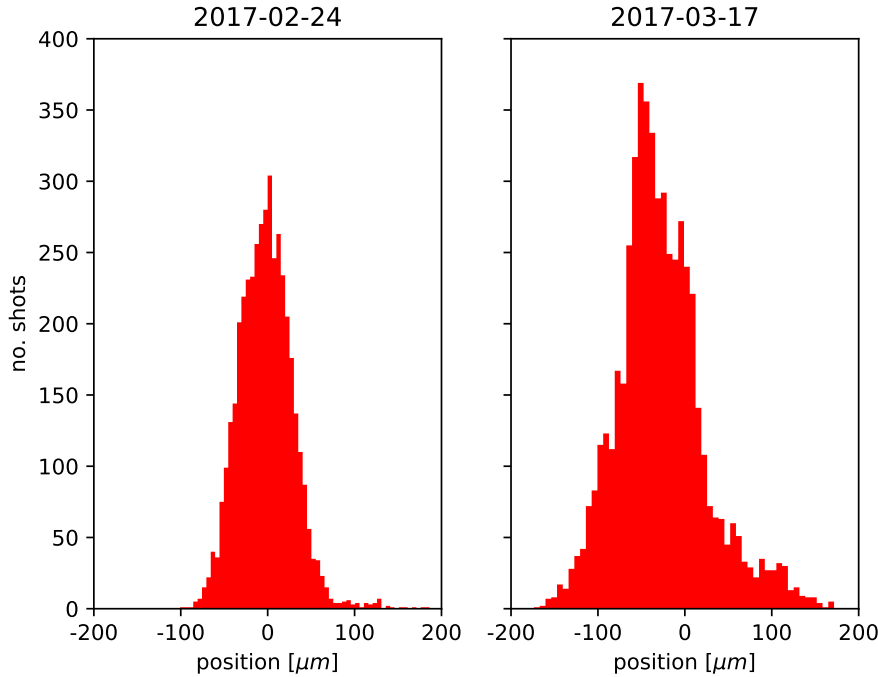


**Figure 4.17.:** Histograms of the vertical position of the plasma as measured with the spectrometer on February 24th, 2017 at 142.6 mJ pulse energy (left) and on March 17th, 2017 at 94.8 mJ pulse energy (right).

The analysis was done for several thousand shots with two different pulse energies and roughly one month apart, as shown in figure 4.17. Taking all shots into account, the RMS deviations for these two cases are  $63.56 \mu\text{m}$  (2.5% error) and  $111.50 \mu\text{m}$  (3.2% error), respectively. This represents  $\sim 9\%$  and  $\sim 16\%$  of the focus diameter of  $\sim 700 \mu\text{m}$ , respectively, which is of some concern for the experimental scenarios envisaged. However, for all shots within the  $1/e^2$  width of the two distributions, their respective RMS deviations are only  $27.96 \mu\text{m}$  ( $\sim 4\%$  of the focus diameter) and  $47.07 \mu\text{m}$  ( $\sim 7\%$  of the focus diameter). This means that only a small fraction of the shots deviate significantly from their design axis. The peak-to-peak fluctuations of up to  $\sim 600 \mu\text{m}$  might still cause problems, such as damage to the optical elements or the gas target. These absolute fluctuations convert to an angular pointing error of up to  $\sim 2.6 \mu\text{rad}$  RMS ( $\sim 33 \mu\text{rad}$  peak to peak) which agrees well with the pointing error directly at the laser output<sup>15</sup> of  $3.3 \mu\text{rad}$  RMS.

<sup>15</sup>with a beam diameter of 450 mm



# Experimental Results

---

The method of spectroscopic electron density determination described in chapter 3 has only recently been used for plasma acceleration applications with measurements by Filippi *et al.* (2016), which took place shortly after they visited FLASHForward to learn about this technique in 2015. This chapter will show a comparison of the different approaches to convert the spectral line width to an electron density based on measurements. Furthermore, temporally and spatially resolved electron-density measurements with high relative accuracy carried out on capillary-discharge plasmas and laser-induced plasmas will be presented.

Section 5.1 describes how the spectral-line profiles were analyzed and discusses the resulting errors. The comparison of the different approaches on calculating the electron density as well as the characterization of the capillary-discharge plasmas is presented in section 5.2. Finally, section 5.3 covers the characterization of the laser-based plasma generation on the ionization test beamline for FLASHForward.

## 5.1. Method of Analysis and Error Considerations

Except for the comparison of the different methods for electron-density determination from spectral-line profiles at the beginning of section 5.2, all electron densities provided in the following sections were obtained from the  $H_\alpha$  linewidth using the GC model (Gigosos and Cardeñoso, 1996, see chapter 3.2.2) for a temperature of 20 000 K. The  $H_\beta$  line could not be used to determine the electron density. In the case of the capillary discharge plasmas, the  $H_\beta$ -line profiles were obstructed by the spectral lines of aluminum and oxygen caused by the ablation of the capillary walls (see section 5.2.1), and in the case of the laser-generated plasmas, the  $H_\beta$ -line intensity was too weak and therefore the signal was too noisy without significantly increasing the exposure time and thereby sacrificing temporal resolution. The line width was determined by fitting a Lorentzian to the data and taking the FWHM of the fit. Examples of the residuals of the fits to the measured line profiles of a capillary discharge plasma (see section 5.2 at different pressures are shown in figure 5.1. They show a small deviation from the data at the peak and in the left flank that grows with increasing pressure. However, this deviation is within an error of  $\sim 10\%$ , except for the left end of the profiles, which is due to the continuous background caused by recombination, and at the lowest pressure of 5 mbar, which is due to the noise. The fact that the shape of the spectral lines did

## 5. Experimental Results

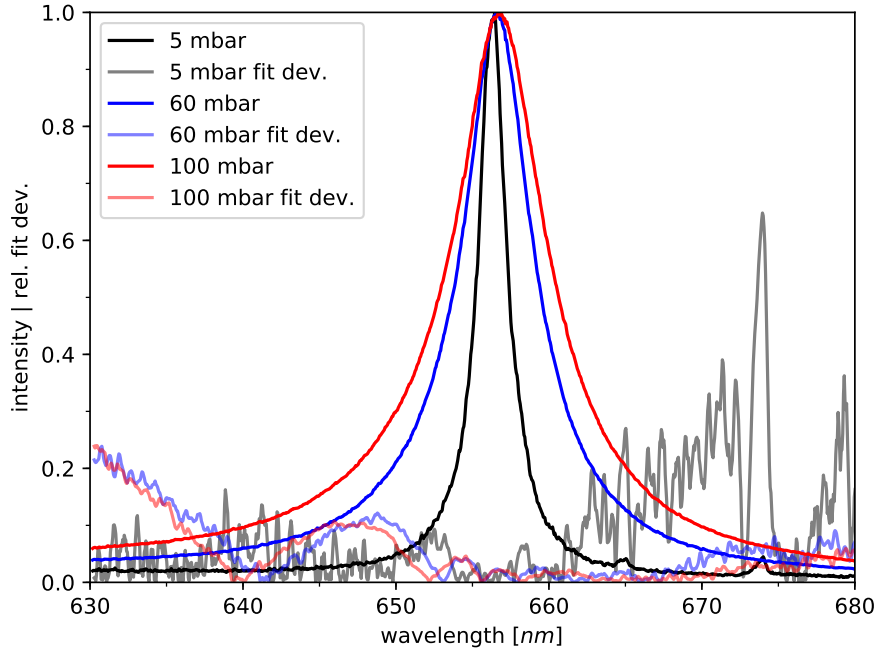


**Figure 5.1.:** Measured  $H_\alpha$  line profiles of capillary-discharge plasmas at different pressures and the residuals of their respective Lorentzian fits.

not change significantly shows that the dominating broadening mechanism in the plasmas investigated in this work is linear Stark broadening and that ion dynamics are negligible. This supports the assumption that the plasmas investigated in this work are indeed *'two-temperature'* non-equilibrium plasmas. Since the fits were less sensitive to noise, thereby improving the statistical error of measurements with weak signal, the line widths used to calculate the electron density were obtained from the fits. The shift of the spectral lines was obtained by subtracting the vacuum wavelength of the  $H_\alpha$  line of  $656.279 \text{ nm} \pm 0.003 \text{ nm}$  according to the National Institute of Standards and Technology (NIST) atomic spectra database (Kramida *et al.*, 2017, <https://www.nist.gov/pml/atomic-spectra-database>) from the central wavelength of the Lorentzian fit.

In all measurements presented in the following sections, the error due to shot-to-shot fluctuations of the laser and discharge parameters as well as the gas density were taken into account. In case of the *capillary-discharge plasmas*, the fluctuation of the discharge current proved to be very small ( $\sim 1\%$ ) due to the high stability of the PFN. However, the uncertainty in the applied pressure of up to 15% (depending on the pressure range) had to be taken into account for measurements requiring a long time period. The *laser-induced plasmas* were subject to larger fluctuations on the order of 10%, due to the fluctuations in the laser's pointing and energy. The uncertainty in the applied

hydrogen pressure was only on the order of 1 % due to improvements in the gas-supply system undertaken after the capillary measurements. As detailed in chapter 3.2, the uncertainty of the shift method is approximately 10 %, the uncertainty of the GKS model depends on the pressure range (between over a factor of 2 for  $n_e \sim 10^{15} \text{ cm}^{-3}$  and 10 % for  $n_e \sim 10^{19} \text{ cm}^{-3}$ ), while the GC model has an uncertainty of approximately 5%. Furthermore, the limitations of the optical setup and the spectrometer introduce some systematic errors to all measurements. The spectral resolution of the spectrometer of 0.05 nm introduces an uncertainty of  $1.7 \cdot 10^{17} \text{ cm}^{-3}$  when calculating the electron density from the shift of the central wavelength and an uncertainty  $\simeq 10^{15} \text{ cm}^{-3}$  when calculating the electron density from the line width using both the GKS model (see chapter 3.2.1) and the GC model (see chapter 3.2.2). Thereby, the line width is the more sensitive parameter for the determination of the electron density.

The spatial uncertainty is given by the resolution of the optical setup of  $10 \mu\text{m}$  (see section 4.2). This error is not plotted for the measurements involving spatial distributions for clarity. Due to the depth of field of the imaging system, the spectra are averaged over a depth of  $\sim 100 \mu\text{m}$  (see chapter 4.2.1). The difference in time between the commencement of the discharge and the capture of the emission spectra was accurate to  $\leq 1 \text{ ns}$ . The same was true for the difference in time between the laser arrival and the capture of the emission spectra.

## 5.2. Capillary Discharge Plasmas

This section covers measurements made on capillary-discharge plasma cells commonly used for laser wakefield acceleration due to their pulse-guiding properties (see section 2.2.4) which lead to a prolonged region of high laser intensity and therefore a longer acceleration region (see e.g. Esarey, Sprangle, Krall, and Ting, 1997). These cells can also be used to focus electron bunches or beams due to the magnetic field created by the current (active plasma lens, see e.g. Hairapetian *et al.* (1994) and Tilborg *et al.* (2015)).

First measurements were made with standard capillaries of  $200 \mu\text{m}$  diameter and 15 mm length filled homogeneously with hydrogen at different pressures. A 400 ns (FWHM) discharge was generated with the PFN charged to 20 kV. The spectrometer was set up such that the direction along the capillary was spatially resolved with an exposure time of 5 ns per image. For analysis, the images were integrated along their spatial axis (which corresponds to the capillary axis) to improve the signal-to-noise ratio, since only a small spatial variation of  $< 3\%$  could be observed. This can be seen in the region between 4 mm and 10 mm of the spatially resolved density measurements at homogeneous pressure in figure 5.12 in section 5.2.3.

## 5. Experimental Results

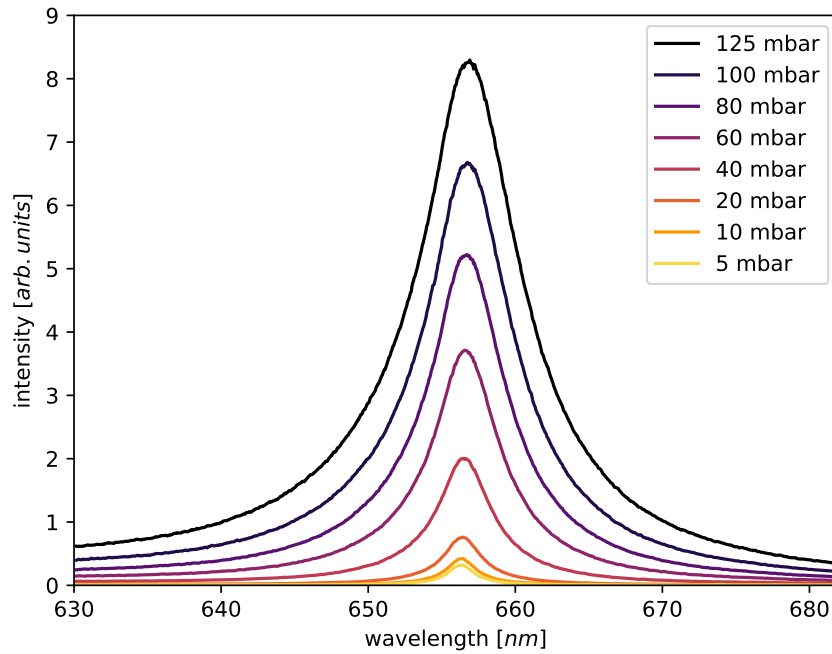


Figure 5.2.: Measured H $\alpha$  line profiles for different pressures. Raw data without fit.

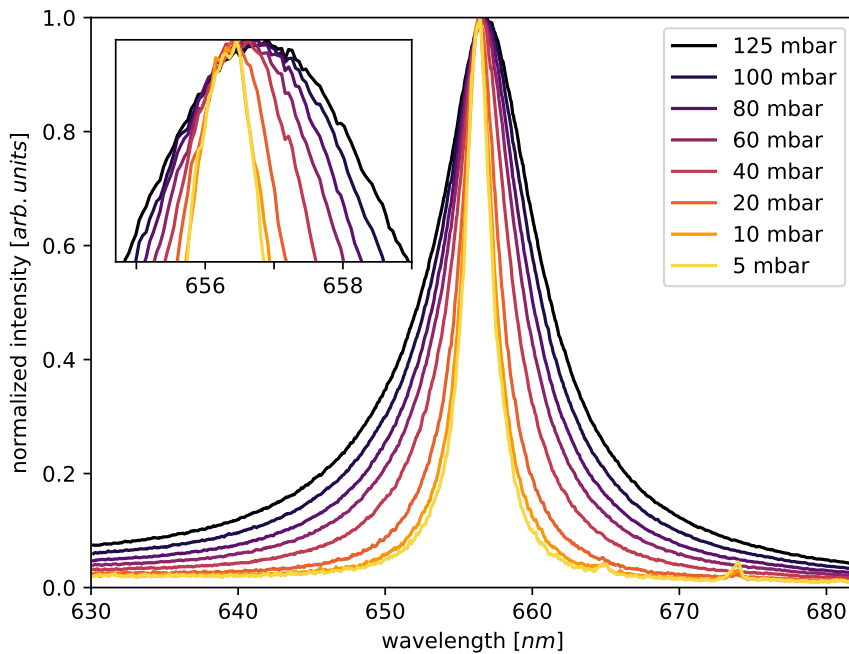
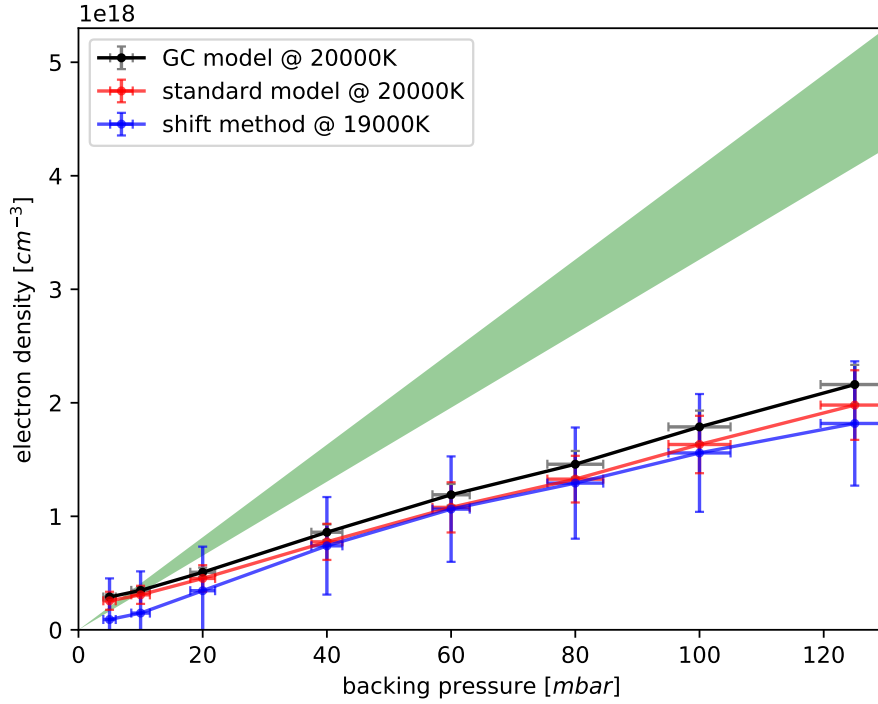


Figure 5.3.: Normalized measured H $\alpha$  line profiles for different pressures. The inset is a magnification of the graph peaks. Raw data without fit.

The influence of different electron densities on the  $H_{\alpha}$  line (656.27 nm) is shown in figure 5.2, where line profiles for applied pressures between 5 mbar and 125 mbar shortly after plasma creation (at the time of peak density) are plotted. Intensity and linewidth both increase with pressure. The increase in linewidth is more evident in figure 5.3, where all line profiles are normalized to their respective maximum. The shift of the line center towards longer wavelengths is also visible here and can be seen clearly in the magnified plot at the top left of figure 5.3.

A comparison of the different methods to determine the electron density is shown in figure 5.4, where the peak electron densities derived shortly after the commencement of the discharge (cf. section 5.2.2) at the given pressures are plotted. The integration time was set to 5 ns. The images were spatially averaged along the capillary axis and over a depth of  $\sim 100 \mu\text{m}$  (see chapter 4.2.1). The green area represents the theoretically expected electron densities. Full ionization of the hydrogen gas at the applied pressure was assumed as the upper limit, which is warranted by the amount of energy introduced to the hydrogen gas by the discharge. The lower limit is given by 80 % full ionization. This ionization limit was found in 1D magnetohydrodynamics (MHD) simulations of the discharge setup performed by Röckemann *et al.* (2018) at a current of 400 A for a capillary of 500  $\mu\text{m}$  diameter filled with hydrogen at 4 mbar. Since a 1D simulation cannot take expansion of the gas or a change in radial density into account, the result is only an estimate of the degree of ionization. Furthermore, the lower limit of 80 % is justified by the pressure gradient between the gas reservoir, where the pressure was measured, and the capillary, an effect which increases with applied pressure and was observed during the joint experiments with Messner (2015) utilizing direct measurement of the pressure inside the capillary.

The results of all three methods agree well with each other within their respective errors. The electron density was calculated from the shift using equation (3.11) with  $d_0 = 0.29 \cdot 10^{-17}$  (from Callaway and Unnikrishnan, 1991) for a temperature of  $1.9 \cdot 10^4$  K. The error bars in the y-direction indicate the fluctuations and the uncertainty of the conversion method as well as the systematic error, which is large compared to the other methods ( $1.7 \cdot 10^{17} \text{ cm}^{-3}$ ), due to the spectrometer not being able to properly resolve the sub-nanometer shift. The results agree well with the density calculation from the linewidth using the standard model (see section 3.2.1, equation (3.2)), where the parameter  $\alpha_{1/2}$  was chosen from table 3.1 for a temperature of  $T \simeq 2 \cdot 10^4$  K, corresponding to  $\sim 1.7$  eV. This is well within the temperature range of 1 eV to 2 eV given by Ashkenazy, Kipper, and Caner (1991) for their capillary plasma and the temperature range of 1 eV to  $\sim 3$  eV given by the MHD simulations by Röckemann *et al.* (2018). However, since the temperature could not be determined for the plasmas characterized in this work, the error bars in y-direction for this measurement also indicate the un-



**Figure 5.4.:** Comparison of the peak density values obtained from the  $H_{\alpha}$ -line width shortly after the commencement of the discharge using the GC model (chapter 3.2.2, black), the standard model (chapter 3.2.1, blue), and the shift method (chapter 3.2.3, red). The integration time was set to 5 ns. The images were spatially averaged along the capillary axis and over a depth of  $\sim 100 \mu\text{m}$  (see chapter 4.2.1). The green area represents the theoretically expected values with the upper limit of full ionization and the lower limit is given by 80% full ionization as found in 1D magnetohydrodynamics (MHD) simulations of the discharge setup performed by Röckemann *et al.* (2018) at a current of 400 A for a capillary of 500  $\mu\text{m}$  diameter filled with hydrogen at 4 mbar. The lines are to guide the eye. Each point has an associated error bar representing the fluctuations and systematic error as discussed in section 5.1 in the y-direction as well as the uncertainty in  $n_e$  due to the unknown temperature of the plasma. The uncertainty in the backing pressure leads to an error in the x-direction.

certainty in the electron density due to the unknown temperature, in addition to the systematic error and fluctuations discussed in section 5.1. The electron-density values obtained using the GC model (chapter 3.2.2, equation 3.5) using the power law for  $2 \cdot 10^4$  K also agree well with the other two methods. This shows that ion dynamics only have a small impact on pure hydrogen plasmas. However, the inclusion of ion dynamics and 'two-temperature' plasmas in the GC model (Gigosos and Cardeñoso, 1996) render this model theoretically more useful for plasma acceleration experiments, where gas mixtures are often used for advanced electron injection schemes.

It can also be seen that the graphs of the GC and standard model, when extrapolated to lower pressures, do not intersect with (0,0), but show an offset of  $2.04 \cdot 10^{17} \text{ cm}^{-3}$ . This offset in electron density is due to additional electrons being produced by the discharge ablating the capillary walls, as described in the next section (5.2.1). Furthermore, taking the ablation into account, the degree of ionization of the hydrogen gas inside the capillary is only between 25 % to 27 % at all backing pressures. This is significantly lower than the ionization degree of 80 % estimated from MHD simulations and also lower than the results of Gonsalves *et al.* (2007) which showed an ionization degree of  $\sim 44$  %.

### 5.2.1. Influence of Ablation

Rowlands-Rees *et al.* (2008) have suggested that the capillary discharge produces aluminum and oxygen ions which, in their case, allowed for ionization-based injection of electrons into the wakefield. This theory is supported by spectral lines within the plasma emissions presented in this thesis that cannot be attributed to hydrogen. Figures 5.5, 5.6, 5.7 and 5.8 show spectra taken of the Balmer  $H_\beta$  line (486 nm) at different times during the discharge and for the same pressures as the time-dependent measurements presented in the next section 5.2.2 (cf. figure 5.11), namely 75 mbar, 50 mbar, 25 mbar, and  $\ll 5$  mbar. They all exhibit additional peaks between 460 nm and 475 nm with the highest intensities at  $\sim 461$  nm,  $\sim 466$  nm, and  $\sim 471$  nm. According to the NIST Atomic Spectra Database (Kramida *et al.*, 2017) these lines can be attributed to the following elements:

**Aluminum (Al II)** from the sapphire ( $\text{Al}_2\text{O}_3$ ) the capillary is made of. It has an intense line at  $\sim 466$  nm.

**Oxygen (O II)** from the sapphire the capillary is made of, which has multiple lines around  $\sim 461$  nm, 464 nm to 467 nm and 470 nm to 471 nm.

**Copper (Cu II)** from the electrodes, with the most intense lines in this region between 466 nm and 468 nm.

## 5. Experimental Results

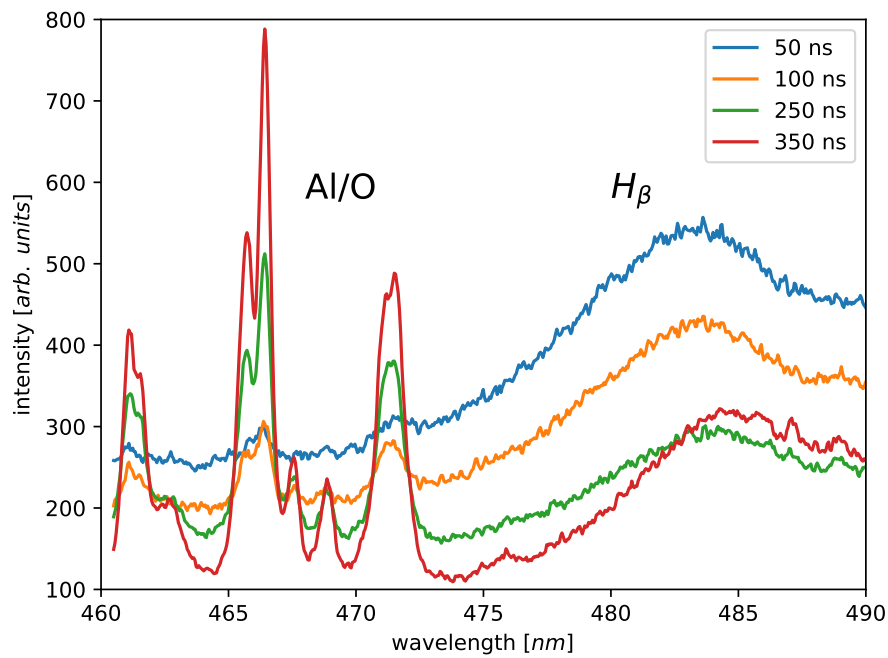


**Figure 5.5.:** Spectra of the capillary-discharge emission at 75 mbar in the vicinity of the  $H_{\beta}$  line (486 nm) at different times after the commencement of the discharge. The data is averaged over 20 shots.

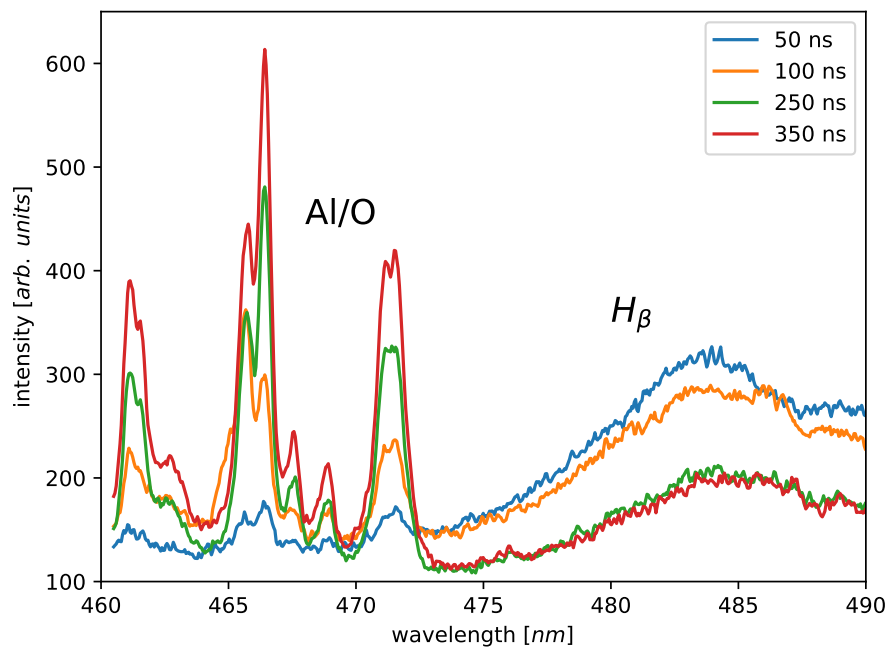


**Figure 5.6.:** Spectra of the capillary-discharge emission at 50 mbar in the vicinity of the  $H_{\beta}$  line (486 nm) at different times after the commencement of the discharge. The data is averaged over 20 shots.

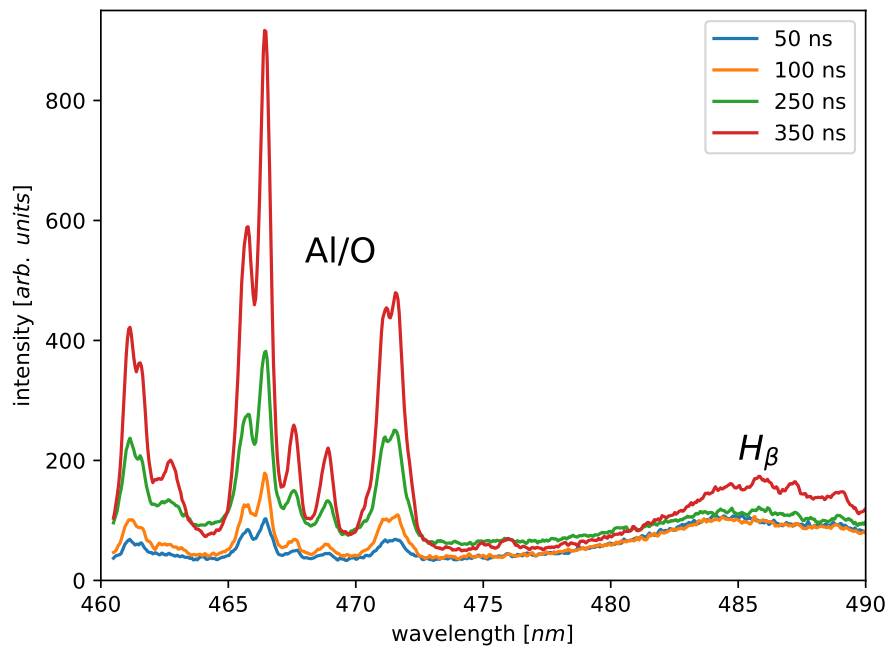


**Figure 5.7.:** Spectra of the capillary-discharge emission at 25 mbar in the vicinity of the  $H_{\beta}$  line (486 nm) at different times after the commencement of the discharge. The data is averaged over 20 shots.

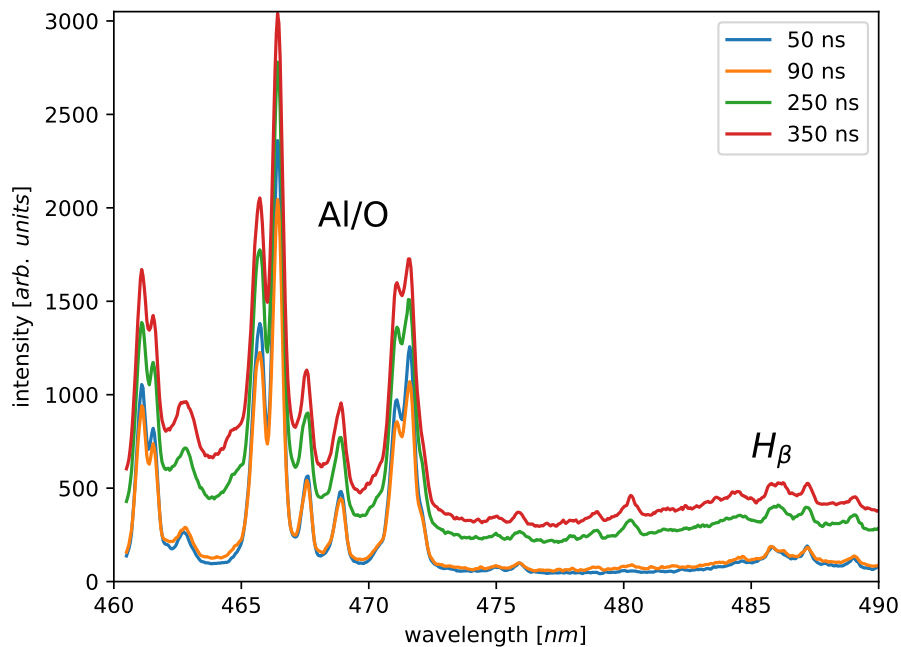


**Figure 5.8.:** Spectra of the capillary-discharge emission at  $\ll 5$  mbar in the vicinity of the  $H_{\beta}$  line (486 nm) at different times after the commencement of the discharge. The data is averaged over 20 shots.

## 5. Experimental Results

---

The contribution from the sapphire dominates, since it is homogeneously available over the length of the capillary.

The temporal evolution of the peak intensity of the aluminum line at  $\sim 466$  nm for different pressures, with the  $H_\beta$  background subtracted, is depicted in figure 5.9. The discharge current is shown in grey. The camera settings for the measurements at 75 mbar, 50 mbar and 25 mbar were identical, with an exposure time of 5 ns. Therefore, the results are directly comparable. At  $\ll 5$  mbar, the exposure time of the camera had to be changed to 10 ns to get sufficient signal. This has been taken into account in figure 5.9 by dividing the corresponding data by 2. At all pressures, the three most intense non-hydrogen-related lines are already visible 50 ns after the commencement of the discharge. Furthermore, they show similar intensities over the  $H_\beta$  background. In each case, the intensity of the aluminum line increases during the discharge and reaches its peak towards the end of the discharge. These observations agree well with the measurements of the temporal evolution of the electron density shown in the next section 5.2.2 (cf. figure 5.11). Here, towards the end of the discharge, the electron densities at low pressures (25 mbar and below) have their maximum and the densities at higher pressures (50 mbar and above) exhibit a plateau.

Another observation from figure 5.9 is that at the lowest applied pressure of  $\ll 5$  mbar, the absolute intensity and its evolution between 0-100 ns are significantly different from the intensities and their evolution at all other pressures, which are approximately the same until  $\sim 350$  ns. Firstly, the overall intensity of the aluminum line at  $\ll 5$  mbar is higher than at the higher pressures. This indicates different plasma parameters for this low hydrogen pressure, since the intensity of the plasma emissions is highly dependent on the plasma temperature and composition (Griem, 1997). Secondly, at  $\ll 5$  mbar, the intensity increases rapidly during the first  $\sim 100$  ns of the discharge and afterwards increases approximately linearly, while at higher pressures, the intensity increases linearly from the start. The slope of this linear increase, from the time at which the discharge current reaches its plateau ( $\sim 80$  ns after the commencement of the discharge) until shortly before the end of the discharge (at  $\sim 350$  ns) is approximately the same in all cases. The different intensity evolution during the first  $\sim 100$  ns at  $\ll 5$  mbar indicates a possible change in the type of discharge due to the low hydrogen density. At the beginning, the main part of the discharge current is transported via the sapphire surface inside the capillary. When the ablation has created a sufficiently dense plasma for the discharge current to be transported through the capillary volume, the discharge behaves as in the cases of higher hydrogen pressure, with the difference that the bulk of the plasma consists of aluminum and oxygen ions and electrons.

The sudden rise in intensity for all pressures at the end of the discharge ( $> 350$  ns) can be attributed to the sudden change in the discharge current, which causes rapid

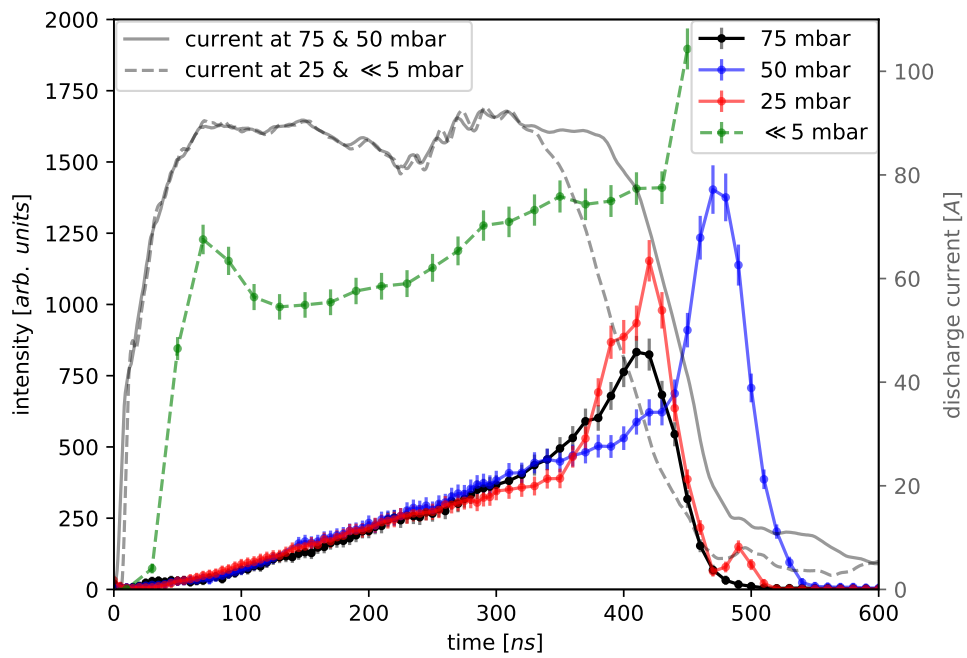


**Figure 5.9.:** Intensity evolution over time of the aluminum line at  $\sim 466$  nm for different pressures. The discharge current is shown in grey. The data is averaged over 20 shots. The lines are to guide the eye.

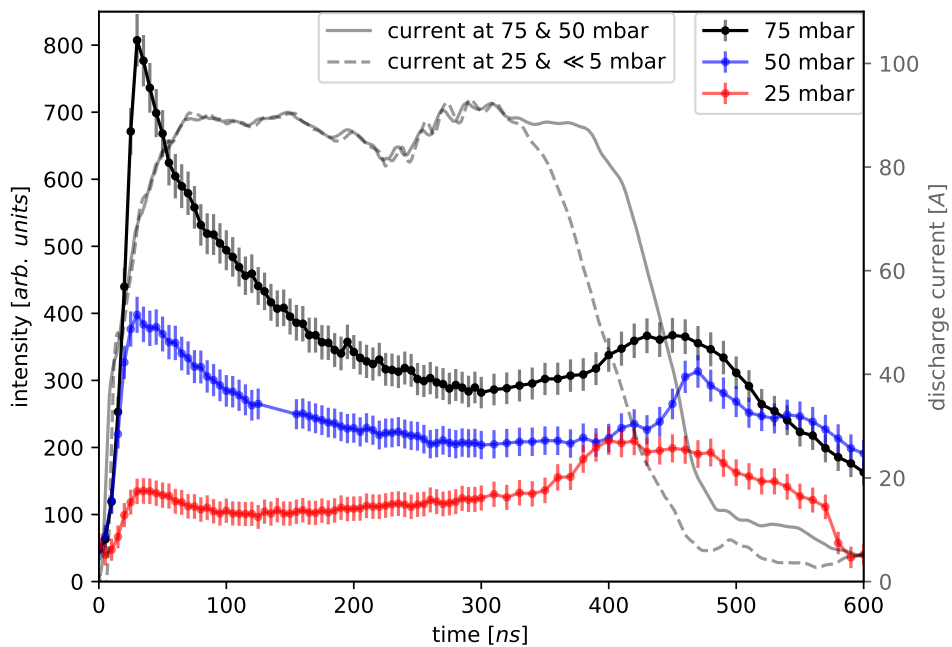


**Figure 5.10.:** Intensity evolution over time of the  $H_{\beta}$  line at  $\sim 486$  nm for different pressures. The discharge current is shown in grey. The data is averaged over 20 shots. The lines are to guide the eye.

## 5. Experimental Results

---

changes in the plasma properties, such as electron density (see figure 5.11), temperature, optical density, and electron energy distribution. It also supports complex interactions such as quenching (Salzberg *et al.*, 1991). While not as pronounced, this increase in intensity at the end of the discharge can also be observed in the intensity evolution of the  $H_\beta$  line, as shown in figure 5.10. Therefore, this effect is not aluminum specific and supports the statement that the rapidly changing plasma conditions at the end of the discharge current are responsible for the increase in intensity and not an increase in the plasma density. It is also noted that the overall evolution of the intensity of the  $H_\beta$  line at all pressures, up to  $\sim 350$  ns, is similar to the electron-density evolution measurements presented in figure 5.11. Therefore, the intensity evolution can give an estimate of the plasma density evolution during the time where the discharge current is roughly constant, which provides sufficiently stable conditions.

The linear increase over time in the intensity of the aluminum line at 466 nm for all pressures correlates with the increase in electron density at  $\ll 5$  mbar in the measurements presented in the next section (figure 5.11). Since the measured electron density is up to 2 times higher than expected for fully ionized pure hydrogen at 5 mbar inside the capillary, the bulk of the plasma consists of aluminum and oxygen ions and electrons from the ablation of the sapphire. Therefore, if the contribution of the hydrogen to the plasma is neglected, a linear fit of the electron density evolution at  $\ll 5$  mbar can be used to approximate the rate at which plasma from the sapphire is produced. The fit of the region between 70 ns and 350 ns, in which the electron density linearly rises and which approximately matches the duration in which the intensity of the aluminum line at all pressures linearly rises, yields  $1.29 \cdot 10^{15} \text{ cm}^{-3} \text{ ns}^{-1}$ . Multiplied by the capillary volume, this gives a rate of  $\sim 4.88 \cdot 10^{11} \text{ ns}^{-1}$  for the creation of electrons from the sapphire.

### Conclusion

These measurements show that the plasma does contain aluminum and oxygen ions from ablation of the sapphire the capillary is made of. This behavior has been suspected by Rowlands-Rees *et al.* (2008) before, but could not be conclusively proven. The intensity evolution of the aluminum line at 466 nm indicates a linear increase in the amount of aluminum inside the plasma over the duration of the discharge. Furthermore, correlating the intensity evolution to the evolution of the electron density at a very low pressure presented in the next section allowed for an estimation of the rate at which electrons are produced from the sapphire.

### 5.2.2. Temporal Plasma Evolution

The high accuracy of the spectroscopy method in combination with the short integration times of down to 5 ns that can be achieved with the iCCD allows detailed studies of the temporal evolution of the plasma. For plasma dynamics that take place on a timescale  $< 5$  ns (see e.g. Lemos *et al.*, 2013), this yields only an averaged temporal distribution.

Figure 5.11 shows these temporal scans for pressures of 75 mbar, 50 mbar and 25 mbar homogeneously applied to a capillary of 200  $\mu\text{m}$  diameter and 15 mm length. Each data point of the density<sup>1</sup> represents data taken with 5 ns integration time that has been averaged over 20 shots. The error bars represent the fluctuations and systematic error as discussed in section 5.1, plus the uncertainty in the backing pressure due to the gas supply system. Additionally, a measurement with the lowest possible density at which a discharge would still stably occur is shown (indicated by " $\ll 5$  mbar"). This was achieved by lowering the pressure of the gas supply system to its minimum of 5 mbar and closing an additional needle valve as far as possible while maintaining the discharge. Unfortunately, the exact pressure inside the capillary is unknown in this measurement, since the pressure was measured before the extra valve and the pressure sensor is not suitable for such low pressures. Here, the integration time for each shot was increased to 10 ns to compensate for the lower intensity of the plasma emission. This sacrifices some of the temporal resolution but still allows for a good measurement of the general evolution, since this timescale is still short compared to the discharge timescale. The signal was found to be weak at the beginning and end of the discharge, which is why this measurement does not extend over the same time period as the others. The discharge current through the capillary is shown in grey and was also averaged over 20 shots. Since the currents at 75 mbar and 50 mbar were indistinguishable, they are represented by the same graph. The same is true for the currents at 25 mbar and below. The ripples in the current plots around 300 ns are caused by a reflection<sup>2</sup> in the PFN that arrives at this time. It can be seen that the discharge is about 50 ns (FWHM) shorter for pressures of 25 mbar and below. This is due to the longer required ignition time at lower densities which effectively shortens the discharge (see Goldberg, 2013).

Apart from the maximum density achieved, the measurements at 75 mbar and 50 mbar exhibit similar main features. When the discharge current begins to rise, the electron density immediately also rises, with the density reaching its maximum shortly before the current. Over the next  $\sim 200$  ns, the electron density linearly decreases and reaches a 100 ns- to 200 ns-long plateau before further decreasing until the current is terminated. The decrease in density over the whole discharge is caused by thermal expansion of

<sup>1</sup>obtained from the  $H_{\alpha}$  line using the GC model as described in section 5.1

<sup>2</sup>Reflections are caused by improper matching of the impedance of the capillary to the wave impedance of the PFN.

## 5. Experimental Results

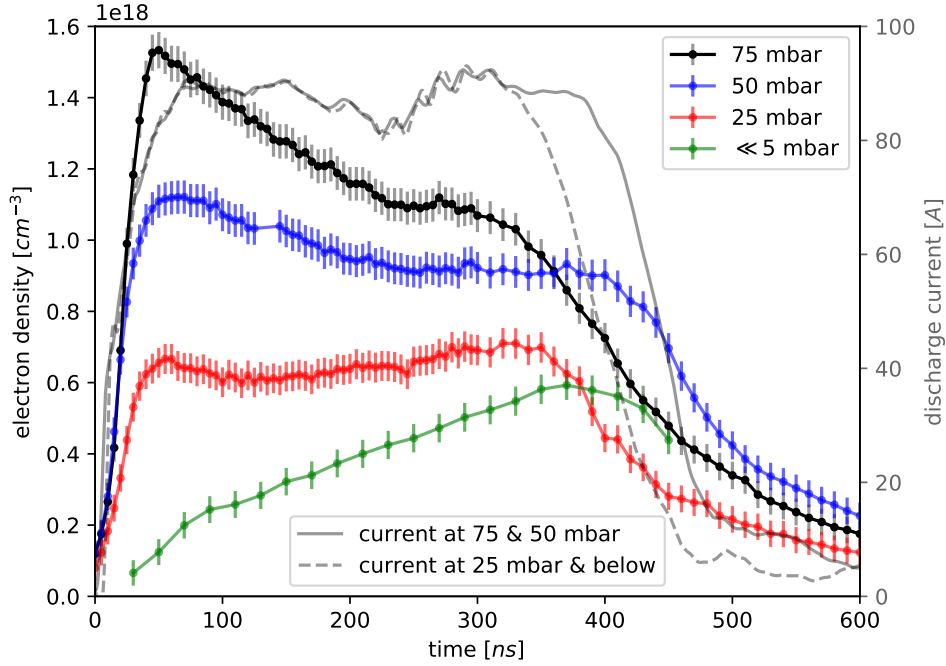


**Figure 5.11.:** Temporal plasma-density evolution inside the capillary for various applied pressures. The grey lines represent the discharge current. Each point has an associated error bar representing the fluctuations and systematic error as discussed in section 5.1, plus the uncertainty in the backing pressure introduced by the gas supply system.

the plasma out of the capillary into the vacuum. The density evolution is slightly different at 25 mbar. At the beginning of the discharge, the density also quickly rises and reaches a first peak just before the maximum current is reached. However, the following decrease is shorter than at higher pressures and the density begins to increase again afterwards until it reaches a global maximum shortly before the end of the discharge. This trend continues for even lower applied pressures. With the lowest possible amount of gas inside the capillary, the electron density increases almost linearly over the full length of the discharge until a density of  $\sim 6 \cdot 10^{17} \text{ cm}^{-3}$  is reached. The approximate corresponding pressure of 10 mbar for fully ionized hydrogen is far higher than the actual applied pressure of  $\ll 5$  mbar.

These observations support the conclusions of the previous section, that the ablation of the sapphire provides additional electrons. Aluminum lines were already visible shortly after the commencement of the discharge (at  $\sim 50$  ns, see figure 5.9), and the increasing intensity of the aluminum and oxygen lines over time matches the increase in electron density at  $\ll 5$  mbar. Since the measured electron density is significantly higher than expected for  $\ll 5$  mbar of hydrogen inside the capillary, the majority of the plasma electrons come from the ablation of the sapphire. A linear fit of the electron density evolution suggests that the ablation increases the electron density at a rate

of  $1.29 \cdot 10^{15} \text{ cm}^{-3} \text{ ns}^{-1}$ . This equals a rate of  $\sim 4.88 \cdot 10^{11} \text{ ns}^{-1}$  for the creation of electrons. Furthermore, the times at which the linear increase of the intensities of the spectral lines at all pressures ends (around 400 ns) correspond to the times in the respective electron-density evolution shortly before the end of the discharge, where the densities start to decrease rapidly. This means that the generation of additional electrons through ablation counteracts the decrease in electron density due to thermal expansion.

### Conclusion

The results of this section confirm the influence of ablation, which is important for two reasons. Firstly, using a capillary-discharge plasma by filling the capillary with gas at the desired density and assuming an electron density in the plasma corresponding to calculated or measured degrees of ionization, as is usually done due to the lack of suitable on-the-fly diagnostics, will underestimate the actual electron density, in particular at low densities. Secondly, the ablated sapphire provides additional ion species which might enable injection mechanisms that would otherwise not occur. This effect has been suspected to occur by Rowlands-Rees *et al.* (2008), but proof has been missing so far.

The precise measurements of the temporal evolution of the electron density presented in this section provide insight into the plasma dynamics and their influence on different delays between the wakefield driver and the discharge. Furthermore, the knowledge of the temporal density evolution is important for capillary-discharge waveguide applications and active plasma lenses, since their properties are highly dependent on the electron density (see chapter 2.2.4).

### 5.2.3. Spatial Plasma Distribution and Gas Mixtures

In addition to the high temporal resolution, the use of an imaging spectrometer also permits measurements of the spatially resolved plasma distribution in one direction.

The following measurements were made using a 15 mm long, 200  $\mu\text{m}$  diameter capillary with two simple inlets. Although the imaging optics were selected to image the whole capillary onto the spectrometer slit, approximately 1 mm was cut off on each side due to distortions in the image. The area of interest between the gas inlets was fully and clearly covered. The images taken were binned over 10 pixel ( $\simeq 370 \mu\text{m}$ ) intervals along the capillary to enhance the signal-to-noise ratio. This was done directly on the camera chip to avoid the accumulation of read-out noise.

## 5. Experimental Results

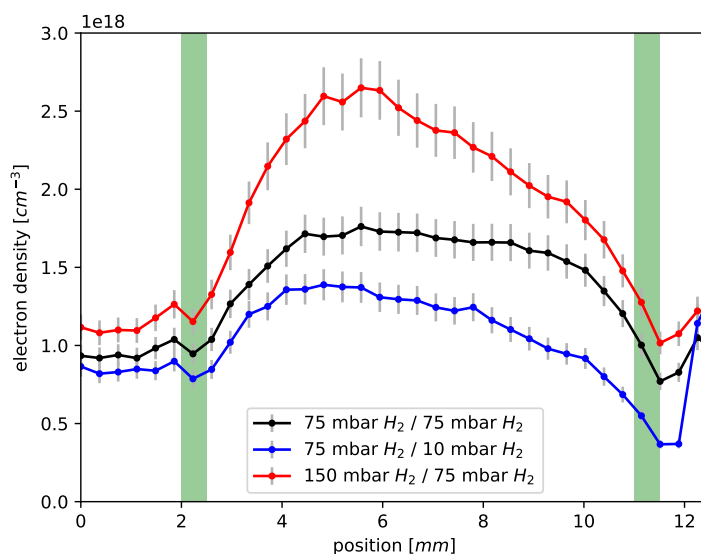


**Figure 5.12.:** Spatial capillary density profiles of density ramps for pressures between 10 mbar and 150 mbar of hydrogen applied to the inlets (green) as specified in the legend. Each point is averaged over 20 shots and has an associated error bar representing the fluctuations and systematic error (see section 5.1) plus the uncertainty in the backing pressure introduced by the gas supply system.

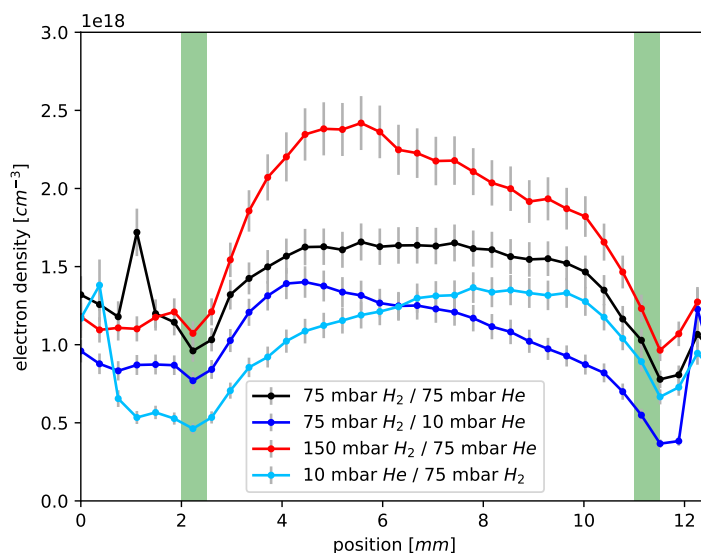


**Figure 5.13.:** Capillary density profiles for pressures of 75 mbar and 150 mbar hydrogen applied to the left inlet and pressures of 10 mbar and 75 mbar Helium applied to the right inlet (green), as specified by the legend. The light-blue plot shows a profile where helium was supplied to the left inlet and hydrogen to the right inlet. The green areas mark the inlets. Each point is averaged over 20 shots and has an associated error bar representing the fluctuations and systematic error (see section 5.1) plus the uncertainty in the backing pressure introduced by the gas supply system.

Figure 5.12 shows density profiles obtained shortly after the start of the discharge at the time of maximum density, where different pressures were applied to each inlet (marked in green). The blue plot shows a measurement with 75 mbar and 10 mbar applied to the left and right inlet, respectively, and the red plot shows a measurement with 150 mbar and 75 mbar applied to the left and right inlet, respectively. Additionally, a measurement with 75 mbar applied to both inlets is shown in black. As expected, if equal pressure is applied to both inlets, a flat density plateau is created in between the inlets, as has been shown in fluid-dynamics simulations (Schwinkendorf, 2012) and Raman-spectroscopy measurements (Schaper *et al.*, 2014) of the gas density distribution in the capillaries. These simulations and measurements also showed that the gas density drops significantly between each inlet and the nearer exit. The measurements depicted in figures 5.12 and 5.13 show that the same is not true for the electron density, which stays constant in these regions and in some cases even increases. This is due to the electrons propagating outwards at a different rate than unionized gas molecules and it is possibly accompanied by the propagation of shock waves induced by the discharge, which have been observed in argon and argon-nitrogen glow discharges at  $\sim 67$  mbar by Macheret *et al.* (2001).

A ramp in electron density can be created by applying a different pressure to each inlet. In this case, the densities in the vicinity of the inlet with the higher applied pressure is lower than if this pressure is applied equally to both inlets. This is due to the gas and plasma flow from the high pressure region to the low-pressure region. Furthermore, the density in the vicinity of the inlet with the lower pressure is significantly higher than if the pressures of 10 mbar and 75 mbar were applied to both inlets, respectively. This is due to the ablation and the gas flow from the high-pressure region on the left side of the capillary to the low-pressure region on the right side. It should also be noted that the plasma density has its peak not at the gas inlets, as predicted by gas density measurements (Schaper *et al.*, 2014) but approximately 2 to 3 mm further inward. This is explained by the higher mobility of the plasma electrons compared to the gas molecules, which enables a higher flow rate out of the capillary.

Plasmas created from mixtures of hydrogen with other gases can also be examined with this measurement method, as long as the hydrogen fraction is high enough to produce line intensities sufficient for detection by the spectrometer. Figure 5.13 shows the spatial electron-density distribution for different pressures of hydrogen applied to one inlet and helium to the other. With the combination of spectrometer and camera used here, the resulting slopes in density can easily be measured as long as at least as much hydrogen as helium is present. Unfortunately, once the helium pressure exceeds the hydrogen pressure, the helium displaces the hydrogen and the signal of the  $H_{\alpha}$  line gets too weak for an accurate measurement of the linewidth and therefore density. In

this case, the helium lines give a stronger signal. They are similarly influenced by the plasma electron density as the hydrogen lines (see e.g. Griem, Baranger, *et al.*, 1962; Dimitrijevic and Sahal-Br  chot, 1984), but to the author’s knowledge, no established method for deriving the electron density from the helium-line profiles exists. However, with a more sensitive spectrometer setup or by sacrificing temporal resolution for longer integration times, the hydrogen-line profiles could be used to determine the electron densities of plasmas generated from any gas, even when the density of hydrogen within the plasma is only on the order of  $10^{14} \text{ cm}^{-3}$ . The measured spatial density distributions shown in figure 5.13 are basically the same as those for the pure hydrogen sample (cf. figure 5.12), apart from a larger error (up to 20%) in the region of the exits and a smaller peak density of the red plot. The larger error can be attributed to the lower intensity of the  $H_{\alpha}$  line since less hydrogen is present. Furthermore, the measurement at equal helium and hydrogen pressure suggests that the helium is also fully ionized, since the electron density near both inlets is approximately equal and therefore both gas species have to contribute the same number of electrons to the plasma.

### Conclusion

It was shown that the spectroscopic electron-density determination can provide detailed insight into the electron-density distribution along the longitudinal direction of the capillary, which has not been done before. This knowledge is essential for plasma-accelerator applications such as density-downramp injection (Suk *et al.*, 2001), dephasing control (Rittershofer *et al.*, 2010), and controlled release of the electron into the vacuum (Mehrling, 2014). Furthermore, the ability to determine the electron-density distribution of mixtures of hydrogen with other gases is important for applications such as ionization injection (e.g. Oz *et al.*, 2007; Pak *et al.*, 2010; McGuffey *et al.*, 2010) or laser-assisted density-downramp injection, where an additional laser beam further ionizes a dopant gas inside the plasma (e.g. helium, argon or nitrogen) and thereby creates a density peak that enables density downramp injection (Wittig *et al.*, 2015).

### 5.3. Laser-Induced Plasmas

This section covers measurements done on the test beamline for laser-induced plasma generation at FLASHForward, as described in section 4.1, to gain knowledge of how the laser-generated plasma evolves and which densities can be achieved. The measurement method was the same as described in section 5.1 and demonstrated in section 5.2.

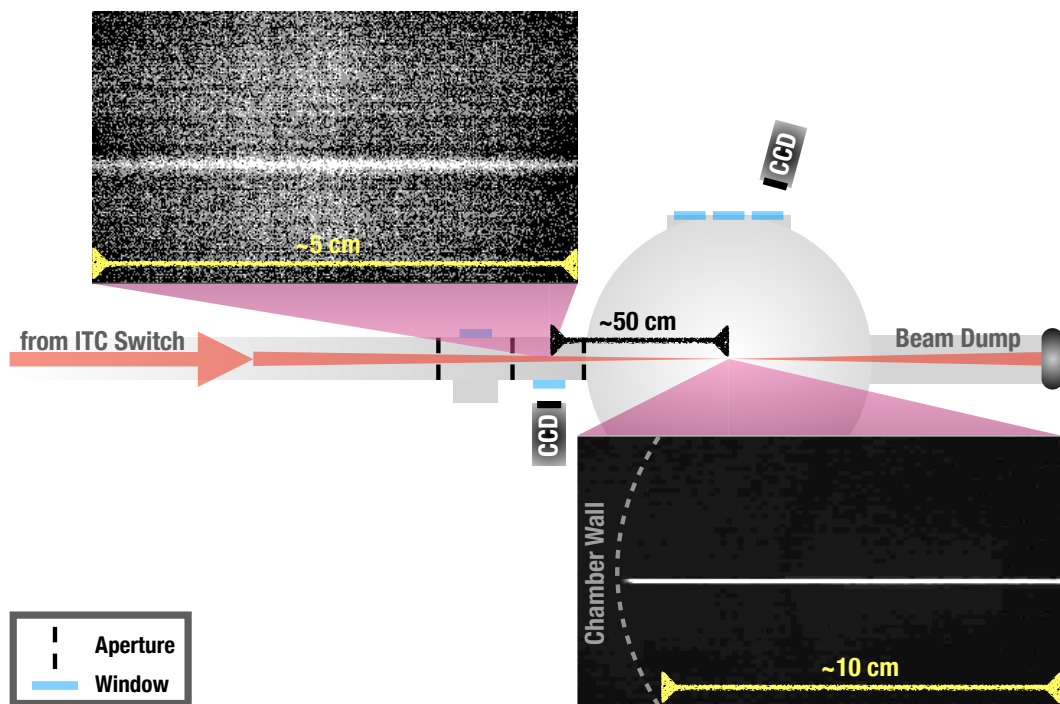


**Figure 5.14.:** Schematic of the CCD camera positions for first interaction tests including images of the plasma.

### 5.3.1. Possible Length of the Plasma Channel

Initial ionization tests were conducted by just filling up the volume of the ionization test chamber (ITC, see section 4.1.2) with hydrogen gas and firing the focused laser into it. The generation of plasma was observed by two CCD cameras. One looked into the center of the ITC, the other into the first differential pumping section (see figure 5.14). At the achievable pressures of up to 15 mbar in the ITC, the plasma could always be observed on the first camera, even though the laser focus was set to be in the center of the ITC. This indicates a plasma length of at least 50 cm, which is the distance between the center of the first differential pumping section and the center of the ITC. It has to be kept in mind that the pressure in the differential pumping section is significantly lower than that in the ITC. Nonetheless, these observations show that the presented setup can ionize hydrogen over tens of centimeters, which is essential for the gas targets that are planned for use at FLASHForward.

### 5.3.2. Plasma Lifetime and Temporal Evolution

The plasma lifetime and temporal evolution are important for later applications. The knowledge of these properties enables the correct timing of the arrival of the electron

## 5. Experimental Results

---

bunch with respect to the plasma and allows the maximum repetition rate at which the plasma can be regenerated to be estimated. The plasma lifetime is defined as the time until the intensity, which is proportional to the density, reaches  $1/e^2$  of the starting value.

Measurements of the  $H_\alpha$  line at various pressures of hydrogen inside the gas cube have been performed for times ranging from the laser arrival at the chamber to the point where no more signal could be obtained. The data points were taken at intervals increasing from 10 ns at the beginning of the discharge up to 200 ns at the end of the plasma lifetime, since the plasma evolves more rapidly shortly after creation than at later times. The integration time was set to 10 ns. Figure 5.15 shows how the intensity of the  $H_\alpha$  line evolves for different pressures. As expected, the plasma lifetime decreases with increasing pressure due to the shorter mean free path of the electrons and therefore faster cooling of the plasma (Margetic *et al.*, 2000; Yalçın, Tsui, and Fedosejevs, 2004). The plasma lifetime at the given pressures can be estimated from the exponential fits to the intensity evolution. These estimations yield lifetimes of 149.96 ns, 76.45 ns, 55.35 ns, and 26.60 ns for the given pressures of 10 mbar, 15 mbar, 20 mbar, and 40 mbar, respectively. At low pressures of  $\leq 10$  mbar, plasma emissions were measured up to  $1 \mu\text{s}$  after the laser arrival<sup>3</sup>, which is far longer than needed and suggests a repetition rate threshold of less than  $\sim 1$  MHz for acceleration experiments to assure that the laser creates the plasma from neutral hydrogen gas and does not heat an existing plasma.

Figure 5.16 shows how the density decreases over time for applied pressures between 10 mbar and 40 mbar. The measured density evolution is best fitted by an exponential function with a linear offset. It has its maximum at the time of creation of the plasma and after approximately 20 ns, the electron densities reach values on the order of  $1.4 \cdot 10^{16} \text{ cm}^{-3}$  which lie within 15 % of each other, independent of the backing pressure. The densities then slowly drop over the following few 100 ns until the intensity of the  $H_\alpha$  line is too weak for the camera to detect. This temporal evolution of the average plasma density is caused by the temporal evolution of the spatial plasma profile transverse to the laser direction, as shown in the next section (5.3.3). Shortly after the laser arrival the transverse plasma profile is approximately the same width as the laser focus and has its peak density on the laser axis. The plasma then rapidly expands, its profile becomes flat with only narrow density peaks at the edges of the plasma, and the density on axis approaches  $\sim 1.4 \cdot 10^{16} \text{ cm}^{-3}$  after  $\sim 40$  ns. This temporal density evolution means that if the desired operating density occurs within the first 20 ns after the creation of the plasma, the timing between the laser and the electron bunch has to be accurate on the sub-nanosecond level to be certain to avoid large fluctuations in the

---

<sup>3</sup>with the exposure time set to 10 ns and the gain maxed on the iCCD

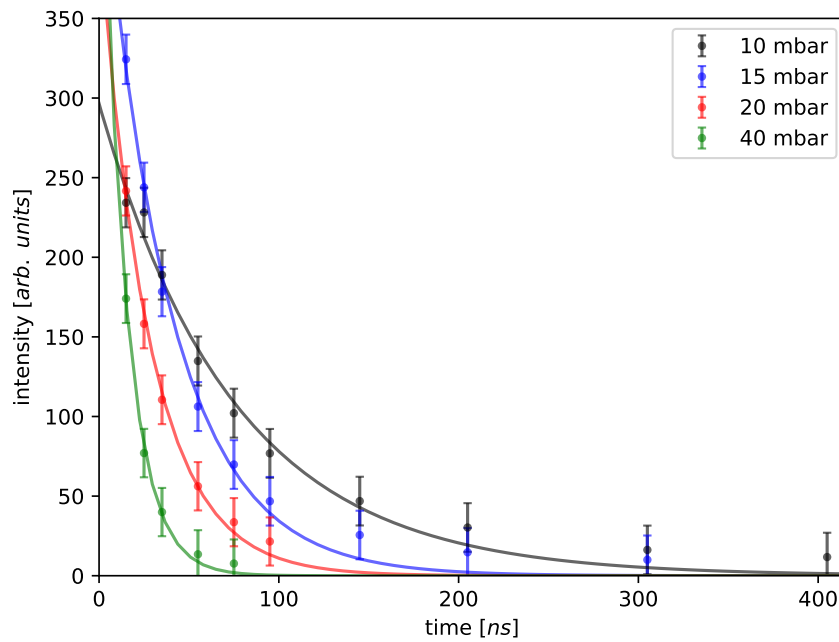


**Figure 5.15.:** Evolution of the plasma emission intensity for different pressures inside the gas cube. The solid lines indicate exponential fits. The errorbars indicate the uncertainty due to the shot to shot fluctuations.

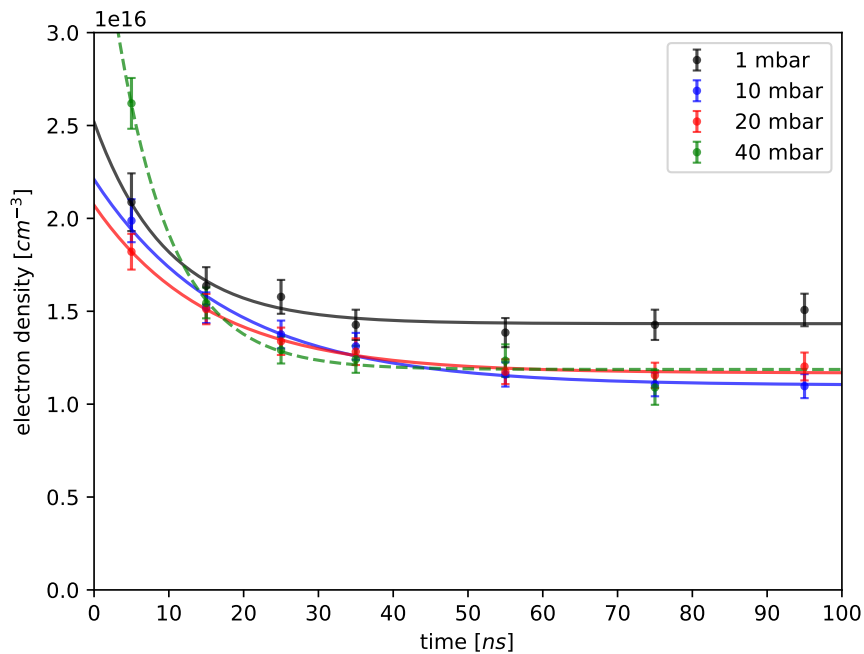


**Figure 5.16.:** Density evolution over time at different applied hydrogen pressures at 94.8 mJ laser-pulse energy. The lines indicate an exponential fit. The measurement at 40 mbar was taken with a fresh set of apertures in the gas cube. The errorbars indicate the fluctuations and systematic error (see section 5.1).

## 5. Experimental Results

---

electron density between shots. The laser and electron bunch at FLASHForward are designed to coincide to better than 100 fs. This is still to be demonstrated.

Curiously, the density during the first 10 ns after the creation of the plasma (see figure 5.16) appears to decrease with increasing pressure. Furthermore, the measured peak electron densities are significantly lower than expected for full ionization of the hydrogen gas at the given pressures. Since all measurements were conducted with the same laser energy of 94.8 mJ, this can be explained by the laser passing an increasing amount of gas inside the ITC, differential pumping section, and beam pipe and therefore losing more energy before reaching the cube. Background pressures inside the ITC of up to 3 mbar were observed for the pressures of up to 40 mbar applied to the cube. Since fully ionizing a cylindrical volume of 25 cm long and 700  $\mu\text{m}$  in diameter<sup>4</sup> filled with hydrogen at 1 mbar takes approximately 20 mJ, this means that the laser can lose up to  $2/3$  of its energy before reaching the gas cube. An exception to the decreasing electron density with increasing backing pressure is the measurement at 40 mbar applied pressure which shows initially a significantly higher density compared to the other measurements. Since a heavily used set of windows<sup>5</sup> after several thousand shots did not allow for such a high pressure without exceeding the pressure limits of the beamline, a new set of thin windows for the laser entrance and exit was installed before the measurements at 40 mbar. This led to smaller apertures and therefore lower gas flow out of the cube, which resulted in a lower gas density inside the ITC, differential pumping section, and beam pipe. Thereby, the laser lost less energy before reaching the cube and was able to produce a higher density plasma.

Due to the fast evolution of the electron density during the first  $\sim 20$  ns after creation and the exposure time of 10 ns of the spectrometer, the measured electron density at these times represents a temporal average. Besides the increasing gas load, this is another reason for the measured electron densities being lower than expected for full ionization. Therefore, this setup is not suitable for accurate measurements of the electron density of laser-induced plasmas at early times. Since the electron density only evolves slowly and approximately linearly from 20 ns to 30 ns (see figure 5.16), the measurements are accurate at late times. Since the operating density of FLASHForward is on the order of  $10^{16} \text{ cm}^{-3}$  to  $10^{17} \text{ cm}^{-3}$ , these observations suggest that experiments should be performed during the time of slow plasma evolution if this density diagnostic setup is used and accurate knowledge of the electron density is required.

---

<sup>4</sup>approximately the diameter of the laser focus

<sup>5</sup>The diameter of the holes made by the laser increases over time due to the pointing fluctuations.

### 5.3.3. Spatial Evolution

In FLASHForward, a laser is used to create the plasma in order to be able to shape the electron density and create well defined density profiles in a confined space. To achieve this, the temporal evolution of the spatial plasma profile has to be known. This can also be investigated with the spectroscopy setup.

Figure 5.17 shows how the  $1/e^2$  width of the plasma channel evolves over time at different backing pressures. It can be seen that the plasma starts to expand immediately after creation and continues to do so until the emission is too weak to be measured. This hydrodynamic expansion is due to the rapid heating of the plasma by the laser and is faster the higher the backing pressure, since the higher initial plasma density leads to a higher plasma-density gradient. The initial width of the plasma channel approximately matches the width of the laser focus (see chapter 4.5). A similar expansion behavior can be observed when varying the laser energy, as shown in figure 5.18. This plot also clearly shows that the initial width of the plasma increases with the laser-pulse energy. This is due to the fact that the intensity in the flanks of the laser pulse increases with higher energy, the pulse thus being able to ionize over a wider region.

Measurements of transverse electron-density profiles are shown in figures 5.19, 5.20 and 5.21 for hydrogen pressures of 1 mbar, 15 mbar and 40 mbar, respectively. To improve the signal-to-noise ratio, the camera was set to bin over 4 rows of pixels in the spatial direction directly on the chip. This did not reduce the spatial resolution, since the average distance imaged to 4 pixels was  $7.24\ \mu\text{m}$ , which is well below the resolution of the optical system of  $10\ \mu\text{m}$ . The plasma dynamics are most obvious at 1 mbar (figure 5.19). In the first 10 ns after creation, the transverse density profile has its maximum on the laser axis. However, it changes to a channel with its minimum on axis within the first 20 ns. This channel grows deeper and wider over the lifetime of the plasma. This effect is again due to the hydrodynamic expansion of the plasma and has been used to create guiding channels for LWFA applications in the past (see e.g. Durfee III and Milchberg, 1993). The origin of the modulation of the electron density, which is most obvious at 0-10 ns, is unknown. However, it is not a statistical variation since the measurements are averaged over 100 shots. The effect of plasma channel formation seems less pronounced at higher pressures and the transverse density profile is mostly flat. However, due to the faster expansion of the plasma at higher densities and the 10 ns integration time of the spectrometer setup, the initial plasma evolution could not be resolved. Therefore, measurements at high densities only show an already fully developed plasma profile. The increase in density at the edge of the profiles from 10 ns onward indicate the shock front propagating outwards as described by, for example, Lemos *et al.* (2013). Furthermore, the integral over the density profile grows over time, which indicates that additional electrons are created through impact ionization within

## 5. Experimental Results

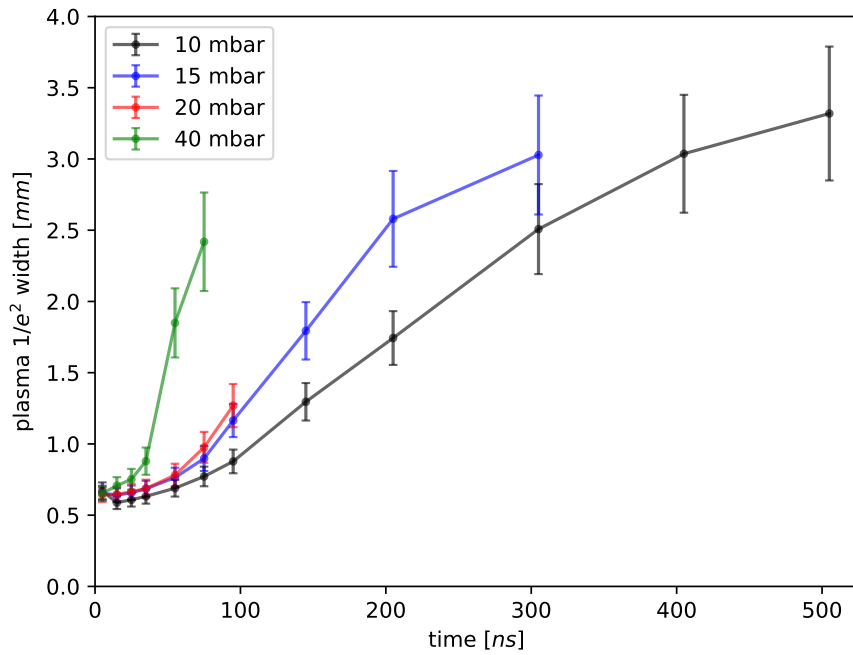


**Figure 5.17.:** Evolution of the transverse plasma  $1/e^2$  width over time for different pressures at 94.8 mJ laser pulse energy. The data is averaged over 100 shots and the error bars indicate the fluctuations and systematic error (see section 5.1).

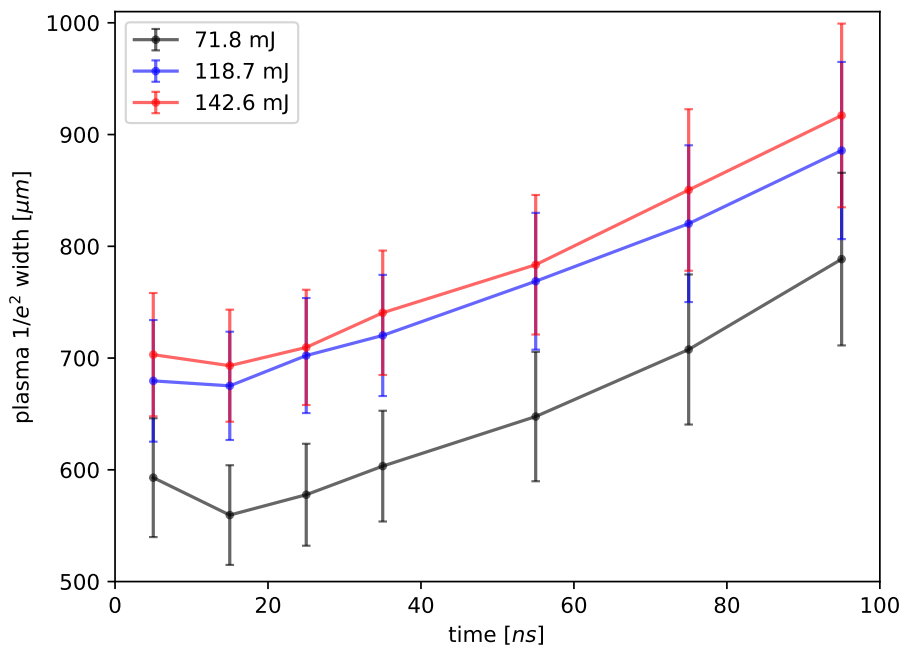


**Figure 5.18.:** Evolution of the transverse plasma  $1/e^2$  width over time for three different laser energies at 10 mbar hydrogen pressure. The data is averaged over 100 shots and the error bars indicate the fluctuations and systematic error (see section 5.1).

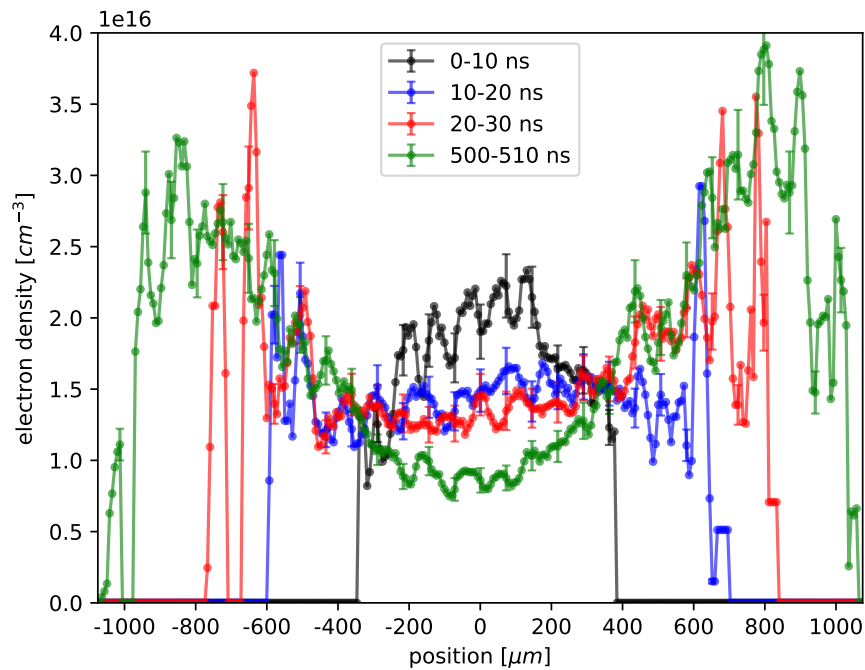


**Figure 5.19.:** Transverse plasma evolution over time at 1 mbar hydrogen pressure averaged over 100 shots per timing. The error bars, shown only on every tenth point for clarity, indicate the fluctuations and systematic error (see section 5.1).

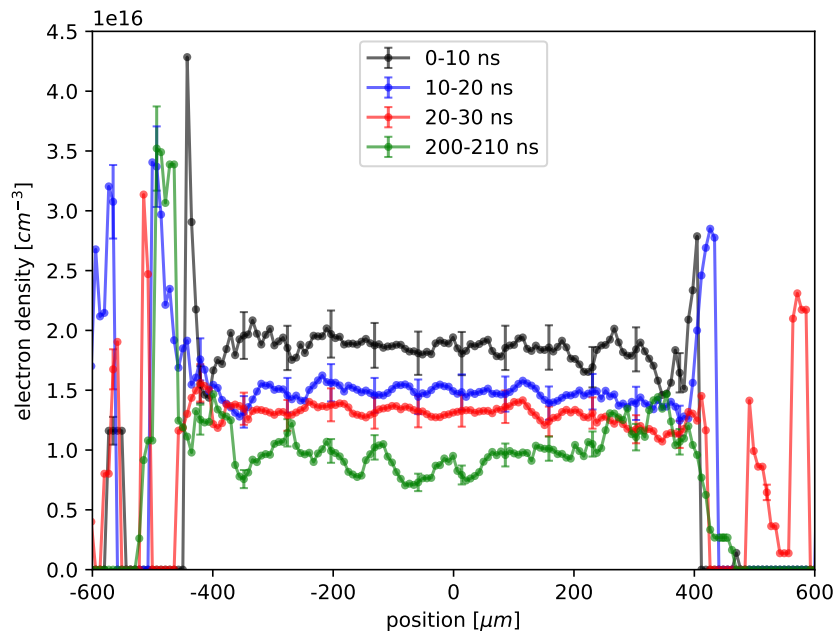


**Figure 5.20.:** Transverse plasma evolution over time at 15 mbar hydrogen pressure averaged over 100 shots per timing. The error bars, shown only on every tenth point for clarity, indicate the fluctuations and systematic error (see section 5.1).

## 5. Experimental Results

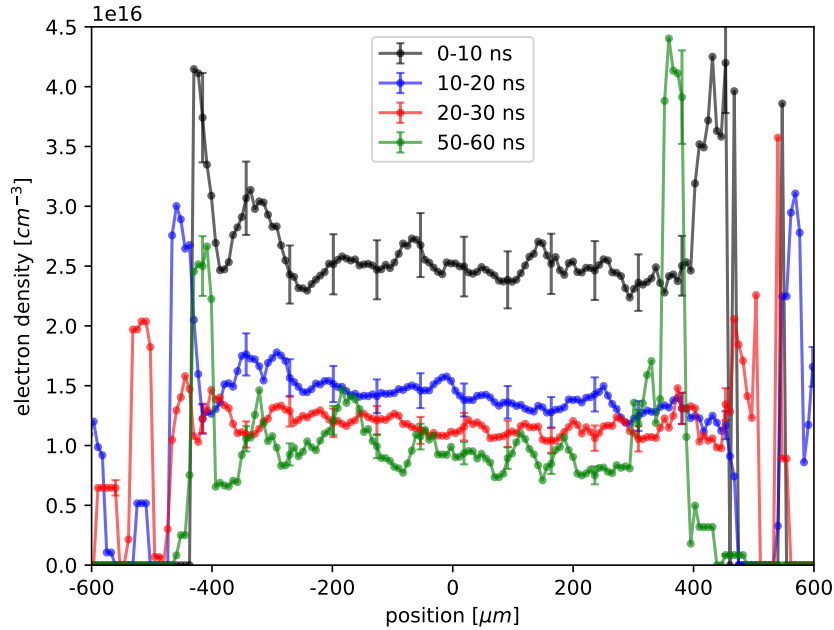


**Figure 5.21.:** Transverse plasma evolution over time at 40 mbar hydrogen pressure averaged over 100 shots per timing. The error bars, shown only on every tenth point for clarity, indicate the fluctuations and systematic error (see section 5.1).

the shockwave.

Combining these observations with the results of section 5.3.2 yields the conclusion that stable and, with  $< 10\%$  spatial variation, approximately flat transverse electron-density profiles can be obtained by letting the plasma expand for 20 ns to 40 ns after creation. In this case, an increase in the backing pressure only slightly influences the electron density on axis, which stays within 15% of  $1.4 \cdot 10^{16} \text{ cm}^{-3}$  for all pressures that have been investigated, but leads to a wider electron channel due to the faster expansion at higher pressures. Therefore, this technique can be used to create plasma channels of various widths at the same electron density.

### 5.3.4. Investigating Lower Than Expected Peak On-Axis Densities

A calibration of the Stark-broadening measurements against interferometric measurements and theoretical calculations is foreseen for the future, since the simulations by Griem, Kolb, and Shen (1959) did not cover non-equilibrium states and there are no comparisons of the simulations by Gigoso and Cardeñoso (1996) to experimental data. The planned calibration measurements rely on interferometry, which depends on the accumulated phase shift between the beam passing through the plasma and the reference beam. For a given laser wavelength, this depends on the electron density and

the length of the beam path through the plasma. In the case of the laser-induced plasmas of  $\sim 700 \mu\text{m}$  width investigated in this thesis, an  $\sim 800 \text{ nm}$  probe beam requires densities  $\geq 10^{17} \text{ cm}^{-3}$  (Kaganovich *et al.*, 1999; Spence, Burnett, and Hooker, 1999; Jones *et al.*, 2003; Gonsalves *et al.*, 2007), which theoretically should have been reached with the setup. As already discussed, the on-axis electron density measured with the spectroscopy method did not change much over the investigated pressure range. Since the plasma was shown to start expanding directly after its creation (see figure 5.17), this seemingly constant measured plasma density is explained by the rapid hydrodynamic expansion of the plasma during the 10 ns long integration time, as mentioned in section 5.3.3. The formation of the plasma channel has been shown to occur within  $\sim 2 \text{ ns}$  after the plasma was created by a femtosecond laser pulse (Lemos *et al.*, 2013) and leads to an order of magnitude decrease in peak density. The effect is illustrated in figure 5.22, where the peak<sup>6</sup> transverse density profiles at different pressures are shown. Even for pressures as high as 40 mbar, the measured density stayed in the  $10^{16} \text{ cm}^{-3}$  region when the theoretical value for full ionization is  $\sim 2 \cdot 10^{18} \text{ cm}^{-3}$ . Even increasing the laser energy on target had little or no effect (cf. figure 5.23). The electron density never seemed to reach the theoretically possible  $5 \cdot 10^{17} \text{ cm}^{-3}$  for the applied pressure of 10 mbar, though an increase in density was observable and the plasma channel significantly gained in width while the laser focal spot size remained unchanged.

In an attempt to confirm the long integration time as the reason for these low observed electron densities, further possible explanations were evaluated by taking measurements of the laser energy, spectrum, and pulse length after the lenses while increasing the laser pulse energy. Figure 5.24 shows that for energies above the lowest setting (16.3 mJ), an increasing fraction of the laser pulse spectrum is shifted towards shorter wavelengths. Furthermore, the spectrum of the laser pulse increasingly fluctuates in intensity with increasing laser energy, which can be seen in figures 5.25, 5.26 and 5.27. At the lowest energy setting of 16.3 mJ, the maximum standard deviation is already 14%. It increases to 33% and 42% for 94.8 mJ and 189.9 mJ, respectively. This is an indication for non-linear effects strengthening as the increasingly intense laser pulse passes through the lenses. The lenses are on average 3.3 mm thick; one made of fused silica<sup>7</sup> and the other made of N-BK7<sup>8</sup>. Assuming a pulse length of 30 fs and a flat intensity profile, the B integral (cf. section 2.1.4) value for the laser pulse passing through the two lenses reaches a value  $> 1$  at 90 mJ pulse energy, which was approximately the lowest energy at which full ionization was reliably observed. It increases up to  $\simeq 3$  for the maximum used energy of 189.9 mJ. This indicates that non-linear effects are likely to occur at all energies used in the experiments. At an energy of 48.8 mJ, the

<sup>6</sup>over the first 10 ns after creation

<sup>7</sup> $n_2(FS) = 3.2 \cdot 10^{-16} \text{ cm}^2/\text{W}$

<sup>8</sup> $n_2(BK7) = 3.4 \cdot 10^{-16} \text{ cm}^2/\text{W}$

## 5. Experimental Results

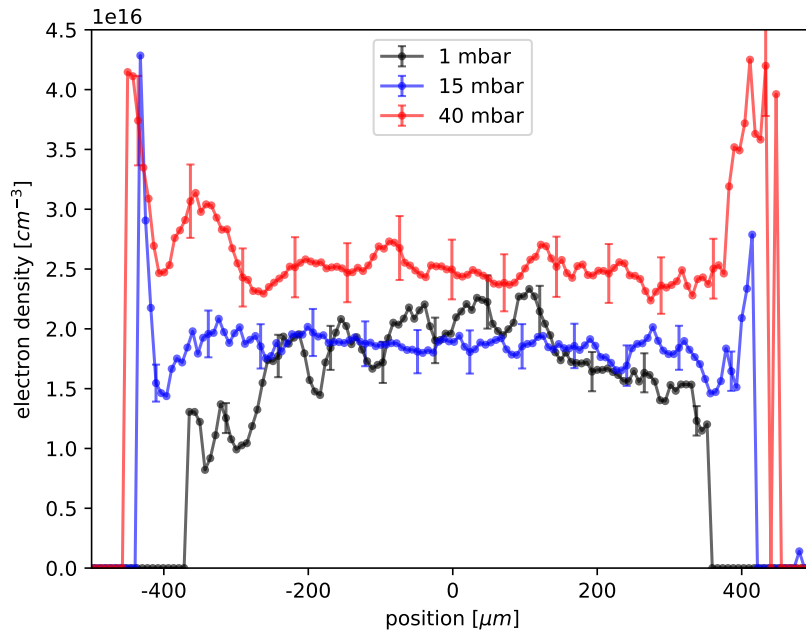


**Figure 5.22.:** Maximum transverse electron-density profiles for different hydrogen pressures at 94.8 mJ laser energy. The error bars, shown only on every tenth point for clarity, indicate the fluctuations and systematic error (see section 5.1).

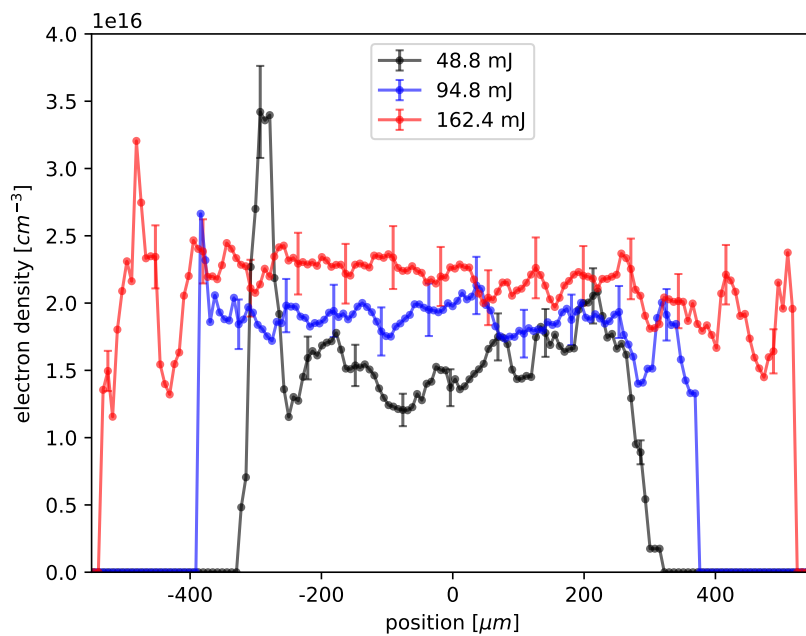


**Figure 5.23.:** Maximum transverse electron-density profiles for different laser energies at 10 mbar hydrogen pressure. The error bars, shown only on every tenth point for clarity, indicate the fluctuations and systematic error (see section 5.1).

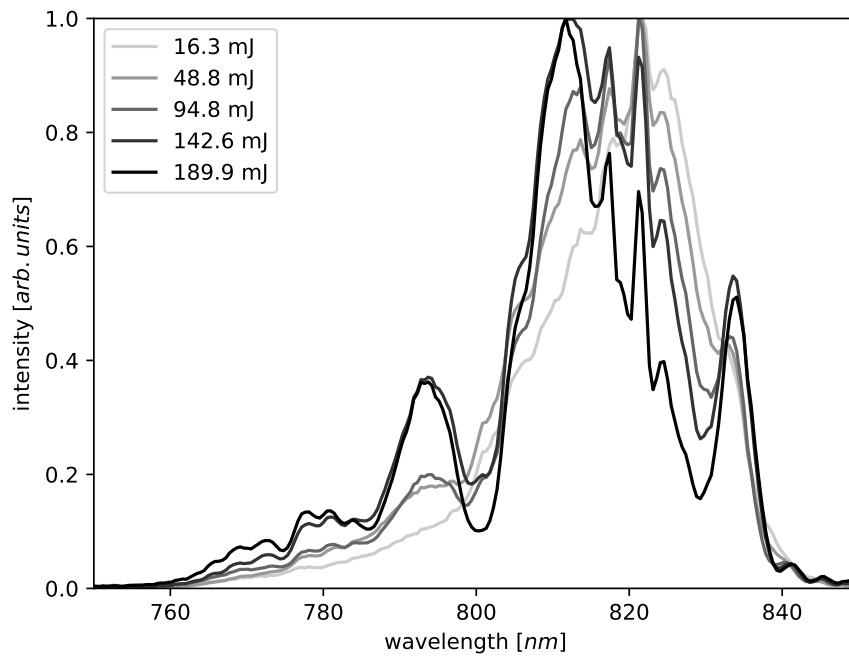


**Figure 5.24.:** Spectra of the laser pulse after passing through the focusing optics for different laser pulse energies averaged over 130 shots. The error bars are not shown for clarity. See figures 5.25, 5.26 and 5.27 for fluctuations.

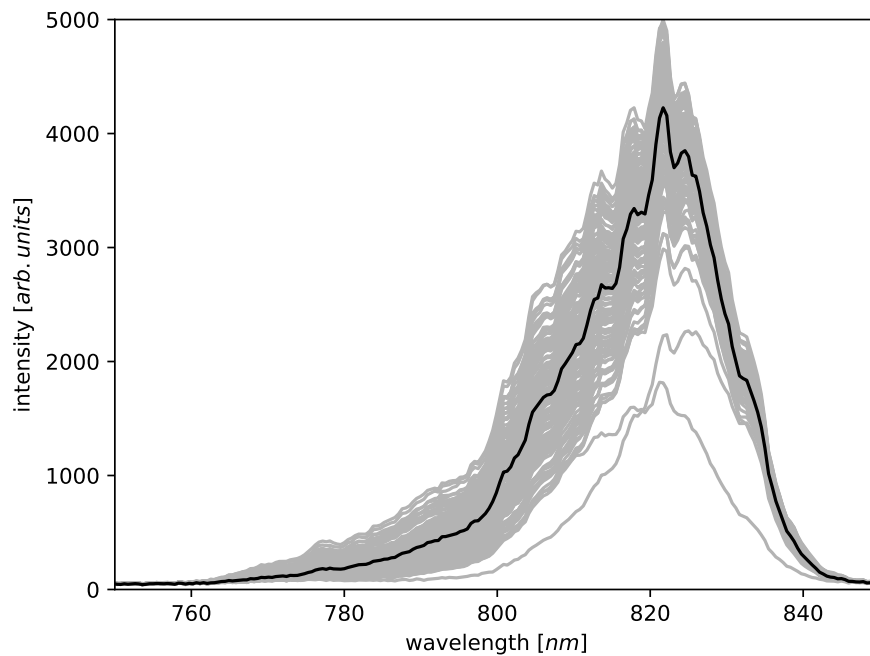


**Figure 5.25.:** All 130 measured spectra of the laser pulse at 16.3 mJ after passing through the focusing optics. Average plotted in black. The maximum standard deviation is 14%.

## 5. Experimental Results

---

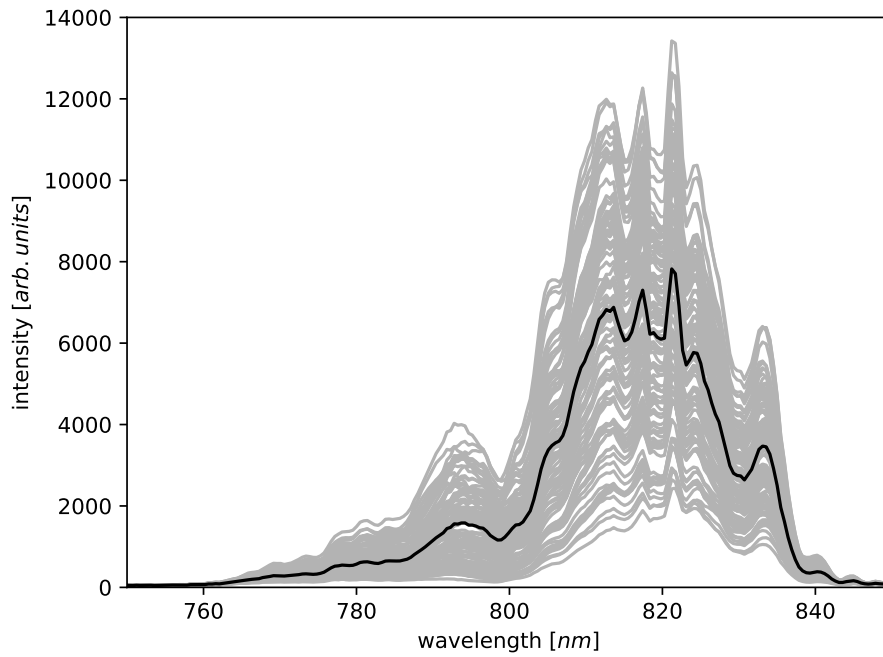


**Figure 5.26.:** All 130 measured spectra of the laser pulse at 94.8 mJ after passing through the focusing optics. Average plotted in black. The maximum standard deviation is 33%.

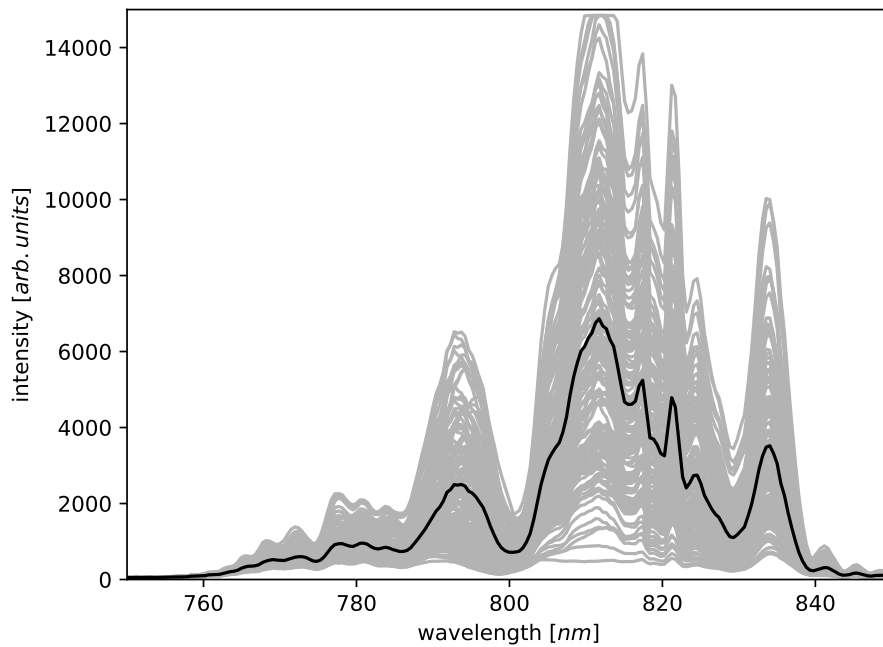


**Figure 5.27.:** All 130 measured spectra of the laser pulse at 189.9 mJ after passing through the focusing optics. Average plotted in black. The maximum standard deviation is 42%.

lowest at which ionization of the hydrogen gas could still be observed, the estimated B integral value is  $\simeq 0.73$ . This value is just about what is considered acceptable for the total B-integral of a focused short-pulse laser beam (cf. section 2.1.4 or Mourou and Umstadter (1992)), but in this setup the B integral stems from the lenses alone. Furthermore, this energy is too low to fully ionize the hydrogen inside the gas cell.

Along with the shift in the spectrum of the laser pulse, the pulse length increased by 30.2 fs ( $\pm 5.4$  fs) when the pulse energy was increased from 16.3 mJ to 189.9 mJ (after the lenses). This is almost a doubling of the unfocused pulse length at the ITC ( $\sim 40$  fs on average) which means that the peak intensity was only roughly half its expected value. Since the ionization capability of the laser depends on its intensity, this can be partially responsible for the lower than expected degree of ionization.

Besides the averaging caused by the 10 ns integration time, these non-linear effects can have a significant impact on the measured electron density. Therefore, more experiments are planned for the future to determine the influence and magnitude of each effect by, for example, using reflective focusing optics to avoid the nonlinear effects of transmissive optics. Furthermore, a more sensitive spectrometer and detector could enable an even higher temporal resolution than with the current setup by allowing shorter exposure times. This would allow for more detailed studies of the temporal evolution of the plasma density shortly after the arrival of the laser.

### 5.3.5. Conclusions

The measurements of the laser-induced plasmas showed that the average electron density as well as the transverse electron-density profile evolve rapidly during the first  $\sim 20$  ns after creation. This leads to an inaccurate measurement of the electron density, due to the long integration time of the spectrometer setup (10 ns) compared to the plasma evolution. At later times, the electron density decreases significantly slower, while the transverse electron-density profile stays approximately flat with outwards propagating shock fronts at the edges. Therefore, the electron-density measurements in the central region of the plasma at these times are accurate. Furthermore, the electron density at these late times is between  $10^{16} \text{ cm}^{-3}$  to  $10^{17} \text{ cm}^{-3}$ , independent of the backing pressure, while the plasma expands more rapidly at higher pressures, which leads to wider channels.

The average electron density in the regions of the plasma with high intensity emission and therefore the overall transverse density distribution is reproducible over several hundred shots and the results are realistic compared to the capillary-based measurements presented in this work and the observations from other sources (e.g Durfee III and Milchberg, 1993; Lemos *et al.*, 2013). Since the laser-based measurements presented

## 5. *Experimental Results*

---

in this chapter are all based on data taken during a single measuring campaign due to technical difficulties with the laser system and time constraints, these observations, especially regarding the fine structure of the density distribution such as the modulations observed in the transverse density profile, should be verified in the future.

The operating regime of FLASHForward will be  $10^{16} \text{ cm}^{-3}$  to  $10^{17} \text{ cm}^{-3}$ . Therefore, the results of this section show that it is beneficial to operate at later times after the plasma creation. This provides a temporally stable density distribution and the width of the plasma channel can be controlled via the backing pressure. The investigation of the non-linear effects in the focusing optics of the laser led to a change to reflective focusing optics in FLASHForward. Furthermore, these results show that nonlinear effects in the  $\sim 2 \text{ mm}$  thick window between the laser beamline and the electron beamline, which is required due to vacuum restrictions, will influence the performance of the laser regarding pulse length and spectrum in the planned experiments.

## Conclusions and Outlook

---

In order to generate stable and reproducible beams in plasma particle accelerators it is vital to gain knowledge of the initial plasma-density distribution and to be able to control it. This thesis investigated the possibility of using Stark-broadening of hydrogen lines as a means of measuring the plasma-density distribution. An imaging spectrometer in combination with an iCCD camera as detector allows line profiles of plasmas generated by a high-voltage discharge and a high-power laser to be investigated with  $\sim 10 \mu\text{m}$  spatial, 0.05 nm spectral, and down to 5 ns temporal resolution.

### Capillary Discharge Plasmas

Capillary discharge plasmas (see chapter 5.2), which are often used in LWFA due to their laser guiding properties, were used to determine the usability of the Stark-broadening method, since the spatial confinement of the plasma inside the capillary as well as the high stability of the discharge (see Goldberg, 2013) provided a well controlled test environment. With increasing hydrogen pressure, the measured spectral-line profiles showed the expected increase in intensity and line width as well as a shift of the line's central wavelength. These pressure-dependent measurements were used to compare the available methods for deriving the electron density from the line-width and -shift to the theoretical expectations. Thereby, it was determined that all proposed models are equivalent within error, with the model by Gigoso and Cardeñoso (1996) theoretically being the most accurate and the shift method being the most inaccurate. Furthermore, the measured spectra allowed for the identification of the capillary's sapphire material as a secondary plasma source, which before had only been suspected by Rowlands-Rees *et al.* (2008).

The time evolution and longitudinal distribution of the capillary-discharge plasmas have also been investigated at different pressures. The temporal evolution showed that, for backing pressures above 25 mbar, the density reaches its peak value shortly after the onset of the discharge and thereafter decreases due to thermal expansion. For pressures of 25 mbar and below, the electron density continually rises during the discharge, which can be attributed to the ablation of the sapphire. First direct measurements of the spatial electron-density distribution in the longitudinal direction showed the possibility of creating density ramps if a different pressure is applied to each inlet of the capillary. This also works if the gas applied to one of the inlets is helium. Therefore, a sufficiently

sensitive spectrometer setup would be able to measure the electron density of plasmas made of various gases and mixtures, as long as sufficient hydrogen is present. The properties of the spectral lines of other elements, which are similarly influenced by the electron density and might provide a stronger signal (e.g. Griem, Baranger, *et al.*, 1962; Dimitrijevic and Sahal-Br  chot, 1984), could also be used to determine the electron density of the plasma. However, to the authors knowledge, no established methods for this purpose exist for elements other than hydrogen.

### Laser-Induced Plasmas

The temporal evolution and transverse distribution of laser-induced plasmas, as will be used at FLASHForward, have also been investigated. Initial tests with CCD cameras just capturing the plasma emission at different positions around the focus showed that the current focusing setup is capable of creating a plasma with a length of  $\geq 50$  cm in  $\sim 10$  mbar of hydrogen. This is essential for the  $\sim 30$  cm-long gas targets planned for FLASHForward. It was also shown from just the plasma emission that the plasma lives for up to  $1 \mu\text{s}$ , depending on the pressure, limiting the possible repetition rate of acceleration to  $\sim 1$  MHz. The electron density decreases exponentially shortly after the creation of the plasma. This is due both to recombination, which takes place on a timescale of 10 ns to several hundred nanoseconds (e.g. Schwenke, 1990), and to the thermal expansion of the plasma (see e.g. Durfee III and Milchberg, 1993), which was also measured. The effects of this expansion were observed in the measured transverse density profiles. It was shown that the electron-density distribution initially has its maximum on the laser axis. The thermal expansion then forms a plasma channel with a density minimum on the laser axis. This effect is most obvious at low pressures of  $\sim 1$  mbar. Due to the faster expansion with increasing density and the limited temporal resolution of the spectrometer setup ( $\geq 5$  ns), the channel formation, which usually takes place within 0.5 ns to 2 ns for plasmas with densities on the order of  $10^{18} \text{ cm}^{-3}$  (see e.g. Lemos *et al.*, 2013), cannot be resolved at these high densities. Therefore, mostly flat density profiles with rising density at the edges were obtained at high hydrogen-gas densities. However, due to the slower density evolution at times  $> 40$  ns, the measurements at those times are accurate. Therefore, if this diagnostic setup is to be used in FLASHForward and the density has to be exactly known, it is favorable to let the plasma expand for  $\sim 40$  ns before introducing the electron bunch. Furthermore, with this method, the width of the plasma channel can be controlled via the backing pressure.

In all experiments with laser induced plasmas, the observed on-axis electron density never exceeded the  $10^{16} \text{ cm}^{-3}$  range, even for backing pressures as high as 80 mbar.

---

One cause for this is the rapid expansion of the plasma, as mentioned above. Further investigations uncovered that the transmissive focusing optics consisting of two lenses might also be partly responsible. Non-linear effects induced by the high-intensity laser pulse when passing through the lenses lead to a broadened laser spectrum with large intensity fluctuations that increase with increasing energy. Furthermore, the pulse length nearly doubles from the lowest to the highest laser-pulse energy used, leading to a lowered peak intensity. These effects are also responsible for the lower than expected on-axis densities that were measured.

## Comparison

Both types of plasma show their own unique features. Capillary-discharge plasmas can maintain a higher electron density over a longer period of time, due to the constant energy input during the discharge. Furthermore, the confines of the capillary keep the plasma from expanding in the transverse direction, which also alters the transverse electron-density evolution. Here, the plasma density increases towards the capillary walls due to the cooling of the plasma at the wall. In the case of the unconfined laser-induced plasma, the transverse electron density increases towards the edges due to an outwards-propagating shock front. Additionally, these plasmas expand rapidly due to the lack of confinement. Capillary-discharge plasmas allow for shaped longitudinal density profiles through the capillary design while laser-induced plasmas allow for transverse shaping of the density profile by altering the intensity distribution of the laser. Some of the advantages of both methods can be combined, for example by generating the plasma with a laser within a small, gas-filled channel. This would limit the expansion of the plasma and allow for longitudinal density shaping while maintaining the possibility of transverse density shaping.

## The Method

It was shown that the spectrometer setup enables the determination of electron densities with high relative accuracy. The validity of the established methods was confirmed and the model by Gigoso and Cardeñoso (1996) was chosen due to its theoretically higher accuracy in the case of plasma accelerators. However, a calibration with other methods of electron density measurement should be done in the future to determine the absolute accuracy of this method. The spectroscopic electron-density measurements proved to be well suited for the characterization of stable and well confined capillary-discharge plasmas and provided reasonable results for the electron densities. Furthermore, the

measured spectra allowed for the identification of the ablation of the capillary as a secondary plasma source. In the case of laser-induced plasmas, the spectroscopic measurements accumulate a higher error due to the fluctuations in the laser's pointing and energy. Furthermore, the fast evolution of these plasmas within the first  $\sim 2$  ns poses a challenge. The current setup is only capable of a temporal resolution of 5 ns and the low signal intensity of low pressure plasmas often requires an increased exposure time of at least 10 ns. However, if the plasma is allowed to expand and cool for  $\sim 40$  ns and the density is measured at times where the plasma distribution evolves slowly, the current setup is capable of delivering accurate density measurements for the laser-induced plasmas. A more sensitive detector, such as a streak camera or a line array camera, might provide a higher temporal resolution but would sacrifice the spatial imaging capability. This would have to be compensated for by scanning the plasma along the direction of interest.

## The Future

Future plans involve switching to reflective focusing optics to avoid nonlinear effects in the lenses, using a capillary-like gas target for the laser-induced plasmas to combine the transverse density-shaping capability of the laser-induced plasmas with the longitudinal density-tapering capability of discharge plasmas, and trying to increase the temporal resolution of the spectrometer setup to further investigate the lower than expected observed on-axis electron densities. Once this problem is resolved, a calibration of the Stark-broadening method, in particular the GC model, is planned by simultaneously measuring the electron density using the well understood interferometric method (see e.g. Gonsalves *et al.*, 2007; Jang, Kim, and Nam, 2012; Lemos *et al.*, 2013) and comparing the results. This will provide further insight into the validity and usability of the theoretical models behind the methods. Furthermore, experiments to tailor the transverse density profile by shaping the intensity distribution of the laser to enable guiding of the electrons via hollow-core plasma channels are planned as well as the implementation of Stark-broadening diagnostics at FLASHForward.

# Software

---

## A.1. Image Preparation Script

The images taken with the spectrometer had to be read in, saved, background subtracted, centered around a common axis and averaged in order to analyze them. Furthermore, the experimental parameters had to be extracted from the filenames. The following functions were used for this.

## A. Software

---

imagePreparator.py

```
1 import ToolBox as tb
2 import glob
3 import os
4 import shelve
5 import numpy as np
6 from PIL import Image
7
8
9 class imagePreparator:
10     def __init__(self):
11         self.imageLocation = '/run/media/lars/Data/ExpData/spectroscopy/20170323_dazzler_33050/Tiff'
12         self.fileExtension = '.tif'
13         self.fileList = ''
14         self.bgFileLocation = '/run/media/lars/Data/ExpData/spectroscopy/20170320_backgrounds_uncooled/Tiff'
15         self.bgIdentifier = ''
16         self.bgFileList = ''
17         self.imageStoreLocation = '/home/lars/ExpData/20170323_dazzler_33050'
18         self.maxCenFitError = 0.1 # max error in trying to find center of images
19
20     def getDirectories(self):
21         if self.imageLocation == '':
22             self.imageLocation = input('Enter location of images to prepare:\n')
23             while not os.path.exists(self.imageLocation):
24                 self.imageLocation = input('Image location does not exist. Please reenter:\n')
25             foo = input('Enter file extension of images to prepare (default .tif):\n')
26             if not foo == '':
27                 self.fileExtension = foo
28         if self.bgFileLocation == '':
29             self.bgFileLocation = input('Enter location of background images to use:\n')
30             while not os.path.exists(self.bgFileLocation):
31                 self.bgFileLocation = input('Background location does not exist. Please reenter:\n')
32             if self.bgFileLocation == self.imageLocation:
33                 self.bgIdentifier = input('Enter identifier for background images.\n')
34         self.fileList = self.getFileList(self.imageLocation)
35         self.bgFileList = self.getFileList(self.bgFileLocation)
36         if self.imageStoreLocation == '':
37             bar = input('Enter location to store prepared images. Default: ' + str(self.imageLocation) + '/PreparedImages\n')
38             if bar == '':
39                 self.imageStoreLocation = os.path.join(self.imageLocation, 'PreparedImages')
40             else:
41                 self.imageStoreLocation = bar
42         if not os.path.exists(self.imageStoreLocation):
43             print('Making storage directory ' + self.imageStoreLocation)
44             os.makedirs(self.imageStoreLocation)
45
46     def getFileList(self, fileLocation):
47         fileExtension = '*' + self.fileExtension
48         path = os.path.join(fileLocation, fileExtension)
49         return glob.glob(path)
50
51     def readImage(self, file):
52         im = Image.open(file)
53         imArr = np.array(im, dtype=np.float64)
54         im.close()
55         return imArr
56
57     def getAverageImage(self, images, keyprefix):
58         xshapes = [images[k]['image'].shape[0] for k in images]
59         s = np.zeros((min(xshapes), 1024), dtype=np.float64)
60         print('Shape of average image: ' + str(s.shape))
61         for key in images:
62             if keyprefix in key:
63                 im = images[key]['image']
64                 if s.shape[0] != im.shape[0]:
65                     im = np.resize(im, s.shape)
66                 s += im
67         s /= len(images)
68         std = np.zeros(s.shape, dtype=np.float64)
69         for key in images:
70             if keyprefix in key:
71                 im = images[key]['image']
72                 if s.shape[0] != im.shape[0]:
73                     im = np.resize(im, s.shape)
74                 std += (im - s) ** 2
75         std = np.sqrt(std / len(images))
76         return s, std, len(images)
77
78     def getBackground(self, id=''):
79         store = shelve.open(os.path.join(self.imageStoreLocation, 'backgrounds.db'))
80         raw = shelve.open(os.path.join(self.imageStoreLocation, 'raw_images.db'))
81         if self.bgFileList == '':
82             im = raw['image-1']['image']
83             store['average-bg'] = np.zeros(im.shape)
84             print('No backgrounds found. Setting background to 0.')
85             raw.close()
86             return
87         if not id=='':
88             bgfiles = [i for i in self.bgFileList if id in i]
89         else:
90             bgfiles = self.bgFileList
91         i = 0
92         l = len(bgfiles)
93         for item in bgfiles:
94             key = 'background-' + str(i)
95             im = self.readImage(item)
96             store[key] = {'image': im, 'attributes': 'None'}
97             i += 1
```

## A.1. Image Preparation Script

```
98         print('Background image ' + str(i) + ' of ' + str(l) + ' imported.')
99     print('Averaging...')
100     bg, bgstd, nimgs = self.getAverageImage(store, 'background-')
101     print('Averaged ' + str(nimgs) + ' images.')
102     store['average-bg'] = {'image': bg, 'attributes': {'stdErr': bgstd, 'noImgs': nimgs}}
103     store.close()
104     raw.close()
105     print('Successfully acquired background.')
106
107     def subtractBackground(self):
108         raw = shelve.open(os.path.join(self.imageStoreLocation, 'raw_images.db'))
109         bgs = shelve.open(os.path.join(self.imageStoreLocation, 'backgrounds.db'))
110         clean = shelve.open(os.path.join(self.imageStoreLocation, 'bg_subtracted.db'))
111         i = 0
112         for key in raw:
113             print('Cleaning ' + key + '...')
114             bg = bgs['average-bg']['image']
115             im = raw[key]['image']
116             i += 1
117             if im.shape != bg.shape:
118                 oldshape = bg.shape
119                 bg = np.resize(bg, im.shape)
120                 print('Resized background with ' + str(oldshape)
121                       + ' to ' + str(bg.shape) + ' to fit image no. ' + str(i))
122             cl = im - bg
123             clean[key] = {'image': cl, 'attributes': raw[key]['attributes']}
124             print('Image no. ' + str(i) + ' background subtracted.')
125         raw.close()
126         bgs.close()
127         clean.close()
128         print('Successfully subtracted background from ' + str(i) + ' images.')
129
130     def getIntensity(self, image):
131         return np.sum(image)
132
133     def loadImages(self):
134         store = shelve.open(os.path.join(self.imageStoreLocation, 'raw_images.db'))
135         i = 0
136         l = len(self.fileList)
137         for item in self.fileList:
138             im = self.readImage(item)
139             att = tb.parseFileName(item)
140             key = 'image-' + str(i)
141             store[key] = {'image': im, 'attributes': att}
142             i += 1
143             print('Image ' + str(i) + ' of ' + str(l) + ' imported.')
144         store.close()
145         print('Successfully imported all ' + str(l) + ' images.')
146
147     def findPlasmaCenters(self):
148         clean = shelve.open(os.path.join(self.imageStoreLocation, 'bg_subtracted.db'))
149         newc = shelve.open(os.path.join(self.imageStoreLocation, 'bg_subtracted_c.db'))
150         # fit Gaussian to horizontally binned data to determine center and sigma values
151         for key in clean:
152             binIm = np.sum(clean[key]['image'], axis=1)
153             xdata = np.arange(len(binIm))
154             bestFit, fitParams = tb.fitGaussian(xdata, binIm)
155             im = clean[key]['image']
156             att = clean[key]['attributes']
157             fit = {'amplitude': fitParams['amplitude'].value, 'ampErr': fitParams['amplitude'].stderr,
158                  'VCenter': fitParams['center'].value, 'VCenErr': fitParams['center'].stderr,
159                  'VSigma': fitParams['sigma'].value, 'VSigErr': fitParams['sigma'].stderr}
160             newc[key] = {'image': im, 'attributes': att, 'centerfit': fit}
161             print('Center for ' + key + ' found at ' + str(fitParams['center'].value) + ' +/- ' + str(
162                   fitParams['center'].stderr))
163         # select maximum sigma value for cropping / padding
164         clean.close()
165         newc.close()
166         os.remove(os.path.join(self.imageStoreLocation, 'bg_subtracted.db'))
167
168     def getSigma(self, data):
169         sigmas656 = []
170         sigmas486 = []
171         sigmas434 = []
172         for key in data:
173             relSigErr = data[key]['centerfit']['VSigErr'] / data[key]['centerfit']['VSigma']
174             if relSigErr < self.maxCenFitError:
175                 if data[key]['attributes']['wavelength'] == '656nm':
176                     sigmas656.append(data[key]['centerfit']['VSigma'])
177                 elif data[key]['attributes']['wavelength'] == '486nm':
178                     sigmas486.append(data[key]['centerfit']['VSigma'])
179                 elif data[key]['attributes']['wavelength'] == '434nm':
180                     sigmas434.append(data[key]['centerfit']['VSigma'])
181             sigma656 = np.sum(sigmas656) / len(sigmas656)
182             sigma486 = np.sum(sigmas486) / len(sigmas486)
183             sigma434 = np.sum(sigmas434) / len(sigmas434)
184             return sigma656, sigma486, sigma434
185
186     def centerImages(self, sig=3):
187         clean = shelve.open(os.path.join(self.imageStoreLocation, 'bg_subtracted_c.db'))
188         centered = shelve.open(os.path.join(self.imageStoreLocation, 'centered.db'))
189         discarded = shelve.open(os.path.join(self.imageStoreLocation, 'discarded_centered.db'))
190         maxSigma656, maxSigma486, maxSigma434 = self.getSigma(clean)
191         print('Sigma values for centering: ' + str(maxSigma656) + ' at 656nm, ' + str(maxSigma486) + ' at 486nm, and '
192               + str(maxSigma434) + ' at 434nm.')
193         i = 0
194         l = len(clean)
195         for key in clean:
196             print('Trying to center ' + key)
197             # determine if fit was ok and that image can be centered
```

## A. Software

---

```
198     im = clean[key]['image']
199     att = clean[key]['attributes']
200     cen = clean[key]['centerfit']
201     if att['wavelength'] == '656nm':
202         maxSigma = maxSigma656
203     elif att['wavelength'] == '486nm':
204         maxSigma = maxSigma486
205     elif att['wavelength'] == '434nm':
206         maxSigma = maxSigma434
207     relSigErr = cen['VsigErr']/cen['Vsigma']
208     relCenErr = cen['VCenErr']/cen['VCenter']
209     if relCenErr > self.maxCenFitError or relSigErr > self.maxCenFitError:
210         discarded[key] = {'image': im, 'attributes': att, 'centerfit': cen}
211         i += 1
212         print('Image ' + str(i) + ' of ' + str(l) + ' discarded from centering with '
213               + str(relSigErr) + ' sigma error and ' + str(relCenErr) + ' center error.')
214         continue
215     i += 1
216     print('Image ' + str(i) + ' of ' + str(l) + ' can be centered with '
217           + str(relSigErr) + ' sigma error and ' + str(relCenErr) + ' center error.')
218     # determine pad / crop parameters for top of image
219     topDiff = cen['VCenter'] - sig * maxSigma
220     if topDiff < 0:
221         topPad = int(abs(topDiff))
222     else:
223         topPad = 0
224     if topDiff > 0:
225         topCrop = int(abs(topDiff))
226     else:
227         topCrop = 0
228     print('Top of image will be cropped by ' + str(topCrop) + ' and padded by ' + str(topPad))
229     botDiff = (cen['VCenter'] + sig * maxSigma) - im.shape[0]
230     # determine pad / crop parameters for bottom of image
231     if botDiff > 0:
232         botPad = int(abs(botDiff))
233     else:
234         botPad = 0
235     if botDiff < 0:
236         botCrop = int(abs(botDiff))
237     else:
238         botCrop = 0
239     print('Bottom of image will be cropped by ' + str(botCrop) + ' and padded by ' + str(botPad))
240     # now for the actual cropping
241     botEnd = im.shape[0] - botCrop
242     im = im[topCrop:botEnd]
243     # and padding
244     im = np.pad(im, ((topPad, botPad), (0, 0)), 'constant', constant_values=0)
245     # now store the whole thing
246     centered[key] = {'image': im, 'attributes': att, 'centerfit': cen}
247     print('Image ' + str(i) + ' of ' + str(l) + ' centered. New shape: ' + str(im.shape))
248     clean.close()
249     centered.close()
250     discarded.close()
251
252     def averageImages(self, data='centered.db'):
253         centered = shelve.open(os.path.join(self.imageStoreLocation, data))
254         averaged = shelve.open(os.path.join(self.imageStoreLocation, 'averaged.db'))
255         uniqueAttributes = self.getListOfUniqueAttributeCombinations(centered)
256         i = 0
257         l = len(uniqueAttributes)
258         print(str(l) + ' sets of unique attribute combinations found')
259         for attributes in uniqueAttributes:
260             print('Averaging images with ' + str(attributes))
261             ims = self.getImagesByAttributes(attributes, centered)
262             avImg, stdErr, noImg = self.getAverageImage(ims, 'match-')
263             avg = {'error': stdErr, 'imagecount': noImg}
264             key = 'averaged-' + str(i)
265             averaged[key] = {'image': avImg, 'attributes': attributes, 'average': avg}
266             i += 1
267             print('Imageset ' + str(i) + ' of ' + str(l) + ' with ' + str(noImg) + ' images averaged.')
268         centered.close()
269         averaged.close()
270
271     def averageImagesByPressure(self, pressure, tolerance=1., data='centered.db'):
272         centered = shelve.open(os.path.join(self.imageStoreLocation, data))
273         averaged = shelve.open(os.path.join(self.imageStoreLocation, 'averaged_by_pressure.db'))
274         uniqueAttributes = self.getListOfUniqueAttributeCombinationsForPressure(centered, pressure, tolerance)
275         print(str(len(uniqueAttributes)) + ' sets of unique attribute combinations at ' + str(pressure) + ' mbar found.')
276         i = 0
277         for attributes in uniqueAttributes:
278             print('Averaging images with ' + str(attributes))
279             ims = self.getImagesByAttributes(attributes, centered, pressure, tolerance)
280             pressures = []
281             amps = []
282             amperrors = []
283             vcenters = []
284             vcerrors = []
285             vsigmas = []
286             vsigerros = []
287             for g in ims:
288                 pressures.append(float(ims[g]['attributes']['pressure'][: -4]))
289                 amps.append(ims[g]['centerfit']['amplitude'])
290                 amperrors.append(ims[g]['centerfit']['ampErr'])
291                 vcenters.append(ims[g]['centerfit']['VCenter'])
292                 vcerrors.append(ims[g]['centerfit']['VCenErr'])
293                 vsigmas.append(ims[g]['centerfit']['Vsigma'])
294                 vsigerros.append(ims[g]['centerfit']['VsigErr'])
295             avgpressure = np.sum(pressures) / len(pressures)
296             avgamp = np.sum(amps) / len(amps)
297             avgcen = np.sum(vcenters) / len(vcenters)
```

## A.1. Image Preparation Script

```
298     avgsig = np.sum(vsigmas) / len(vsigmas)
299     presserror = 0
300     for item in pressures:
301         presserror += (item - avgpressure) ** 2
302     presserror = np.sqrt(presserror / len(pressures))
303     amperror = np.sum(amperrors) / len(amperrors)
304     cenerror = np.sum(vcenerrors) / len(vcenerrors)
305     sigerror = np.sum(vsigerrors) / len(vsigerrors)
306     attributes['pressure'] = str(avgpressure) + 'mbar'
307     attributes['presserror'] = str(presserror) + 'mbar'
308     avImg, stdErr, noImg = self.getAverageImage(ims, 'match-')
309     avg = {'error': stdErr, 'imagecount': noImg}
310     cen = {'amplitude': avgamp, 'ampErr': amperror, 'VCenter': avgcen, 'VCenErr': cenerror,
311           'VSigma': avgsig, 'VSigErr': sigerror}
312     i += 1
313     key = str(pressure) + 'mbar-' + str(i)
314     averaged[key] = {'image': avImg, 'attributes': attributes, 'average': avg, 'centerfit': cen}
315     print('Averaged ' + str(noImg) + ' images at ' + str(avgpressure) + ' +/- ' + str(presserror))
316     centered.close()
317     averaged.close()
318     print('Finished!')
319
320 def getListOfUniqueAttributeCombinations(self, data):
321     fileAttributes = [data[key]['attributes'] for key in data]
322     uniqueAttributes = [dict(t) for t in set([tuple(sorted(d.items())) for d in fileAttributes])]
323     return uniqueAttributes
324
325 def getListOfUniqueAttributeCombinationsForPressure(self, data, pressure, tolerance):
326     minp = pressure - tolerance
327     maxp = pressure + tolerance
328     fileAttributes = [data[key]['attributes'] for key in data
329                       if minp < float(data[key]['attributes']['pressure'][:-4]) <= maxp]
330     for item in fileAttributes:
331         item.pop('pressure')
332     uniqueAttributes = [dict(t) for t in set([tuple(sorted(d.items())) for d in fileAttributes])]
333     return uniqueAttributes
334
335 def getImagesByAttributes(self, attributes, data, pressure=-1., tolerance=1.):
336     matches = {}
337     i = 0
338     minp = pressure - tolerance
339     maxp = pressure + tolerance
340     for key1 in data:
341         match = True
342         if pressure != -1. and not minp < float(data[key1]['attributes']['pressure'][:-4]) <= maxp:
343             match = False
344         else:
345             for key2 in attributes:
346                 if data[key1]['attributes'][key2] != attributes[key2]:
347                     match = False
348                     break
349             else:
350                 continue
351         if match == True:
352             i += 1
353             s = 'match-' + str(i)
354             matches[s] = data[key1]
355     return matches
356
357
358 def prepareImages():
359     ip = imagePreparator()
360     ip.getDirectories()
361     ip.loadImages()
362     ip.getBackground()
363     ip.subtractBackground()
364     ip.centerImages()
365     ip.averageImages()
366
367 # if __name__ == '__main__':
368 #     prepareImages()
369
```

## **A.2. Image Analysis Script**

The spectrometer images were analyzed by fitting a Lorentzian to the spectral profile in order to extract the FWHM or FWHA and then converting it to an electron density.

## A.2. Image Analysis Script

```

imageAnalyser.py

1 import numpy as np
2 import os
3 import shelve
4 import ToolBox as tb
5
6 class imageAnalyser:
7     def __init__(self):
8         self.imageLocation = '/home/lars/ExpData/Analysis/Calibration'
9         self.resultStoreLocation = '/home/lars/ExpData/Analysis/Calibration'
10        self.specRange = 51.01 #wavelength range covered by one image
11        self.errorTolerance = 0.1 # tolerance for fit errors
12
13    def convertPixelsToWavelength(self, wl):
14        xdata = np.arange(wl - self.specRange / 2, wl + 513 * self.specRange / 1024, self.specRange / 1024)
15        return xdata
16
17    # convert fwhm to density. Result in cm-3
18    def fwhmToNe(self, data, errors):
19        data = np.asarray(data)
20        errors = np.asarray(errors)
21        relErrors = errors / data
22        newRelErrors = (3/2) * relErrors
23        alpha = 0.00226 #-konstante in nm, aus H. Griem
24        data = 8.02e12 * (data / alpha) ** (3 / 2)
25        return data, data * newRelErrors
26
27    # alternate conversion, depending on FWHArea. Not so much dependent on Ne and T. Result in cm-3
28    # Functions from Gigosos et al. 2003
29    def widthToNeGigosos(self, data, errors, line='alpha'):
30        pars = {'alpha': (0.549, 1/0.67965), 'beta': (1.666, 1/0.68777), 'gamma': (2.433, 1/0.68575)}
31        c, exp = pars[line]
32        data = np.asarray(data)
33        errors = np.asarray(errors)
34        relErrors = errors / data
35        newRelErrors = exp * relErrors
36        data = (10**17) * (data/c)**exp
37        return data, data * newRelErrors
38
39    def calculateShift(self, center, errors, line='alpha'):
40        lineValue = {'alpha': 656.279, 'beta': 486.135, 'gamma': 434.0472, 'delta': 410.1734}
41        shift = center - lineValue[line]
42        return shift, errors
43
44    # convert shift to density
45    def shiftToNe(self, shift, errors):
46        d0 = 4.963065e-20 # 0.29e-18 #constant from J. Callaway, K. Unnikrishnan, converted to nm
47        errors = errors / d0
48        return shift / d0, errors
49
50    # calculation of the matched spot size(1 / e ^ 2 radius) in micron
51    def calcMatchedSpotSize(self, capRad, ne, neErr):
52        wm = 1.48e5 * np.sqrt(capRad / np.sqrt(ne))
53        wmErr = neErr * 0.25
54        return wm, wmErr
55
56    def analyseImage(self, data='averaged_by_pressure.db'):
57        store = shelve.open(os.path.join(self.imageLocation, data))
58        analysed656 = shelve.open(os.path.join(self.resultStoreLocation, 'analysed_656nm.db'))
59        discarded656 = shelve.open(os.path.join(self.resultStoreLocation, 'discarded_analysed_656nm.db'))
60        i = 0
61        l = len(store)
62        for key in store:
63            i += 1
64            if store[key]['attributes']['wavelength'] == '656nm':
65                binnedImage = np.sum(store[key]['image'], axis=0)
66                wlNum = float(store[key]['attributes']['wavelength'][:-2])
67                xdata = self.convertPixelsToWavelength(wlNum)
68                xdata = np.resize(xdata, binnedImage.shape)
69                bfit, bpar = tb.fitLorentzian(xdata, binnedImage, wlNum, True)
70                amperr = abs(bpar['amplitude'].stderr / bpar['amplitude'].value) # calc rel errors for fit check
71                cenerr = abs(bpar['center'].stderr / bpar['center'].value)
72                fwhmerr = abs(bpar['fwhm'].stderr / bpar['fwhm'].value)
73                sigerr = abs(bpar['sigma'].stderr / bpar['sigma'].value)
74                fit = {'amplitude': bpar['amplitude'].value, 'ampErr': bpar['amplitude'].stderr,
75                    'center': bpar['center'].value, 'cenErr': bpar['center'].stderr,
76                    'fwhm': bpar['fwhm'].value, 'fwhmErr': bpar['fwhm'].stderr,
77                    'sigma': bpar['sigma'].value, 'sigmaErr': bpar['sigma'].stderr}
78                ana = {'bestFit': bfit, 'fitParameters': fit}
79                print('Image ' + str(i) + ' of ' + str(l) + ' at 656nm analysed...')
80                k = 'analysed-' + str(i)
81                if amperr <= self.errorTolerance and cenerr <= self.errorTolerance and fwhmerr <= self.errorTolerance \
82                   and sigerr <= self.errorTolerance:
83                    analysed656[k] = {'image': store[key]['image'], 'attributes': store[key]['attributes'],
84                                     'average': store[key]['average'], 'analysis': ana}
85                    print('... and stored.')
86                else:
87                    discarded656[k] = {'image': store[key]['image'], 'attributes': store[key]['attributes'],
88                                     'analysis': ana}
89                    print('... and discarded.')
90        store.close()
91        analysed656.close()
92        discarded656.close()
93        print('Finished!')
94
95    def spatiallyAnalyseImage(self, data='averaged_by_pressure.db'):

```

## A. Software

---

```
96 store = shelve.open(os.path.join(self.imageLocation, data))
97 analysed656 = shelve.open(os.path.join(self.resultStoreLocation, 'analysed_spatially_656nm.db'))
98 i = 0
99 l = len(store)
100 for key in store:
101     i += 1
102     if store[key]['attributes']['wavelength'] == '656nm':
103         print('Analysing image ' + str(i) + ' of ' + str(l) + ' at 656nm.')
104         lineBestFits = []
105         lineFitResults = []
106         discardedLineBestFits = []
107         discardedLineFitResults = []
108         pic = store[key]['image']
109         wLNum = float(store[key]['attributes']['wavelength'][:-2])
110         xdata = self.convertPixelsToWavelength(wLNum)
111         xdata = np.resize(xdata, pic.shape[1])
112         j = 0
113         m = pic.shape[0]
114         for line in pic:
115             j += 1
116             print('Fitting line ' + str(j) + ' of ' + str(m) + '...')
117             bfit, bpar = tb.fitLorentzian(xdata, line, wLNum)
118             amperr = abs(bpar['amplitude'].stderr / bpar['amplitude'].value) # calc rel errors for fit check
119             cenerr = abs(bpar['center'].stderr / bpar['center'].value)
120             fwhmerr = abs(bpar['fwhm'].stderr / bpar['fwhm'].value)
121             sigerr = abs(bpar['sigma'].stderr / bpar['sigma'].value)
122             fitParameters = {'amplitude': bpar['amplitude'].value, 'ampErr': bpar['amplitude'].stderr,
123                             'center': bpar['center'].value, 'cenErr': bpar['center'].stderr,
124                             'fwhm': bpar['fwhm'].value, 'fwhmErr': bpar['fwhm'].stderr,
125                             'sigma': bpar['sigma'].value, 'sigmaErr': bpar['sigma'].stderr}
126             if amperr <= self.errorTolerance and cenerr <= self.errorTolerance and fwhmerr <= self.errorTolerance \
127                 and sigerr <= self.errorTolerance:
128                 print('... and storing it.')
129                 lineBestFits.append(bfit)
130                 lineFitResults.append(fitParameters)
131             else:
132                 print('... and discarding it.')
133                 lineBestFits.append(np.zeros(xdata.shape))
134                 lineFitResults.append({'amplitude': 0, 'ampErr': 0,
135                                     'center': 0, 'cenErr': 0,
136                                     'fwhm': 0, 'fwhmErr': 0,
137                                     'sigma': 0, 'sigmaErr': 0})
138                 discardedLineBestFits.append(bfit)
139                 discardedLineFitResults.append(fitParameters)
140             k = 'analysed-' + str(i)
141             ana = {'bestLineFits': lineBestFits, 'lineFitParameters': lineFitResults,
142                  'discardedLineFits': discardedLineBestFits, 'discardedLineFitParameters': discardedLineFitResults}
143             analysed656[k] = {'image': store[key]['image'], 'attributes': store[key]['attributes'],
144                              'average': store[key]['average'], 'analysis': ana}
145 store.close()
146 analysed656.close()
147 print('Finished!')
148
```

### **A.3. ToolBox**

The tool box contains several functions for fitting, parsing, averaging and integrating that were used in the analysis of the images.

## A. Software

---

### ToolBox.py

```
1 import numpy as np
2 import re
3 from natsort import natsorted
4 from lmfit.models import GaussianModel
5 from lmfit.models import LorentzianModel
6 from lmfit.models import VoigtModel
7 from lmfit.models import LinearModel
8 from scipy.integrate import quad
9 from scipy.integrate import simpson
10 from scipy.optimize import fsolve
11
12
13 def parseFileName(filename):
14     wavelength = re.search(r'\d{1,4}nm', filename)
15     pressure = re.search(r'\d{1,3}\.\d{1,2}mbar', filename)
16     delay = re.search(r'\d{1,2}\.\d{1,9}s_', filename)
17     if delay == None:
18         delay = re.search(r'\d{1,2}\.\d{1,4}e-\d{1,2}s_', filename)
19     lensPos = re.search(r'_\d{1,6}lens_', filename)
20     attPerc = re.search(r'\d{1,3}\.\d{1}att_', filename)
21     parameters = {'wavelength': wavelength.group()[1:-1], "delay": delay.group()[1:-1], "pressure": pressure.group()[1:-1],
22                 "lensPos": lensPos.group()[1:-1], "attPerc": attPerc.group()[1:-1]}
23     return parameters
24
25
26 def getParameterList(fileList):
27     wavelengths = []
28     pressures = []
29     delays = []
30     lensPos = []
31     attPerc = []
32     for item in fileList:
33         params = parseFileName(item)
34         wavelengths.append(params['wavelength'])
35         pressures.append(params['pressure'])
36         delays.append(params['delay'])
37         lensPos.append(params['lensPos'])
38         attPerc.append(params['attPerc'])
39     paramList = {"wavelengths": natsorted(set(wavelengths)), "delays": natsorted(set(delays)), "pressures": natsorted(set(pressures))}
40     return paramList
41
42
43 def fitGaussian(xdata, ydata):
44     peak = GaussianModel()
45     pars = peak.guess(ydata, x=xdata)
46     out = peak.fit(ydata, pars, x=xdata)
47     print(out.fit_report())
48     return out.best_fit, out.params
49
50
51 def fitLorentzian(xdata, ydata, cen, background=False):
52     peak = LorentzianModel()
53     pars = peak.guess(ydata, x=xdata)
54     pars['center'].set(cen, min=cen - 2, max=cen + 2) # make sure center of fit stays at target wavelength
55     # pars['gamma'].set(value=1., vary=True, expr='') #only for VoigtModel()
56     if background:
57         backgr = LinearModel()
58         pars += backgr.make_params(slope=0, intercept=np.amin(ydata))
59         mod = peak + backgr
60     else:
61         mod = peak
62     out = mod.fit(ydata, pars, x=xdata)
63     print(out.fit_report())
64     return out.best_fit, out.params
65
66
67 def fitVoigt(xdata, ydata, cen):
68     peak = VoigtModel()
69     backgr = LinearModel()
70     pars = peak.guess(ydata, x=xdata)
71     pars['center'].set(cen, min=cen - 2, max=cen + 2) # make sure center of fit stays at target wavelength
72     pars['gamma'].set(value=1., vary=True, expr='')
73     pars += backgr.make_params(slope=0, intercept=np.amin(ydata))
74     mod = peak + backgr
75     out = mod.fit(ydata, pars, x=xdata)
76     print(out.fit_report())
77     return out.best_fit, out.params
78
79
80 def runningaverage(data, width=3):
81     steps = (width - 1)/2
82     for i in np.arange(steps, len(data)):
83         data[i] = (data[i - steps] + data[i + steps]) / width
84     return data
85
86
87 def running_mean(x, N):
88     cumsum = np.cumsum(np.insert(x, 0, 0))
89     return (cumsum[N:] - cumsum[:-N]) / N
90
91
92 def deltaOmega(parameters, guess1, guess2):
93     amp = parameters['amplitude']
94     cen = parameters['center']
95     gamma = parameters['fwhm'] / 2
96     def lorentzian(x):
97         return amp / (1 + ((x - cen) / gamma) ** 2)
98     integral2, err2 = quad(lorentzian, -np.inf, np.inf)
99     def func1(x):
100         integral1, err1 = quad(lorentzian, -np.inf, x)
101         return (1 / 4) * integral2 - (integral1 / integral2)
102     def func2(x):
103         integral1, err1 = quad(lorentzian, -np.inf, x)
```

```

102         return (3 / 4) * integral2 - (integral1 / integral2)
103     vomega1 = np.vectorize(func1)
104     vomega2 = np.vectorize(func2)
105     fom1, = fsolve(vomega1, guess1)
106     fom2, = fsolve(vomega2, guess2)
107     return fom2 - fom1
108
109 def getGuesses(parameters):
110     guess1 = parameters['center'] - (parameters['fwhm'] / 2)
111     guess2 = parameters['center'] + (parameters['fwhm'] / 2)
112     return guess1, guess2
113
114 def convertPixelsToWavelength(wl):
115     xdata = np.arange(wl - 51.01 / 2, wl + 513 * 51.01 / 1024, 51.01 / 1024)
116     return xdata
117
118 def fitbaseline(data, avgint=50):
119     yavg1 = np.sum(data[0:avgint]) / avgint
120     yavg2 = np.sum(data[len(data)-avgint:]) / avgint
121     m = (yavg2 - yavg1) / ((len(data) - avgint/2) - (avgint/2))
122     b = ((yavg1 - m * avgint/2) + (yavg2 - m * (len(data) - avgint/2))) / 2
123     return m, b
124
125 def deltaOmegaNum(data, wavelength, bm, bb):
126     wave = convertPixelsToWavelength(wavelength)
127     blArea, blErr = quad(lambda x: bm * x + bb, wave[463], wave[563])
128     peakArea = simpson(data[463:563], wave[463:563])
129     area = peakArea - blArea
130     w1 = area / 4
131     w2 = 3*area / 4
132     dw1 = 0
133     dw2 = 0
134     for i in range(470, 563):
135         base, err = quad(lambda x: bm * x + bb, wave[463], wave[i])
136         peak = simpson(data[463:i], wave[463:i])
137         print(str((peak - base) / area) + ' of whole area reached.')
138         if peak - base >= w1 and dw1 == 0:
139             dw1 = wave[i]
140             print('First limit at ' + str(dw1))
141         if peak - base >= w2:
142             dw2 = wave[i]
143             print('Second limit at ' + str(dw2))
144             break
145     return dw2 - dw1
146

```



# Bibliography

---

- Ali, A. W. and H. R. Griem, *Theory of resonance broadening of spectral lines by atom-atom impacts*. Physical Review **140**, (1965)
- Altarelli, M., *The European X-ray free-electron laser facility in Hamburg*. Nuclear Instruments and Methods in Physics Research, Section B: Beam Interactions with Materials and Atoms **269**, 2845–2849 (2011)
- Ammosov, M.V., N.B. Delone, and V.P. Krainov, *Tunnel ionization of complex atoms and of atomic ions in an alternating electromagnetic field*. Sov. Phys. JETP **64**, 4–7 (1986)
- Aschikhin, A. *et al.*, *The FLASHForward facility at DESY*. Nuclear Instruments and Methods in Physics Research, Section A: Accelerators, Spectrometers, Detectors and Associated Equipment **806**, 175–183 (2016)
- Ashkenazy, J., R. Kipper, and M. Caner, *Spectroscopic measurements of electron density of capillary plasma based on Stark broadening of hydrogen lines*. Physical Review A **43**, 5568–5574 (1991)
- Augst, S. *et al.*, *Laser ionization of noble gases by Coulomb-barrier suppression*. JOSA B **8**, 858 (1991)
- Auguste, T. *et al.*, *Defocusing effects of a picosecond terawatt laser pulse in an underdense plasma*. Optics Communications **89**, 145–148 (1992)
- Bethe, H.A. and E.E. Salpeter, *Quantum Mechanics of One- and Two-Electron Atoms*, Springer Verlag (1957)
- Bohm, D. and E. P. Gross, *Theory of Plasma Oscillations. A. Origin of Medium-Like Behavior*. Physical Review **75**, 1851–1864 (1949)
- Bourgeois, N., J. Cowley, and S. M. Hooker, *Two-pulse ionization injection into quasilinear laser wakefields*. Physical Review Letters **111**, 1–5 (2013)
- Bulanov, S. *et al.*, *Particle injection into the wave acceleration phase due to nonlinear wake wave breaking*. Physical Review E **58**, R5257–R5260 (1998)
- Cairns, R. A., *Plasma Physics*, Blackie (1985)
- Callaway, J. and K. Unnikrishnan, *Shift and width of the Balmer- $\alpha$  and Lyman- $\beta$  lines of neutral hydrogen due to electron collisions*. Physical Review A **44**, 3001–3006 (1991)
- Chen, Pisin *et al.*, *Acceleration of Electrons by the Interaction of a Bunched Electron Beam with a Plasma*. Physical Review Letters **54**, 693–696 (1985)
- Cooper, J., *Plasma spectroscopy*. Reports on Progress in Physics **29**, 302 (1966)
- Delone, N.B. and V.P. Krainov, *Tunneling and barrier-suppression ionization of atoms and ions in a laser radiation field*. Physics-Uspekhi **41**, 469–485 (1998)
- Demtröder, Wolfgang, *Experimentalphysik 2: Elektrizität und Optik, Fünfte*, Springer-Verlag (2009)
- Dimitrijevic, M.S. and S. Sahal-Bréchet, *Stark broadening of neutral helium lines*. Journal of Quantitative Spectroscopy and Radiative Transfer **31**, 301–313 (1984)
- Dinklage, A. *et al.*, *Plasma Physics*, Springer-Verlag (2005), ISBN: 3-540-25274-6
- Dorchies, F. *et al.*, *Monomode Guiding of  $10^{16}$  W/cm<sup>2</sup> Laser Pulses over 100 Rayleigh Lengths in Hollow Capillary Dielectric Tubes*. Physical Review Letters **82**, 4655–4658 (1999)

- Durfee III, C. G. and H. M. Milchberg, *Light Pipe for High Intensity Laser Pulses*. Ebeling, Bernd, *European XFEL*, 2017
- Einstein, Albert, *Über einen die Erzeugung und Verwandlung des Lichtes betreffenden heuristischen Gesichtspunkt*. *Annalen der Physik* **322**, 132–148 (1905)
- Einstein, Albert, *Über das Relativitätsprinzip und die aus demselben gezogenen Folgerungen*. *Handbuch der Radioaktivität und Elektronik* **2**, 432–488 (1907)
- Einstein, Albert, *Über die Entwicklung unserer Anschauungen über das Wesen und die Konstitution der Strahlung*. *Physikalische Zeitschrift* **10**, 817–825 (1909)
- Einstein, Albert, *Über den Einfluß der Schwerkraft auf die Ausbreitung des Lichtes*. *Annalen der Physik* **340**, 898–908 (1911)
- Einstein, Albert, *Die Feldgleichungen der Gravitation*. *Sitzungsberichte der Königlich Preußischen Akademie der Wissenschaften*, 844–847 (1915)
- Esarey, E., C. Schroeder, and W. Leemans, *Physics of laser-driven plasma-based electron accelerators*. *Reviews of Modern Physics* **81**, 1229–1285 (2009)
- Esarey, E., P. Sprangle, and J. Krall, *Overview of plasma-based accelerator concepts*. *Plasma Science, IEEE* **24**, (1996)
- Esarey, E., P. Sprangle, J. Krall, and A. Ting, *Self-focusing and guiding of short laser pulses in ionizing gases and plasmas*. *IEEE Journal of Quantum Electronics* **33**, 1879–1914 (1997)
- Filippi, F. et al., *Spectroscopic measurements of plasma emission light for plasma-based acceleration experiments*. *Journal of Instrumentation* **11**, C09015–C09015 (2016)
- Fitzpatrick, Richard, *Introduction to Plasma Physics: A graduate level course*.
- Geddes, C. G. R. et al., *High-quality electron beams from a laser wakefield accelerator using plasma-channel guiding*. *Nature* **431**, (2004)
- Gibbon, P., *Short pulse laser interactions with matter*, Imperial College Press (2005)
- Gigosos, Marco A. and Valentín Cardeñoso, *New plasma diagnosis tables of hydrogen Stark broadening including ion dynamics*. *Journal of Physics B: Atomic, Molecular and Optical Physics* **29**, (1996)
- Gigosos, Marco A., Manuel Á. González, and Valentín Cardeñoso, *Computer simulated Balmer-alpha, -beta and -gamma Stark line profiles for non-equilibrium plasmas diagnostics*, (2003).
- Goldberg, Lars, *Laser-Based Discharge Ignition for Capillary Waveguides*, Master's Thesis, Universität Hamburg (2013)
- Goldston, R.J. and P.H. Rutherford, *Introduction to Plasma Physics*, Taylor & Francis Group (1995)
- Gonsalves, A. J. et al., *Transverse interferometry of a hydrogen-filled capillary discharge waveguide*. *Physical Review Letters* **98**, 1–4 (2007)
- Gordon, D. et al., *Observation of Electron Energies Beyond the Linear Dephasing Limit from a Laser-Excited Relativistic Plasma Wave*. *Physical Review Letters* **80**, 2133–2136 (1998)
- Griem, H. R., *Spectral Line Broadening by Plasmas*, Academic Press (1974), ISBN: 0-12-302850-7
- Griem, H. R., *Principles of Plasma Spectroscopy*, Cambridge University Press (1997), ISBN: 0521455049
- Griem, H. R., M. Baranger, et al., *Stark Broadening of Neutral Helium Lines in a Plasma*. *Physical Review* **125**, 177–195 (1962)

- Griem, H. R., A. C. Kolb, and K. Y. Shen, *Stark broadening of hydrogen lines in a plasma*. Physical Review **116**, (1959)
- Hafz, Nasr a. M. *et al.*, *Stable generation of GeV-class electron beams from self-guided laser-plasma channels*. Nature Photonics **2**, 571–577 (2008)
- Hairapetian, G. *et al.*, *Experimental demonstration of dynamic focusing of a relativistic electron bunch by an overdense plasma lens*. Physical Review Letters **72**, 2403–2406 (1994)
- Hofelich-Abate, E. and F. Hofelich, *Time Behavior of a Laser with a Saturable Absorber as Q Switch*. Journal of Applied Physics **39**, 4823–4827 (1968)
- Holtzmark, J., *Über die Verbreiterung von Spektrallinien*. Annalen der Physik **363**, 577–630 (1919)
- Humphries, S., *Principles of charged particle acceleration*, John Wiley & Sons (1999)
- Jackson, J. D., *Classical Electrodynamics*, third edit, John Wiley & Sons, Inc. (1999)
- Jang, D. G., M. S. Kim, and I. H. Nam, *Interferometric density measurement of the gas-filled capillary plasma and its comparison with the H $\beta$  line measurement*, (2012).
- Jang, D. G., M. S. Kim, I. H. Nam, *et al.*, *Density evolution measurement of hydrogen plasma in capillary discharge by spectroscopy and interferometry methods*. Applied Physics Letters **99**, (2011)
- Jones, T. G. *et al.*, *Spatially resolved interferometric measurement of a discharge capillary plasma channel*. Physics of Plasmas **10**, 4504–4512 (2003)
- Kaganovich, D. *et al.*, *Variable profile capillary discharge for improved phase matching in a laser wakefield accelerator*. Applied Physics Letters **75**, 772–774 (1999)
- Keldysh, L.V., *Ionization in the field of a strong electromagnetic wave*. Sov. Phys. JETP , (1965)
- Kepple, P. and H. R. Griem, *Improved Stark Profile Calculations for the Hydrogen Lines H $\alpha$ , H $\beta$ , H $\gamma$ , and H $\delta$* . Physical Review **173**, 317–325 (1968)
- Keudell, A. von, *Einführung in die Plasmaphysik*, (2014)
- Kondratenko, A. M. and E. L. Saldin, *Generation of coherent radiation by a relativistic-electron beam in an undulator*. Doklady Physics **24**, (1979)
- Konjević, N., *Plasma broadening and shifting of non-hydrogenic spectral lines: Present status and applications*. Physics Report **316**, 339–401 (1999)
- Konjević, N., M. Ivković, and N. Sakan, *Hydrogen Balmer lines for low electron number density plasma diagnostics*. Spectrochimica Acta Part B: Atomic Spectroscopy **76**, 16–26 (2012)
- Kramida, A. *et al.*, *NIST Atomic Spectra Database (ver. 5.5.1)*, 2017
- Lemos, N. *et al.*, *Effects of laser polarization in the expansion of plasma waveguides*. Physics of Plasmas **20**, (2013)
- Macheret, Sergej O. *et al.*, *Shock wave propagation and dispersion in glow discharge plasmas*. Physics of Fluids **13**, 2693–2705 (2001)
- Mainfray, G. and C. Manus, *Multiphoton ionization of atoms*. Rep. Prog. Phys. **54**, 1333–1372 (1991)
- Malka, V. *et al.*, *Electron acceleration by a wake field forced by an intense ultrashort laser pulse*. Science (New York, N.Y.) **298**, 1596–600 (2002)
- Mangles, S. P. D. *et al.*, *On the stability of laser wakefield electron accelerators in the monoenergetic regime*. Physics of Plasmas **14**, 056702 (2007)

## Bibliography

---

- Margetic, V. *et al.*, *Comparison of nanosecond and femtosecond laser-induced plasma spectroscopy of brass samples*. *Spectrochimica acta, Part B: Atomic spectroscopy* **55**, 1771–1785 (2000)
- Martinez de la Ossa, Alberto *et al.*, *High-Quality Electron Beams from Beam-Driven Plasma Accelerators by Wakefield-Induced Ionization Injection*. *Physical Review Letters* **245003**, (2013)
- Maxwell, J. C., *On physical lines of force*. *The London, Edingburgh and Dublin Philosophical Magazine and Journal of Science* **21**, 161 (1861)
- McGuffey, C. *et al.*, *Effects of Ionization in a Laser Wakefield Accelerator*.
- McIntyre, D. H. *et al.*, *Continuous-wave measurement of the hydrogen 1 S -2 S transition frequency*. *Physical Review A* **39**, 4591–4598 (1989)
- Mehrling, Timon Johannes, *THEORETICAL AND NUMERICAL STUDIES ON THE TRANSPORT OF TRANSVERSE BEAM QUALITY IN PLASMA-BASED ACCELERATORS*, Dissertation, Universität Hamburg (2014)
- Messner, Philipp, *Target Design and Diagnostics for Laser Wakefield Acceleration*, PhD thesis, (2015)
- Modena, A., Z. Najmudin, and A. E. Dangor, *Electron acceleration from the breaking of relativistic plasma waves*. *Nature* **377**, 606–608 (1995)
- Morrow, R. and J. J. Lowke, *Streamer propagation in air*. *Journal of Physics D: Applied Physics* **614**, (1997)
- Mourou, G. and D. Umstadter, *Development and applications of compact highintensity lasers*. *Physics of Fluids B: Plasma Physics* **4**, 2315–2325 (1992)
- Nakamura, K. *et al.*, *GeV electron beams from a centimeter-scale channel guided laser wakefield accelerator*. *Physics of Plasmas* **14**, 056708 (2007)
- O’Shea, Patrick *et al.*, *Highly simplified device for ultrashort-pulse measurement*. *Optics Letters* **26**, 932 (2001)
- Osterhoff, J., *Stable, ultra-relativistic electron beams by laser-wakefield acceleration*, PhD thesis, (2009)
- Oz, E. *et al.*, *Ionization-Induced Electron Trapping in Ultrarelativistic Plasma Wakes*. *Physical Review Letters* **98**, 084801 (2007)
- Pak, A. *et al.*, *Injection and Trapping of Tunnel-Ionized Electrons into Laser-Produced Wakes*. *Physical Review Letters* **104**, 025003 (2010)
- Paschen, F., *Über die zum Funkenübergang in Luft, Wasserstoff und Kohlensäure bei verschiedenen Drucken erforderliche Potentialdifferenz*. *Annalen der Physik* **273**, 69–96 (1889)
- Perelomov, A. M. and V. S. Popov, *IONIZATION OF ATOMS IN AN ALTERNATING ELECTRICAL FIELD. Ill*. *Soviet Physics JETP* **25**, 336–343 (1967)
- Perry, M. D., T. Ditmire, and B. C. Stuart, *Self-phase modulation in chirped-pulse amplification*. *Optics Letters* **19**, 2149 (1994)
- Planck, Max, *Ueber das Gesetz der Energieverteilung im Normalspectrum*. *Annalen der Physik* **309**, 553–563 (1901)
- Popp, Antonia, *Dynamics of electron acceleration in laser-driven wakefields: Acceleration limits and asymmetric plasma waves*, PhD thesis, (2011)
- Poynting, John Henry, *Collected scientific papers*, Cambridge University Press (1920), ISBN: 9788578110796

- Pronko, P. P. *et al.*, *Machining of sub-micron holes using a femtosecond laser at 800 nm*. Optics Communications **114**, 106–110 (1995)
- Raman, C. V. and K. S. Krishnan, *A New Type of Secondary Radiation*. Nature **121**, 501–502 (1928)
- Rittershofer, W. *et al.*, *Tapered plasma channels to phase-lock accelerating and focusing forces in laser-plasma accelerators*. Physics of Plasmas **17**, (2010)
- Röckemann, Jan-Hendrik *et al.*, *Private Communication*, 2018
- Rosenzweig, J. B. *et al.*, *Experimental observation of plasma wake-field acceleration*. Physical Review Letters , (1988)
- Roth, J. R., *Industrial Plasma Engineering: Volume I - Principles*, Institute of Physics Press (1995)
- Rowlands-Rees, T. P. *et al.*, *Laser-Driven Acceleration of Electrons in a Partially Ionized Plasma Channel*. Physical Review Letters **100**, 105005 (2008)
- Sacek, Vladimir, 6.5. *Strehl Ratio*, 2006
- Salzberg, A. P. *et al.*, *Collision-induced electronic quenching of aluminum monoxide*. Chemical Physics Letters **180**, 161–167 (1991)
- Schaper, Lucas *et al.*, *Longitudinal gas-density profilometry for plasma-wakefield acceleration targets*. Nuclear Instruments and Methods in Physics Research, Section A: Accelerators, Spectrometers, Detectors and Associated Equipment **740**, 208–211 (2014)
- Schwenke, David W., *A theoretical prediction of hydrogen molecule dissociation/recombination rates including an accurate treatment of internal state nonequilibrium effects*. The Journal of Chemical Physics **92**, 7267–7282 (1990)
- Schwinkendorf, Jan-Patrick, *Sapphire capillaries for laser-driven wakefield acceleration in plasma*, Diplomarbeit, Universität Hamburg (2012)
- Siegman, Anthony E., *Lasers*, University Science Books (1986)
- Solyak, N. a. *et al.*, *Gradient Limitations in Room Temperature and Superconducting Acceleration Structures*. AIP Conference Proceedings **365**, 365–372 (2009)
- Spence, D. J., P. D. Burnett, and S. M. Hooker, *Measurement of the electron-density profile in a discharge-ablated capillary waveguide*. Optics Letters **24**, 993–995 (1999)
- Spence, D. J., A. Butler, and S. M. Hooker, *First demonstration of guiding of high-intensity laser pulses in a hydrogen-filled capillary discharge waveguide*. Journal of Physics B: Atomic, ... **4103**, (2001)
- Sprangle, P. *et al.*, *Propagation and guiding of intense laser pulses in plasmas*. Physical Review Letters , (1992)
- Stix, T. H., *The Theory of Plasma Waves*, 1st Ed., McGraw-Hill (1962)
- Suk, H. *et al.*, *Plasma Electron Trapping and Acceleration in a Plasma Wake Field Using a Density Transition*. Physical Review Letters **86**, 1011–1014 (2001)
- Svelto, O., *Principles of Lasers*, Fourth Ed., Springer Science+Media, Inc. (1998)
- Tajima, T. and J. M. Dawson, *Laser Electron Accelerator*. Physical Review Letters **4**, 267–270 (1979)
- Tauscher, Gabriele, *Ionisation of Hydrogen for Plasma Wakefield Accelerators*, PhD thesis, Universität Hamburg (2016)
- Tilborg, J. van *et al.*, *Active Plasma Lensing for Relativistic Laser-Plasma-Accelerated Electron Beams*. Physical Review Letters **115**, 184802 (2015)

## Bibliography

---

- Ting, A., E. Esarey, and P. Sprangle, *Nonlinear wake-field generation and relativistic focusing of intense laser pulses in plasmas*. *Physics of Fluids B: Plasma Physics* **2**, 1390 (1990)
- Tong, X. M. and C. D. Lin, *Empirical formula for static field ionization rates of atoms and molecules by lasers in the barrier-suppression regime*. *Journal of Physics B: Atomic, Molecular and Optical Physics* **38**, 2593–2600 (2005)
- Tonks, Lewi and Irving Langmuir, *Oscillations in Ionized Gases*. *Physical Review* **33**, 195–210 (1929)
- Wang, Faya *et al.*, *Performance Limiting Effects in X-Band Accelerators*, (2010).
- Weineisen, T. *et al.*, *Density measurement in a laser-plasma-accelerator capillary using Raman scattering*. *Physical Review Special Topics - Accelerators and Beams* **14**, 1–5 (2011)
- Wittig, G. *et al.*, *Optical plasma torch electron bunch generation in plasma wakefield accelerators*. *Physical Review Special Topics - Accelerators and Beams* **18**, 1–6 (2015)
- Yalçın, S., Y.Y. Tsui, and R. Fedosejevs, *Pressure dependence of emission intensity in femtosecond laser-induced breakdown spectroscopy*. *Journal of Analytical Atomic Spectrometry* **19**, 1295–1301 (2004)

# Acknowledgments

---

I would like to thank everyone who helped make this thesis happen.

Special thanks go to:

**Jens Osterhoff** for the opportunity to perform the work on this thesis in his group and for providing counsel when needed.

**Brian Foster and Bernhard Schmidt** for supervising my thesis.

**Lucas Schaper** for his intense mentoring, the countless hours spent in the lab, an open ear for discussions and tolerating my stupid jokes.

**Gabriele Tauscher and Martin Quast.** Without your help I would have gone mad in the lab. Well, maybe I still have...

**John Dale** for showing me how to code properly.

**Jan-Patrick Schwinkendorf** for useful advice and a helping hand.

**Gregor Loisch (DESY Zeuthen)** for enlightening conversations.

**All other people in the plasma / FLA group** for providing help and assistance whenever needed.

Also, thanks for providing me with the inspiration I needed to come up with the collection of names for our still nameless laser. I would still like to call it POTHEYTO, since it so elegantly captures the performance of the system ;)

Nevertheless, here are all of the names to preserve them for the future:

**POTHEYTO** - Poorly OpTimized High EnergY TiSa Oscillator

**ARROW** - Amplifier of Red Radiation to Obtain Wakefields

**FIRESTORM** - Fucking Intense Radiation for Experiments Systematically TransfORMing energy

**VIXEN** - Vicious Intensity for eXperiments using ElectroNs

**STARFIRE** - Super Tough AcceleratoR For Intense Radiation Experiments

**ELECTRONADO** - self explaining, isn't it?

**BEAST** - Beam for Electron Acceleration STuff

**HELGE** - High Energy Laser for GeV Electrons

*Bibliography*

---

**ASGARD** - Accelerator for Stimulated Generation of Accelerator RaDiation

**GIANT** - Great Intensity for Accelerators Nearly Tabletop

**TINY** - Tw INtensitY or Tw Intensity for iNjection studY

# Eidesstattliche Versicherung

---

Hiermit versichere ich an Eides statt, die vorliegende Dissertationsschrift selbst verfasst und keine anderen als die angegebenen Hilfsmittel und Quellen benutzt zu haben.

Die eingereichte schriftliche Fassung entspricht der auf dem elektronischen Speichermedium.

Die Dissertation wurde in der vorgelegten oder einer ähnlichen Form nicht schon einmal in einem früheren Promotionsverfahren angenommen oder als ungenügend beurteilt.

Hamburg, 15. Dezember 2018

---

Lars Goldberg